DESIGNING A UWB GENERATOR AND ANTENNA FOR CWD RADAR

DEVELOPMENT OF AN ULTRA-WIDEBAND (UWB) PULSE GENERATOR AND PRINTED ANTENNA FOR CONCEALED WEAPONS DETECTION RADAR

By

ERIC A. EVELEIGH, B.Eng.

A Thesis
Submitted to the Department of Electrical & Computer Engineering
and the School of Graduate Studies
in Partial Fulfilment of the Requirements
for the Degree of
Master of Applied Science

Master of Applied Science (2020)
(Electrical & Computer Engineering)

McMaster University
Hamilton, Ontario, Canada

TITLE:	Development of an Ultra-wideband (UWB) Pulse Generator and Printed Antenna for Concealed Weapons Detection Radar
AUTHOR:	Eric A. Eveleigh B.Eng. (McMaster University, Canada)
SUPERVISOR:	Prof. Natalia K. Nikolova Ph.D. (University of Electro-Communications, Japan), Dipl. Eng. (Technical University of Varna, Bulgaria), IEEE Fellow, P.Eng.
PAGES:	xxviii, 166

Lay Abstract

This thesis is about the improvement of a radio antenna and a transmitter. These are ultimately intended as components in a system for detecting weapons (such as firearms, knives, etc.) concealed within the clothing or bags of nearby persons. The detection happens by transmitting specific radio signals which interact harmlessly with a person being scanned, and then are received back by the system. This is a form of radio detection and ranging (RADAR). The research on these devices has consisted of computer simulations and real-life measurements. As a result, it appears that the transmitter and radio antenna have been improved to be more suitable for the desired application than they were originally.

Abstract

This thesis demonstrates the further development of an ultra-wideband (UWB) pulse generator and of an UWB antenna. Custom prototypes of these devices were initially developed for an ongoing research project. The project topic is a compact and portable concealed weapons detection (CWD) radar system to find objects such as firearms, knives, and grenades hidden on persons as they pass by. The system uses the UWB pulse generator as a transmitter, while the UWB antenna radiates the pulse and receives the corresponding backscatter from targets and other objects. Initial device prototypes do not perform adequately according to project specifications. A key specification is of adequate operation over the entire 0.5 GHz to 5 GHz frequency band, where adequate operation is defined distinctly for the antenna and pulse generator. In this work, empirical investigations of both devices are performed using techniques such as simulation, fabrication, and measurement. Through these investigations, the designs of the devices have been incrementally modified. Measured performance data suggest that the research has yielded designs with substantially improved bandwidth as a result. Bandwidth increases from 3.31 GHz to 4.36 GHz (31.7%) for the pulse generator and from 0.46 GHz to 4.98 GHz (983%) for the antenna are demonstrated. Future work is needed to establish the effects of fabrication tolerance, component tolerance, and human error on the variation of the observed device performance.

Acknowledgements

The completion of this work would not have been possible without the influence of many whom I have personally interacted with in these past years. They all deserve my acknowledgement and deepest gratitude.

First and foremost I would like to thank Dr. Natalia K. Nikolova, my thesis supervisor, for offering me the opportunity to pursue Master's studies under her supervision. Professor Nikolova has made her expertise available to me and provided much help and advice over the course of these past years. I have been encouraged and re-assured to continue with my work countless times, as well as offered constructive criticism on how my work could be improved. For these things I continue to be grateful as my work comes to a close.

I would like to thank Dr. John W. Bandler, OC, for his guidance in preparing my Three Minute Thesis (3MT®) presentation for both the University- and department-wide competitions in 2019, and also for his stalwart advice regarding the preparation of this thesis itself.

I acknowledge the funding contributions of the North Atlantic Treaty Organization (NATO), the Natural Sciences and Engineering Research Council of Canada (NSERC) and Patriot One Technologies, Inc. Their contributions have made my studies possible.

I also thank a number of my research lab colleagues. I thank Aaron Pitcher, for his various conversations with me about research challenges in these past years, and I acknowledge his provision of a LaTeX template for this very document that I have been able to use as a starting point. We have also co-authored a conference publication. I thank Daniel Tajik, for his reassurance in my abilities, and his assistance in my preparations to attend AP-S/URSI 2019—my first academic conference abroad. I acknowledge Dr. Charl Baard, for reviewing my manuscript of chapter 2, and I thank him for offering his insights based on his experiences with radar hardware and his position of Research Engineer in our lab. I acknowledge Alex Beaverstone, for his co-authorship on my second conference paper, and I thank him for his kindness.

I thank Cheryl Gies, for organizing everything behind the scenes, and helping me out whenever I had questions about my academic program.

I thank Tyler Ackland, for always handling our lab orders for supplies, components, and PCBs that allowed me to complete my hardware investigations.

I thank the technical support staff of the McMaster University ECE department, for assisting with software installations and maintenance on our research computers and servers.

Finally, I would like to thank my partner Grace, and my family members, for their continued love and support through my academic journey. They have encouraged me to keep going and see things through until the end.

Contents

List of Figures

List of Tables

Notation and Abbreviations

List of Abbreviations

Notation	Description	Page List
AWG	arbitrary waveform generator	45, 46
BOM	bill of materials	49, 50, 60, 153, 154
CAD	computer-aided design	155, 160
CMOS	complimentary metal oxide semiconductor	23, 35, 36
CNC	computer numerical control	95, 108

Notation	**Description**	**Page List**
CPW	co-planar waveguide	xxvi, 11, 36, 40, 42, 88, 89, 93–95, 156, 158, 164
CW	continuous wave	6–8
CWD	concealed weapons detection	1–4, 6–9, 20, 31, 34, 35, 68, 69, 84, 85, 124, 125
DC	direct current	36, 45, 48
DDS	direct digital synthesis	23, 46
DSO	digital storage oscilloscope	44–46

Notation	**Description**	**Page List**
EM	electromagnetic	1–5, 9, 10, 69, 85, 86, 155, 157, 161
FCC	Federal Communications Commission	35, 78
FEM	finite element method	86
FFT	fast Fourier transform	27, 48
FMCW	frequency modulated continuous wave	8
FoM	figure of merit	33, 36, 59, 83, 84, 117–120
FR-4	Flame Retardant 4	82, 84, 88, 89, 95, 99, 107, 108, 157, 161, 165
FWHM	full width at half maximum	29

Notation	Description	Page List
HBT	heterojunction bipolar transistor	25, 35
HEMT	high electron mobility transistor	23, 35
HFSS	High Frequency Structure Simulator	86–89, 162
IC	integrated circuit	35, 50
IEEE	Institute of Electrical and Electronics Engineers	70
IRF	impulse response function	29, 79
LCP	Liquid Crystal Polymer	84, 85
LHCP	left-handed circular polarization	80
MMIC	monolithic microwave integrated circuit	35

Notation	Description	Page List
PCB	printed circuit board	10–12, 20, 39, 40, 42, 43, 48–50, 59, 68, 108, 110, 145, 153–155, 158
PEC	perfect electric conductor	86, 88, 89, 107, 161, 163, 166
PML	perfectly matched layer	87
PRF	pulse repetition frequency	7, 20, 30–32, 34, 44, 46, 47, 51–60
PSD	power spectral density	32

Notation	Description	Page List
PTFE	polytetrafluoroethylene	89
RBW	resolution bandwidth	27
RF	radio frequency	23, 36, 40, 49, 60, 61
RHCP	right-handed circular polarization	80
RMS	root-mean-square	xxvi, 30, 70
SMA	sub-miniature A	45, 46, 49, 82, 86, 88, 89, 95, 108, 110, 114, 162
SOL	short-open-load	110, 112
SRD	step recovery diode	23, 35, 36, 38, 39, 42, 49, 60

Notation	Description	Page List
SWR	standing wave ratio	73, 74, 77
TEM	transverse-electric-magnetic	72
TTL	transistor-to-transistor logic	38, 46
Tx	transmitter	10, 21, 31, 78, 80
UWB	ultra-wideband	2, 7, 9, 12, 20–23, 25, 29, 33, 35, 59, 68, 74, 78, 79, 83, 84, 96, 124, 125

Notation	**Description**	**Page List**
VNA	<u>v</u>ector <u>n</u>etwork <u>a</u>nalyzer	10, 79, 86, 110, 112

List of Notation

Notation	**Description**	**Page List**
B	Absolute bandwidth	25, 33, 56, 75, 76, 84
b_{f}	Fractional bandwidth	33, 34, 76
b_{fr}	Frequency ratio	34–36, 76, 84, 118
ϵ_r	Relative permittivity of a dielectric medium	39, 84, 88, 89, 118, 157
e_r	Antenna reflection efficiency	74, 96
f	Frequency	25, 27, 70
f_c	Center frequency	33, 75, 76, 84

Notation	Description	Page List
f_l	Lower frequency limit of a specified frequency band	25, 27, 32–34, 36, 56, 75–77, 84, 118
f_u	Upper frequency limit of a specified frequency band	25, 27, 32–34, 36, 56, 75–77, 84, 118
l_1	Length of co-planar waveguide (CPW) between bias tee and SD1 in the pulse generator layout	42, 49, 56, 58
l_2	Length of CPW between SD1 and SRD1 in the pulse generator layout	42, 49, 50, 56, 58, 61
l_3	Length of the shorted CPW stub in the pulse generator layout	42, 43, 56, 58
P_{av}	Average (root-mean-square (RMS)) power	30, 32
ϕ	Azimuth angle	71, 99

Notation	**Description**	**Page List**
Γ	Voltage reflection coefficient	73, 74, 82, 96
r	Radial distance	71
R_A	Antenna input resistance	72
S_{11}	Scattering parameter from port 1 back to port 1; the reflection coefficient at port 1	73
$S(f)$	Magnitude spectrum	25
$s(t)$	Time-domain signal	25, 27–29
$\tan\delta$	Loss tangent of a dielectric medium	39, 88, 89, 157
θ	Elevation angle	71, 99
X_A	Antenna input reactance	72
Z_0	Characteristic impedance of a transmission line; system impedance	29, 40, 59, 73, 86
Z_A	Antenna input impedance	72, 73

Declaration of Academic Achievement

This thesis was written by Eric A. Eveleigh. Dr. Natalia K. Nikolova has reviewed the entire document and suggested textual revisions that have been considered at the author's discretion. In a similar way, Dr. Charl Baard has reviewed Chapter 2 of the document and offered suggestions to that part of the text. The overall contributions within the thesis have have not been changed as a result of the suggestions. Thus, the author declares his academic contributions to encompass the entirety of this document and the research presented within.

Chapter 1

Introduction

1.1 Motivation

Consider a visibly hidden, mass-deployable surveillance system for detecting unauthorized objects concealed by persons as they walk by. Perhaps this system could be carried by law enforcement, military, security personnel, or even mounted in hallways or building entrances to identify hostile individuals and trigger an appropriate response. When applied specifically to unauthorized weapons, such a system is called a concealed weapons detection (CWD) system. This system would be distinct from typical security checkpoints (airport security, for example) in that the persons being scanned would not have to cooperate with personnel or even know they are being scanned at all. The existence of such a system would conceivably be a significant step forward for public safety and personnel protection worldwide.

Electromagnetic (EM) radar techniques have been used for the detection of humans [1], [2] and the detection of concealed targets [3]. A CWD radar is essentially the combination of these ideas. The author of this thesis has been a part of a long-term project to achieve a functional CWD radar system. Previous work on this project by Justin McCombe [4] demonstrates a proof-of-concept prototype CWD radar system using both time-domain and frequency-domain measurements. A good background into CWD technologies is also provided in [4].

The radar system under development is composed of numerous distinct hardware modules. Two of these modules are a ultra-wideband (UWB) pulse generator and a UWB antenna element. Initial prototype designs of the pulse generator and antenna element were developed prior to the author's recruitment for the project. These designs do not perform adequately enough to meet the project specifications. Thus, the thesis author set out to improve the existing pulse generator and antenna designs, culminating in this work.

1.2 Concealed Weapons Detection Systems

Research into the remote detection of concealed, body-worn weapons and threats has been ongoing since at least as early as 1997 [5], [6]. Remote detection over the so-called stand-off distances is distinct from typical security checkpoints employing, for example, walk through metal detectors, in that the detection unit is located up to a number of metres away from the target. Classical EM and acoustic wave phenomena have both been used for the stand-off detection of concealed weapons, with successful remote imaging and/or detection using both phenomena demonstrated in the literature. Many examples of preliminary results have been shown [4], [6]–[18], whereas other sources have demonstrated quite promising results with actual humans or phantoms (physical models) as targets [5], [19]–[25]. Patents have also been filed for these kinds of systems, such as [26]. This thesis is focused on a specific subset of the EM detection systems, thus, the EM systems are the focus of the rest of the discussion in this section.

The EM stand-off CWD systems can be classified based on a handful of general categories, namely

1. detection modality (imaging-based detection vs. signature-based detection),
2. passivity (active vs. passive), and,
3. illumination type (frequency sweep vs. pulse).

The systems may also be described in terms of

- frequency band of operation,
- claimed detection range,
- claimed detection accuracy (true positive rate, false alarm rate).

Some of the previously cited CWD systems are compared by these categories and figures in Table 1.1. The categories are explained as follows.

1.2.1 Detection Modalities

First, we discuss the detection modalities. The imaging-based detection systems extract two or three dimensional images of targets using non-visible EM radiation. The images reveal visibly obscured features from which non-threat objects (i.e. human bodies, belt buckles, mobile phones) can be distinguished from threats (i.e. firearms, blades, explosives). Detection is performed either manually by a human operator who interprets the images, or automatically by computer algorithms. Examples of

Imaging-based Detection

Advantages

- Highly detailed images of hidden objects

Disadvantages

- privacy concerns
- trained image interpreter may be required

Signature-based Detection

Advantages

- automatic detection
- rapid threat response
- no privacy concerns

Disadvantages

- complete reliance on detection algorithms
- requires collection of threat signature database

Figure 1.1: Advantages and disadvantages of the CWD detection modalities.

promising imaging-based detection systems are found in [5], [19], [27], whereas many preliminary results have been shown in [6], [7], [9]–[16]. On the other hand, the signature-based detection systems generally do not generate images or image-like data. They instead rely on the recognition of specific, characteristic features that are uniquely present in the EM signals that are emitted from the desired targets upon their illumination. The recognition of such signatures in the detection space, then, allows the determination of the presence of threat versus non-threat objects using automated computer algorithms. Some examples of signature-based detection systems are found in [4], [18], [21], [23]–[25]. Advantages and disadvantages of the detection modalities are discussed in Figure 1.1.

Active Detection

Advantages

- potentially higher signal-to-noise ratios
  - detection range
  - detection accuracy
- control of target illumination

Disadvantages

- system operation can be easily detected by adversaries
- requires a transmitter

Passive Detection

Advantages

- relatively difficult to detect system in operation
- no transmitter hardware required

Disadvantages

- increased complexity (cost) of receiver hardware

Figure 1.2: Advantages and disadvantages of active versus passive CWD systems.

1.2.2 Passivity

Second, we discuss the system passivity. Active systems are classified as such since they introduce controlled EM radiation for the purposes of illuminating the desired target. These systems require some sort of transmitter to generate the desired illuminating signals. Some examples of active systems are [5], [21]–[23], [25], [27]. Passive systems, on the other hand, rely on existing EM emissions such as thermal blackbody radiation and they do not necessarily require any transmitter at all. Some examples of passive systems are [19], [24]. Advantages and disadvantages of the active versus passive systems are discussed in Figure 1.2.

1.2.3 Illumination Types

Third, we discuss the system illumination types. Illumination signals are only relevant to the active systems. The illuminations may be broadly classified into modulated continuous wave (CW) signals and pulsed signals. The modulated CW signals consist of a sinusoidal waveform which is either keyed on or off (amplitude modulation), perturbed in frequency (frequency modulation) or both. These signals are used to directly capture target responses over a desired range of frequencies. Some examples of systems using CW-type illuminations are [4], [5], [21], [23], [25]. The pulsed signals, on the other hand, consist of various shapes of wideband impulses which impose transient, time-domain illumination of targets. The resulting target response can be analysed using Fourier techniques to extract frequency information. Pulsed illumination in CWD systems is much less common than modulated CW illumination. An example of pulsed illumination is in [4]. Advantages and disadvantages of modulated CW versus pulsed illuminations are discussed in Figure 1.3.

CW Illumination

Advantages

- simple Rx/Tx architecture (superheterodyne)

Disadvantages

- long sweep times limit detection speed

Pulsed Illumination

Advantages

- all frequencies in desired band excited at once
- high pulse repetition frequency (PRF) possible

Disadvantages

- requires UWB pulse generator
- requires high-speed sampling receiver
- increased system complexity

Figure 1.3: Advantages and disadvantages of modulated CW versus pulsed illumination in CWD systems.

Table 1.1: Comparison of electromagnetic CWD systems in the literature.

Ref.	Year	Modality	Passivity	Illumination Signal	Band (GHz)	Range
[5]	1997	Imaging	Active	FMCW	93.25 - 94.75	20 m
[19]	2004	Imaging	Passive	N/A	75.5 - 93.5	15 - 25 ft
[21]	2009	Signatures	Active	interrupted CW	9.5 - 10.5	9 - 15 ft
[23]	2013	Signatures	Active	FMCW	75 - 110	<25 m
[24]	2013	Signatures	Passive	N/A	91 - 96	3 m
[25]	2019	Signatures	Active	FMCW/CW (Doppler)	5.48 - 6.12	7 m

1.2.4 Frequency Band of Operation

Demonstrated EM CWD systems make use of diverse frequency bands:

- Microwave frequencies: [4], [16], [21], [25]
- Millimetre-wave frequencies: [5], [19], [23], [24]
- Sub-Terahertz-frequencies: [13], [18]

Millimetre-wave frequencies are popularly used in the imaging-based detection systems for obtaining sufficient image resolution and penetration depth, while the microwave frequencies are more commonly used in the detection-based systems.

1.3 Research Objective

The main objective of this thesis was to modify existing UWB pulse generator and UWB antenna designs such that they would become more suitable for the CWD radar. The design requirements are summarized as follows. The pulse generator should produce a UWB pulse signal with a suitable time shape which covers a specific frequency band with sufficiently large power, whereas the UWB antenna element should radiate the pulse and/or receive the resulting backscatter from targets with minimum distortion and maximum efficiency. Thus, both devices, need to operate adequately within a common frequency band that the radar system is to use. Additionally, both hardware modules should be compact and low-cost, which is a pre-requisite for the mass deployment of the radar system.

1.4 Overview of the Research Efforts

The aforementioned pulse generator and an antenna element have been investigated in this work. The work undertaken for the pulse generator and the antenna element are outlined as follows.

1.4.1 Work Undertaken for the Antenna

The investigated antenna element is a compact printed circuit board (PCB)-based microwave antenna with wide bandwidth and an optional cavity backing. The author fabricated a handful of prototypes of the initial design in a semi-manual fashion using in-house equipment. The reflection coefficient of each fabricated prototype was measured with a vector network analyzer (VNA). Then, many EM simulations were performed in order to partially re-design the antenna, eventually yielding a final[1] version. A professional manufacturer produced fabricated prototypes of the final design. Afterwards, the reflection coefficient of the final design was measured for comparison with the initial design.

1.4.2 Work Undertaken for the Pulse Generator

The pulse generator is a compact, single-board wideband signal source which serves as the radar transmitter (Tx). The original design and operating theory of the pulse generator is found in [28], and its specifications are in [29]. A single functioning pulse generator prototype along with a simulation model was provided to the author. The simulation model of the generator circuit was tested in an attempt to identify useful circuit modifications. Model inaccuracies in the simulation were noted, so the

---

[1] With respect to this research

author decided instead to work directly with real PCBs. Initial tests were performed through soldering and de-soldering of components, such as

1. modification of component values (i.e. capacitance, resistance),
2. substitution of similar parts (i.e. slightly different transistors) for one another, and
3. relocation of shunt-mounted components to new positions on a co-planar waveguide (CPW) transmission line.

These changes required no modifications to the actual PCB layout and used the original layout. Later tests employed revisions to the PCB layout, such as the addition of new component pads, and the fine-tuning of transmission line lengths. In all, three new PCB revisions were designed and tested in this work. Time-domain measurements of the various pulse generator revisions were performed. Performance metrics were derived from the measurement data and used for comparison.

1.5 Significance

Neither a directly suitable antenna or pulse generator were found to be available for the project by means of purchase or within the literature. This is a result of the demanding nature of the system specifications and constraints related to physical size. The primary technical novelty for both modules is a very wide bandwidth ratio combined with small size. These modules are supposed to operate in a frequency band from 0.5 GHz to 5 GHz as specified in [29] and [28]. This prescribes a ten-to-one (10:1) bandwidth ratio, meaning that the upper frequency of the band is a factor of ten larger than the lower frequency of the band. At the same time, it is asked that the antenna remain constrained to a 15 cm by 15 cm by 5 cm profile, while the pulse generator must fit into an enclosure which limits the PCB size to roughly 5 cm by 12 cm. Thus, this research is relevant to those interested in the hardware side of compact, UWB pulsed radar, whether commercial, intellectual, or otherwise.

1.6 Structure of the Thesis

This thesis is organized into four chapters, followed by two appendices.

Chapter one is the introduction to the work and it is meant as an overview for everything else to follow. It is a brief part of the thesis.

Chapter two details the design efforts for the new generator revisions, including a review of UWB pulse generators, and shows the different design revisions and their performance.

Chapter three details the initial antenna design; design steps; measurements of input impedance; simulation of patterns, and polarization; and final results. It includes a background review of UWB antenna related definitions and prior work.

Chapter four offers concluding remarks and comments on possible future work.

In the appendices, sufficient information is provided to allow the replication of the pulse generator and the antenna hardware.

1.7 Contributions to Knowledge

In this thesis the author identifies design changes of the pulse generator and antenna element which appear to enhance the performance within at least one performance metric, primarily bandwidth. For each device, the prime contribution to knowledge is the final design wherein the discovered changes have been applied. In summary, the contributions are

1. An improved pulse generator design,
2. Details about the design changes which improved the pulse generator,
3. An improved antenna element design, and,
4. Details about the design changes which improved the antenna element.

Every effort is made to ensure that the contributed designs may be replicated. This has been accomplished through the provision of thoroughly detailed design information in the appendices.

1.8 Publications

Over the course of the research, the author contributed to two related publications. The first publication [30] is about the pulse generator, and the second publication [31] is about the antenna element.

References in Chapter 1

[1] A. G. Yarovoy, L. P. Ligthart, J. Matuzas, and B. Levitas, “UWB radar for human being detection,” *IEEE Aerospace and Electronic Systems Magazine*, vol. 21, no. 3, pp. 10–14, Mar. 2006, ISSN: 0885-8985. DOI: 10.1109/MAES.2006.1624185 (cit. on p. 1).

[2] S. Chang, N. Mitsumoto, and J. W. Burdick, “An algorithm for UWB radar-based human detection,” in *2009 IEEE Radar Conference*, May 2009, pp. 1–6. DOI: 10.1109/RADAR.2009.4976999 (cit. on p. 1).

[3] D. J. Daniels, *EM Detection of Concealed Targets*, 1st ed., ser. Wiley Series in Microwave and Optical Engineering. 111 River Street, Hoboken, NJ 07030-5774: John Wiley & Sons, 2010 (cit. on p. 1).

[4] J. J. McCombe, “Noise reduction and clutter suppression in microwave imaging and detection,” MASc Thesis, McMaster University, 2014. [Online]. Available: http://hdl.handle.net/11375/16345 (cit. on pp. 2, 4, 6, 9).

[5] G. R. Huguenin, “Millimeter-wave concealed weapons detection and through-the-wall imaging systems,” in *Command, Control, Communications, and Intelligence Systems for Law Enforcement*, E. M. Carapezza and D. Spector, Eds., International Society for Optics and Photonics, vol. 2938, SPIE, 1997, pp. 152–159. DOI: 10.1117/12.266735. [Online]. Available: https://doi.org/10.1117/12.266735 (cit. on pp. 2, 4, 5, 6, 8, 9).

[6] Y.-W. Chang, M. Juhola, W. Grainger, B. Wang, and B. Manahan, “Millimeter-wave concealed weapon detection,” in *Command, Control, Communications, and Intelligence Systems for Law Enforcement*, E. M. Carapezza and D. Spector,

Eds., International Society for Optics and Photonics, vol. 2938, SPIE, 1997, pp. 131–138. DOI: 10.1117/12.266731. [Online]. Available: https://doi.org/10.1117/12.266731 (cit. on pp. 2, 4).

[7] R. W. McMillan, O. Milton, M. C. Hetzler, R. S. Hyde, and W. R. Owerns, "Detection of concealed weapons using far-infrared bolometer arrays," in *25th International Conference on Infrared and Millimeter Waves (Cat. No.00EX442)*, 2000, pp. 259–260 (cit. on pp. 2, 4).

[8] N. C. Wild, F. Doft, D. Breuner, and F. S. Felber, "Handheld ultrasonic concealed weapon detector," in *Enabling Technologies for Law Enforcement and Security*, S. K. Bramble, E. M. Carapezza, L. I. Rudin, L. I. Rudin, and S. K. Bramble, Eds., International Society for Optics and Photonics, vol. 4232, SPIE, 2001, pp. 152–158. DOI: 10.1117/12.417527. [Online]. Available: https://doi.org/10.1117/12.417527 (cit. on p. 2).

[9] D. M. Sheen, D. L. McMakin, and T. E. Hall, "Three-dimensional millimeter-wave imaging for concealed weapon detection," *IEEE Transactions on Microwave Theory and Techniques*, vol. 49, no. 9, pp. 1581–1592, 2001 (cit. on pp. 2, 4).

[10] V. N. Radzikhovsky, V. P. Gorishniak, S. E. Kuzmin, and B. M. Shevchuk, "Radiometric imaging for concealed weapon detection," in *12th International Conference Microwave and Telecommunication Technology*, 2002, pp. 596–597 (cit. on pp. 2, 4).

[11] D. Notel, J. Huck, S. Neubert, S. Wirtz, and A. Tessmann, “A compact mmw imaging radiometer for concealed weapon detection,” in *2007 Joint 32nd International Conference on Infrared and Millimeter Waves and the 15th International Conference on Terahertz Electronics*, 2007, pp. 269–270 (cit. on pp. 2, 4).

[12] S. Stanko, D. Notel, A. Wahlen, J. Huck, F. Kloppel, R. Sommer, M. Hagelen, and H. Essen, “Active and passive mm-wave imaging for concealed weapon detection and surveillance,” in *2008 33rd International Conference on Infrared, Millimeter and Terahertz Waves*, 2008, pp. 1–2 (cit. on pp. 2, 4).

[13] D. M. Sheen, T. E. Hall, R. H. Severtsen, D. L. McMakin, B. K. Hatchell, and P. L. J. Valdez, “Standoff concealed weapon detection using a 350-GHz radar imaging system,” in *Passive Millimeter-Wave Imaging Technology XIII*, D. A. Wikner and A. R. Luukanen, Eds., International Society for Optics and Photonics, vol. 7670, SPIE, 2010, pp. 57–68. DOI: 10.1117/12.852788. [Online]. Available: https://doi.org/10.1117/12.852788 (cit. on pp. 2, 4, 9).

[14] X. Zhuge and A. G. Yarovoy, “A sparse aperture mimo-sar-based uwb imaging system for concealed weapon detection,” *IEEE Transactions on Geoscience and Remote Sensing*, vol. 49, no. 1, pp. 509–518, 2011 (cit. on pp. 2, 4).

[15] A. Kumar and B. Jassal, “94 ghz radiometer for benchmarking its operational parameters for the remote detecton of concealed threat.,” *Defence Science Journal*, vol. 65, no. 5, 2015 (cit. on pp. 2, 4).

[16] W. F. Moulder, J. D. Krieger, J. J. Majewski, C. M. Coldwell, H. T. Nguyen, D. T. Maurais-Galejs, T. L. Anderson, P. Dufilie, and J. S. Herd, “Development

of a high-throughput microwave imaging system for concealed weapons detection," in *2016 IEEE International Symposium on Phased Array Systems and Technology (PAST)*, 2016, pp. 1–6 (cit. on pp. 2, 4, 9).

[17] Y. Li, Z. Peng, and C. Li, "Potential active shooter detection using a portable radar sensor with micro-doppler and range-doppler analysis," in *2017 International Applied Computational Electromagnetics Society Symposium (ACES)*, 2017, pp. 1–2 (cit. on p. 2).

[18] Z. Sang and Y. Zhao, "Portable sub-terahertz radar for rapid long-range detecting concealed carried threat," in *2019 44th International Conference on Infrared, Millimeter, and Terahertz Waves (IRMMW-THz)*, 2019, pp. 1–2 (cit. on pp. 2, 4, 9).

[19] C. A. Martin and V. G. Kolinko, "Concealed weapons detection with an improved passive millimeter-wave imager," in *Radar Sensor Technology VIII and Passive Millimeter-Wave Imaging Technology VII*, R. Trebits, J. L. Kurtz, R. Appleby, D. A. Wikner, and N. N. Salmon, Eds., International Society for Optics and Photonics, vol. 5410, SPIE, 2004, pp. 252–259. DOI: 10.1117/12.543352. [Online]. Available: https://doi.org/10.1117/12.543352 (cit. on pp. 2, 4, 5, 8, 9).

[20] A. Achanta, M. McKenna, and J. Heyman, "Nonlinear acoustic concealed weapons detection," in *34th Applied Imagery and Pattern Recognition Workshop (AIPR'05)*, 2005, 7 pp.–27 (cit. on p. 2).

[21] J. Hausner, "Radar-based concealed threat detector," in *Radar Sensor Technology XIII*, K. I. Ranney and A. W. Doerry, Eds., International Society for Optics and Photonics, vol. 7308, SPIE, 2009, pp. 143–151. DOI: 10.1117/12.817478.

[Online]. Available: https://doi.org/10.1117/12.817478 (cit. on pp. 2, 4, 5, 6, 8, 9).

[22] D. A. Andrews, S. W. Harmer, N. J. Bowring, N. D. Rezgui, and M. J. Southgate, "Active millimeter wave sensor for standoff concealed threat detection," *IEEE Sensors Journal*, vol. 13, no. 12, pp. 4948–4954, 2013 (cit. on pp. 2, 5).

[23] N. J. Bowring, M. J. Southgate, D. A. Andrews, N. D. Rezgui, S. W. Harmer, and D. O'Reilly, "Development of a longer range standoff millimetre wave radar concealed threat detector," in *Radar Sensor Technology XVII*, K. I. Ranney and A. Doerry, Eds., International Society for Optics and Photonics, vol. 8714, SPIE, 2013, pp. 96–106. DOI: 10.1117/12.2016554. [Online]. Available: https://doi.org/10.1117/12.2016554 (cit. on pp. 2, 4, 5, 6, 8, 9).

[24] B. Kapilevich, B. Litvak, A. Shulzinger, and M. Einat, "Portable passive millimeter-wave sensor for detecting concealed weapons and explosives hidden on a human body," *IEEE Sensors Journal*, vol. 13, no. 11, pp. 4224–4228, 2013 (cit. on pp. 2, 4, 5, 8, 9).

[25] Y. Li, Z. Peng, R. Pal, and C. Li, "Potential active shooter detection based on radar micro-doppler and range-doppler analysis using artificial neural network," *IEEE Sensors Journal*, vol. 19, no. 3, pp. 1052–1063, 2019 (cit. on pp. 2, 4, 5, 6, 8, 9).

[26] N. K. Nikolova and J. J. McCombe, *On-body concealed weapon detection system*, US Patent 10,229,328, Mar. 2019 (cit. on p. 2).

[27] L. Carrer and A. G. Yarovoy, "Concealed weapon detection using uwb 3-d radar imaging and automatic target recognition," in *The 8th European Conference on*

Antennas and Propagation (EuCAP 2014), 2014, pp. 2786–2790 (cit. on pp. 4, 5).

[28] J. J. McCombe, "Cognitive microwave radar for the stand-off detection of on-body concealed weapons: Midterm report," McMaster University, CEM-R- 70, Mar. 2015 (cit. on pp. 10, 11, 31, 38).

[29] J. J. McCombe and N. K. Nikolova, "Transmitter specifications for the stand-off detection of on-body concealed weapons: NATO SPS G4992," McMaster University, CEM-R- 72, Jul. 2015 (cit. on pp. 10, 11, 31, 32, 34, 36).

[30] A. D. Pitcher, J. J. McCombe, E. A. Eveleigh, and N. K. Nikolova, "Compact transmitter for pulsed-radar detection of on-body concealed weapons," in *2018 IEEE/MTT-S International Microwave Symposium-IMS*, IEEE, 2018, pp. 919–922 (cit. on pp. 13, 23, 35).

[31] E. A. Eveleigh, A. S. Beaverstone, and N. K. Nikolova, "Printed cactus monopole antenna with enhanced impedance bandwidth," in *2019 IEEE International Symposium on Antennas and Propagation and USNC-URSI Radio Science Meeting*, IEEE, 2019, pp. 1085–1086 (cit. on pp. 13, 89).

Chapter 2

Development of the Ultra-wideband Pulse Generator

2.1 Introduction

Prior to this thesis, a prototype ultra-wideband (UWB) pulse generator was developed for the concealed weapons detection (CWD) radar application mentioned in Chapter 1. It was designed to produce pulses at a configurable pulse repetition frequency (PRF) as determined by an external trigger signal.

The author of this thesis has engaged in further research with the pulse generator. The purpose of the research was to find a pulse generator design with performance that is more in line with the specifications of the CWD radar project when compared to the existing prototype. We hypothesized that such an improved design could be created by modifying the circuit and printed circuit board (PCB) layout of the existing prototype without fundamentally altering the pulse generation topology. Otherwise, an entirely different design would need to be found.

In this chapter, the author details his research efforts with the prototype UWB pulse generator. First, the original specifications of the device and the appropriate performance metrics are defined. This is followed by an outline of the design of the initial prototype. Then, the experimental setup is detailed. A summary of the incremental designs of the pulse generator is given. The experimental data are presented in the form of plots and tables. Finally, an analysis of the data is performed and conclusions are drawn.

Before delving into the research, we will briefly review UWB signals, methods of generating UWB signals, and examples of existing UWB signal generation hardware.

2.1.1 UWB Signals

UWB signals are those which find use within UWB systems. The definition of an UWB system depends on what authority is consulted, for example, the government of Canada [32, §2], the United States [33] and others [34]. Generally, technology is considered to be UWB if it produces radio transmissions of sufficiently wide bandwidth. The signal generator (transmitter (Tx)) and transmitting antenna together determine the actual transmitted signal bandwidth. The antenna's role in this is covered in Chapter 3. Part of the UWB Tx's role is to produce signals of sufficiently wide bandwidth to enable UWB operation. The actual definition of signal bandwidth is provided in subsection 2.1.3.

Which kinds of signals can be used as UWB signals? The answer follows from Fourier theory and the scaling property. The Fourier scaling property implies that a signal which occupies a large time extent occupies a small frequency extent (bandwidth) and vice versa [35, p. 305], [36, p. 98], [37, p. 6]. Extreme examples are the infinite sinusoid $\sin(t)$, and the impulse function $\delta(t)$. The magnitude spectrum of the sinusoid is a shifted and scaled impulse function in frequency (and mirrored across 0 Hz into the negative frequencies), whereas the magnitude spectrum of the impulse function is a constant value over frequency. In other words, the sinusoid, which occupies all time, has vanishingly small bandwidth (only one exact frequency), whereas the impulse function, which occupies vanishingly small time, has infinite bandwidth (every possible frequency). Thus, UWB signals are those which occupy an ultra-short amount of time to consequently produce an ultra-wide bandwidth.

Some actual signals which find use in UWB systems include:

- Gaussian-derived pulses [36, pp. 98-101], [38, pp. 75-79], [39], [37, pp. 7-8], [40, pp. 40-44],
- Edge-derived pulses [36, pp. 101-104],
- Sinc pulses [36, pp. 104–107], [38, pp. 73-75],
- Truncated sine pulses [36, pp. 107-108], and,
- Chirp signals (frequency sweep) [38, pp. 86-88].

A common thread among these kinds of signals is their ability to occupy only a short duration which, as previously outlined, leads to a wide bandwidth through the scaling property. Radio systems that employ these signals are called impulse radio systems [40, p. 2]. Impulse radio systems, especially those using Gaussian-derived pulses, permit overall system designs with lower complexity (i.e. lower cost) at the expense of reduced spectral efficiency (less than optimal usage of regulated radiation limits) [39]. The pulse generator being investigated in this chapter generates a waveform that is empirically similar to a Gaussian-derived pulse. Thus, it is useful to examine the Gaussian-derived pulses in further detail.

From [36, pp. 98-99], the family of Gaussian pulse signals can be described algebraically in the time-domain as

$$T_n(t) = \frac{\tau^n \left(\frac{n}{2}\right)!}{n!} \frac{d^n}{dt^n} e^{-\frac{t^2}{\tau^2}} \tag{2.1}$$

and in the frequency-domain as

$$F_n(\omega) = \frac{\tau^n \left(\frac{n}{2}\right)!}{n!} \left(\jmath\omega\right)^n \sqrt{\pi\tau^2} e^{-\frac{\tau^2\omega^2}{4}} \tag{2.2}$$

where τ is a time constant, and n is the order of the differentiation. For general n including odd values, the $\left(\frac{n}{2}\right)!$ must be evaluated using the Gamma function [41] whereby $\left(\frac{n}{2}\right)! = \Gamma\left(\frac{n}{2}+1\right)$. The generator produces a waveform which is empirically similar to a Gaussian monocycle (1st derivative). Examples of Gaussian pulse functions are shown in Figure 2.1.

2.1.2 Generating UWB Signals

There are at least two distinct methods of generating UWB pulses, namely radio frequency (RF)/microwave analogue techniques, and, digital synthesis methods such as direct digital synthesis (DDS). Modern analogue techniques make use of solid-state devices such as diodes and transistors. Diode types which see use in UWB pulse generators are step recovery diodes (SRDs) [30], [37], [42]–[44], tunnel diodes [37], and Schottky diodes [30], [42], [43]. Semiconductor technologies include complimentary metal oxide semiconductor (CMOS) [45]–[48], high electron mobility transistor

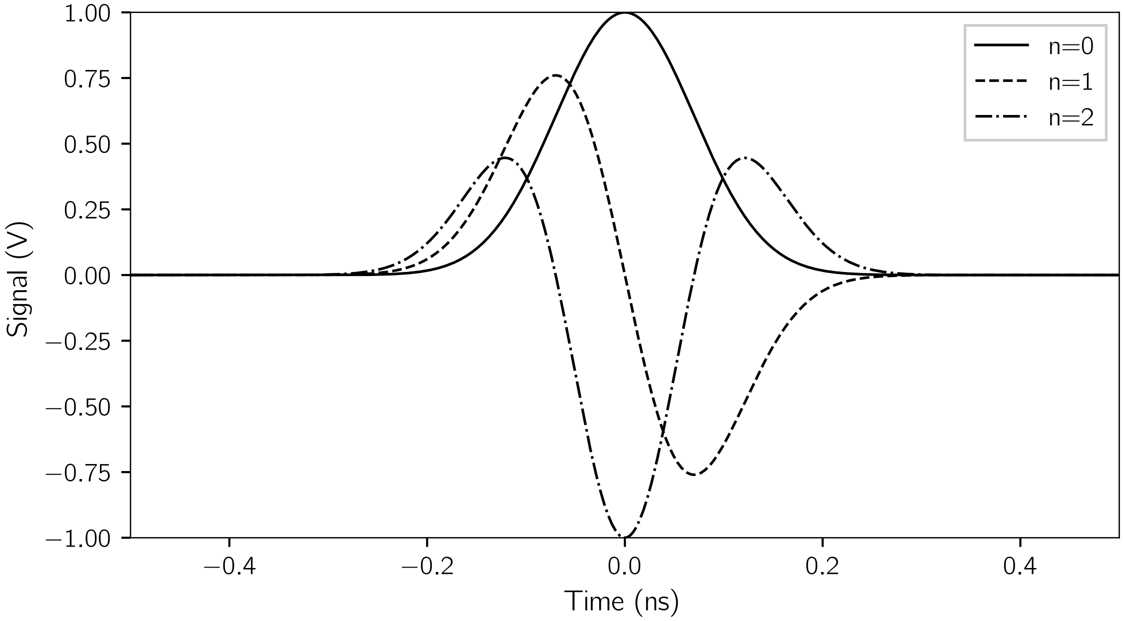

(a) time-domain

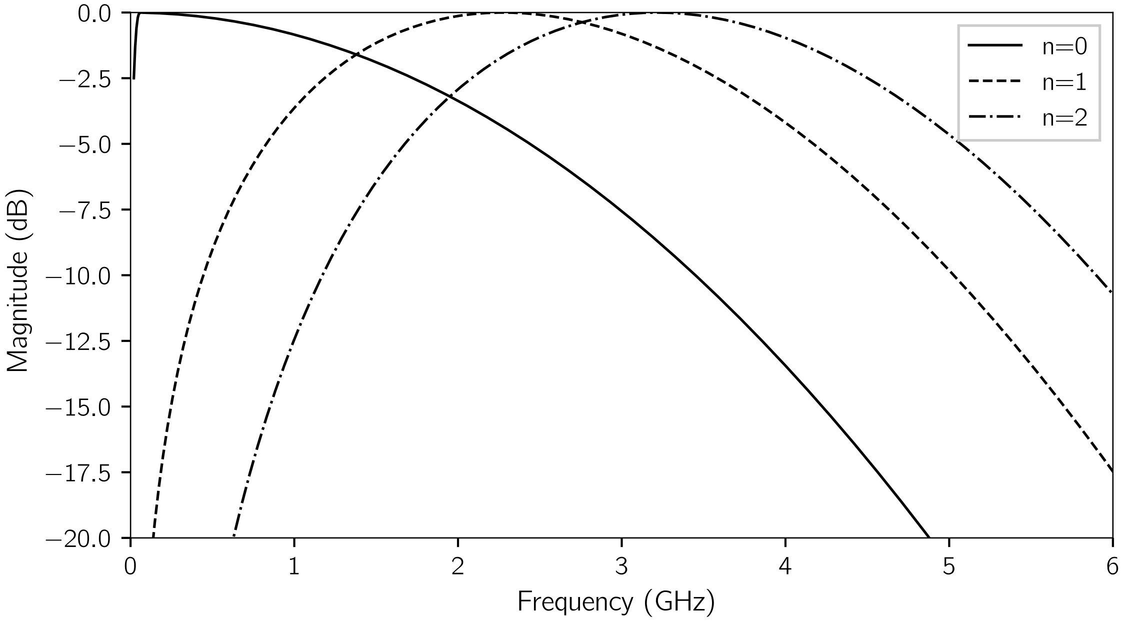

(b) frequency-domain

Figure 2.1: Time shape and spectrum of some Gaussian-derived pulses.

(HEMT) [49]–[51], and heterojunction bipolar transistor (HBT) [52], [53].

2.1.3 Performance Metrics

The performance of UWB pulse generators can be captured with a number of metrics. These metrics include bandwidth and output power as well as some other important quantities.

Bandwidth and Operating Band

Bandwidth can be defined in multiple ways, but here it is defined as an absolute (as opposed to relative or fractional) bandwidth. Absolute bandwidth is defined in the frequency-domain as the difference between the upper and lower frequencies of the operating band. That is,

$$B = f_u - f_l \tag{2.3}$$

where B is the bandwidth, whereas f_u and f_l are the upper and lower cutoff points of the operating band. The operating band is defined here based on the peak value of the signal magnitude spectrum in dB which is calculated as

$$S_{dB} = 20 \log_{10} |S(f)| \tag{2.4}$$

where $S(f)$ is the complex spectrum of the time-domain signal $s(t)$. When the signal spectrum is normalized so that the peak lies at $0\,\mathrm{dB}$ (denoted $\overline{S_{dB}}(f)$), the cutoff points are those frequencies on either side of the peak frequency (f_{pk}) where the normalized spectrum is equal to $-10\,\mathrm{dB}$ for the first time. More explicitly, the value of f_u is the closest frequency point above f_{pk} where it is found that $\overline{S_{dB}}(f) = -10\,\mathrm{dB}$.

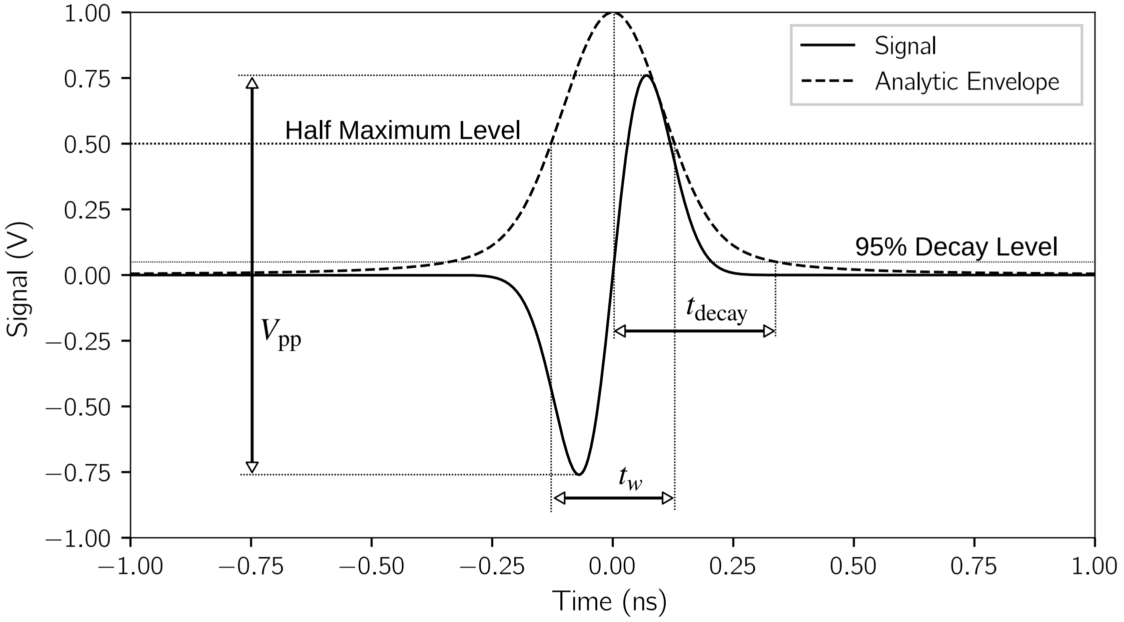

(a) time-domain

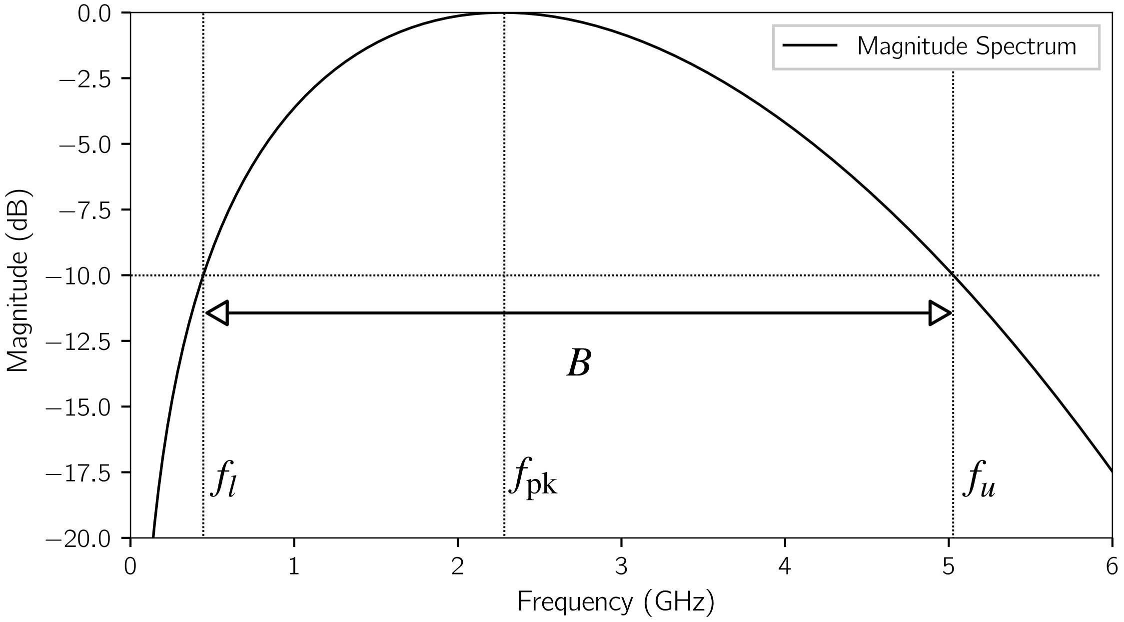

(b) frequency-domain

Figure 2.2: Pulse generator performance metrics in the time and frequency domains.

Similarly, the value of f_l is the closest frequency point below f_{pk} where it is found that $\overline{S_{dB}}(f) = -10\,\mathrm{dB}$.

For this research, the values of f_u and f_l were approximated by examining the discrete spectrum from the fast Fourier transform (FFT) of the measured pulse signal. In most cases, no frequency bin lies exactly at f_u or f_l. A simple way around this is to find the frequency bins where the discrete spectrum first falls below $-10\,\mathrm{dB}$. Then, f_u and f_l are known to within the discrete frequency resolution of the FFT, or resolution bandwidth (RBW). The error can be made quite small by taking a larger number of samples of $s(t)$ to decrease the corresponding RBW. Another method is to find the frequency bins that lie on either side the $-10\,\mathrm{dB}$ points, then perform polynomial interpolation between the points. This way f_u and f_l can be approximated more precisely than the actual RBW, provided that the underlying spectrum function is smooth.

The FFT interpolation method was used in this research to extract operating band and bandwidth information from time-domain measurements of the studied pulse generator.

Amplitude

The pulse amplitude is defined in terms of peak-to-peak value. It is determined as the difference between the maximum and minimum observed voltage value of the measured pulse. This research used cubic spline interpolation between discrete sample points to determine the minimum and maximum peak values.

Peak-to-peak voltage does not directly correspond to signal power when signals are compared. Consider signal $s_1(t)$, which has a maximum voltage of $2\,\mathrm{V}$ and a minimum voltage of 0 V. It has a peak-to-peak voltage of 2 V and a peak power of 4 W into a 1 Ω load. Consider also signal $s_2(t)$ which has a maximum voltage of 1.5 V and a minimum voltage of 1.5 V. This signal has a peak-to-peak voltage of 3 V, but a peak power of only 2.25 W into the same 1 Ω load. It is indeed the case that signal 2 has a larger peak-to-peak voltage than signal 1, but, on the other hand, signal 2 has a smaller peak power than signal 1. Thus, the observation that one signal has a larger peak-to-peak voltage than some other signal does not necessarily indicate which signal is most powerful.

Envelope Width and Decay Time

From the measured pulse signal, a signal called the analytic envelope can be computed. The first step is to construct the analytic signal, defined as

$$s_a(t) = s(t) + \jmath \mathrm{HT}\left\{s(t)\right\} \tag{2.5}$$

where $s_a(t)$ is the analytic signal and HT{} is the Hilbert transform [39], [38, pp. 36-37]. Then, the analytic envelope is simply

$$s_{\mathrm{env}}(t) = |s_a(t)| \tag{2.6}$$

which represents the instantaneous amplitude of the original pulse signal (see Figure 2.2a).

The discrete analytic signal is readily computed from the measured signal through

Fourier techniques. In this research, the actual implementation made use of the built-in `hilbert` function within the Python[1] package `scipy.signal`[2].

The decrease of the analytic envelope on either side of its peak value can be used to characterize the pulse width and decay time. In this research, the definition of envelope width (t_w) as the amount of time that the analytic envelope value remains above half of the peak value (usually referred to as full width at half maximum (FWHM)) was used. In a similar way, the definition of envelope decay time as the amount of time that the analytic envelope remains above 5% of the peak value after the peak is reached was also used. These metrics were adapted from [39] wherein they are used to characterize the impulse response function (IRF) of UWB antennas.

Peak Power

One way to define the output power is through peak power. Peak power is defined here as the maximum instantaneous power of the measured pulse. Instantaneous power is defined as

$$p(t) = \frac{|s(t)|^2}{Z_0} \tag{2.7}$$

where $s(t)$ is the voltage signal and Z_0 is the system impedance assumed equal to $50\,\Omega$. As with the amplitude metric, the maximum value of the power function is estimated using cubic spline interpolation between the sample points. The peak power informs us of the maximum excursion of the signal and how strong it is.

---

[1] The Python programming language - https://www.python.org/

[2] SciPy - https://scipy.org/

Average Power

Another way to define the output power is using the average power. The pulse generator average power, or root-mean-square (RMS) power, refers to the average power contained in the generated pulse train. Average power is a function of both the pulse shape and also the PRF. The average power is equal to the total energy in one pulse multiplied by the number of pulses per second which is just the PRF value. The energy contained in a single pulse is

$$e_{\mathrm{pulse}} \approx \int_{t_{\mathrm{min}}}^{t_{\mathrm{max}}} p(t)\,\mathrm{d}t \tag{2.8}$$

where t_{min} and t_{max} are the limits of the observation window which are chosen sufficiently large such that $p(t)$ has effectively decayed to zero. Then, the average power is simply

$$P_{\mathrm{av}} = e_{\mathrm{pulse}} f_{\mathrm{PRF}} \tag{2.9}$$

where P_{av} is the average power in *watts* (W, $\mathrm{J\,s^{-1}}$), provided that e_{pulse} is the energy of one pulse in the pulse train in *joules* (J) and f_{PRF} is the PRF in *hertz* (Hz, $\mathrm{s^{-1}}$). In this research, Equation 2.8 is evaluated using numerical integration of the instantaneous power. Then, the average power is computed by Equation 2.9. This formulation neglects the effects of noise, namely the average noise power, because noise is outside the scope of this research.

Compared to the peak-to-peak amplitude, determining average power is a more robust way of comparing signal strength as it takes into account the actual rate of energy emission from a given generator under a specific operating PRF regardless of the actual pulse shape. When compared to the peak power, the average power tends to be a much lower value due to the nature of the ultra-short pulses.

2.2 Hardware Specifications and Prior Designs

The pulse generator discussed in this chapter was designed as a Tx for the CWD radar project. The specifications of the Tx are found in [29]:

- "Bandwidth: 500 MHz to 5 GHz"
- "Waveform Type: Undetermined. Currently a monocycle ([also known as] differentiated Gaussian) [pulse], but can be changed"
- "Output Power (at the antenna port): 10 W-15 W minimum and variable"
- "Pulse Repetition Rate: Variable from 1 MHz to 10 MHz"

The power specification itself was determined for the worst-case detection scenario, namely a detection range up to 20 m using antennas with only 1.5 dBi of gain. In [28], the bandwidth requirement has been re-iterated by stating that "the goal is to generate a pulse that can excite resonances between 500 MHz and 5 GHz . . . we will need a pulse generator capable of delivering a pulse with 4.5 GHz bandwidth."

The output power specification above is of average power delivered to a 50 Ω load (i.e. a well-matched antenna or amplifier). The average power is determined through Equation 2.7, Equation 2.8 and Equation 2.9. We may further specify the output power performance in terms of peak instantaneous power (Equation 2.7) or peak-to-peak amplitude with the assumption of an ideal pulse shape (see Equation 2.1, Equation 2.2, Figure 2.1 and Figure 2.2) at a specific PRF value.

The "ideal" monocycle pulse shape chosen by the thesis author is analytically defined from Equation 2.1, and Equation 2.2 by using a time constant τ equal to 100 ps, yielding a pulse with power spectral density (PSD) cutoff frequencies $f_u \approx 4.98\,\text{GHz}$ and $f_l \approx 0.440\,\text{GHz}$. These two frequencies cannot be simultaneously selected as exactly 5 GHz and 0.5 GHz in the ideal pulse since the analytical formulas have only one degree of freedom, namely τ, which modifies both frequencies at the same time. Thus, the author empirically modified the value of τ until a pulse with a near-ideal operating band was found. Such a pulse shape at unit peak-to-peak voltage has an energy of about $e_{\text{pulse}} = 852\,\text{fJ}$ when driven into $50\,\Omega$ based on Equation 2.7 and Equation 2.8. At a worst-case PRF of 1 MHz, the average power of the pulse train is thus $P_{\text{av}} = 0.852\,\mu\text{W}$ based on Equation 2.9, whereas the peak (maximum instantaneous) power is $p_{\text{max}} = 5.01\,\text{mW}$. To meet the minimum average power goal of 10 W, the voltage of the pulse must be increased by the square root of ratio of the average power quantities. The average power ratio is about 71 dB, which translates into a voltage gain of 3.43 kV/V from 1 V peak-to-peak. Thus, to meet the power goal stated in [29] for a PRF of 1 MHz, the required peak-to-peak amplitude of the pulse generator is about 3.43 kV, producing a peak power of 58.7 kW.

For ranges closer than 20 m, a simple approximate calculation can be used to adjust the average power requirements. The analysis in [29] employs the monostatic radar range equation for determining the required power level based on a minimum allowable power returning to the receiver. If we assume all else is equal except for the change in the range, including the assumptions made in [29] (particularly the far-zone assumption), we may observe that the ratio of received to transmitted power exhibits quartic dependence on range. In other words

$$\frac{P_r}{P_t} \propto \frac{1}{R^4} \tag{2.10}$$

where P_r is the received power, P_t is the transmitted power, and R is the range to target. It is easy to see then that if the range is reduced by a factor of, for example, one half, then the received power increases by a factor of not double, not quadruple, but actually a factor of 16. This allows a corresponding decrease in the transmit power by the same factor. For the actual system, then, at a detection range of only 10 m, this method estimates that a minimum average power of merely 625 mW would need to be provided by the pulse generator. Table 2.1 shows the results of this method when it is applied to a number of particular range values. In military and/or personnel protection applications, a detection range of 10 m to 20 m is needed for long-range performance. We can see from the table that such range requires extremely large pulses to be generated. For domestic civilian applications, on the other hand, a detection range of 5 m or less is sufficient.

2.2.1 Figure of Merit

A commonly used figure of merit (FoM) for UWB devices is the fractional bandwidth. Fractional bandwidth is defined in [36] and [38] as

$$b_{\mathrm{f}} = \frac{B}{f_c} = 2\frac{f_u - f_l}{f_u + f_l}. \tag{2.11}$$

Fractional bandwidth essentially quantifies the significance of the absolute bandwidth of a device by normalizing with the centre frequency. For example, we can compare

Table 2.1: Estimated minimum transmit power and pulse amplitude versus detection range for the CWD system. Based on the calculations in [29] with a range adjustment. Pulse amplitude based on the ideal pulse calculations in section 2.2.

Range (m)	Avg. Transmit Power (mW)	V_{pp} @ 1 MHz PRF (V)	V_{pp} @ 5 MHz PRF (V)
20	10 000	3426	1532
15	3164	1927	862
10	625	857	383
5	39	214	96
2	1	34	15

a microwave source which creates a pulse covering from 5 GHz to 55 GHz to a pulsed 1550 nm laser. The microwave source has a centre frequency of 30 GHz and an absolute bandwidth of 50 GHz, yielding a fractional bandwidth of 1.67. The pulsed laser has a centre frequency of about 193 THz, and if it produces a pulse with 50 GHz of bandwidth it yields a fractional bandwidth of less than 0.0002.

The fractional bandwidth is easily shown to be equivalent to the frequency ratio of the upper to lower cutoff frequency, in that a given frequency ratio is associated with only one unique value of fractional bandwidth. If the frequency ratio is defined as

$$b_{\mathrm{fr}} = \frac{f_u}{f_l} \tag{2.12}$$

then the fractional bandwidth can be written as

$$b_{\mathrm{f}} = 2\frac{b_{\mathrm{fr}} - 1}{b_{\mathrm{fr}} + 1}. \tag{2.13}$$

The pulse generator specified bandwidth from 0.5 GHz to 5 GHz represents a 10:1

frequency ratio ($b_{\mathrm{fr}} = 10$) which is equivalent to a fractional bandwidth of about 1.64.

2.2.2 Comparison with Prior Designs

Many UWB impulse generators are demonstrated in the literature. Generators based on SRDs [30], [42]–[44] provide moderate output power levels and generally higher bandwidth compared to the CMOS-based generators [45]–[48], [54]–[56] which offer higher levels of integration and lower cost in bulk production. Some monolithic microwave integrated circuit (MMIC) generators making use of HEMT [49]–[51] and HBT [52], [53] technologies exist whose performance rivals that of the SRD-based generators. Out of these choices, SRD-based generators continue to be suitable in situations requiring higher output power and bandwidth and are more readily prototyped than the custom integrated circuit (IC)-based generators.

Much of the demonstrated UWB pulse generators have been designed to cover the 3.1 to 10.6 GHz band (full band) [54]–[56] or some portion thereof [44]–[47], [49]–[53] based on the spectral mask imposed by the Federal Communications Commission (FCC) for UWB devices [57]. Coverage of the UWB full band entails a fractional bandwidth of about 1.09, which is much smaller than the value of 1.64 required by the CWD project. For this reason, such generators which have been designed specifically to meet regulatory requirements are unsuitable for direct use in the CWD radar system. Other generators which have been designed for specific applications such as biomedical imaging [58] and broadband dielectric spectroscopy [59] have been designed, as well as those whose goal has been that of topological enhancement [42], [43].

TABLE 2.2: COMPARISON OF EXISTING PULSE GENERATOR DESIGNS TO THE DESIGN SPECIFICATIONS.

Reference	f_l (GHz)	f_u (GHz)	FoM (b_{fr})	Type of Pulse	Technology
[42]†	0.254	2.88	1.675	Gaussian Monocycle	SRD
[44]	0.6	2.7	1.27	Gaussian Monocycle	SRD
[46]	3	5	0.5	Multi-cycle	0.13 µm CMOS
[48]	5.5	7.5	0.31	Multi-cycle	0.13 µm CMOS
[52]	3.2	5	0.44	Multi-cycle	2 µm GaAs HBT
[49]	3	5	0.5	Multi-cycle	0.25 µm pHEMT
[29]‡	0.5	5	1.636	Gaussian Monocycle	
Ideal pulse	0.440	4.98	1.675	Gaussian Monocycle	

†Bandwidth as determined by fitting time-domain plots to ideal pulse model by thesis author
‡Specification of desired performance; not a measurement of hardware

2.3 Initial Design Overview

2.3.1 Circuit Description and Operating Principles

The initial pulse generator circuit (Figure 2.3) consists of four interconnected subcircuit stages: the power supply, the driver, the SRD pulser, and the pulse forming network. The power supply provides 12 V direct current (DC) to the driver stage and an adjustable constant current to forward bias the shunt SRD within the pulser stage. It is important to note that the SRD pulse and pulse forming network stages are RF stages consisting of co-planar waveguide (CPW) transmission lines while the power supply and driver stages are designed under assumptions that standard circuit theory holds at least reasonably well.

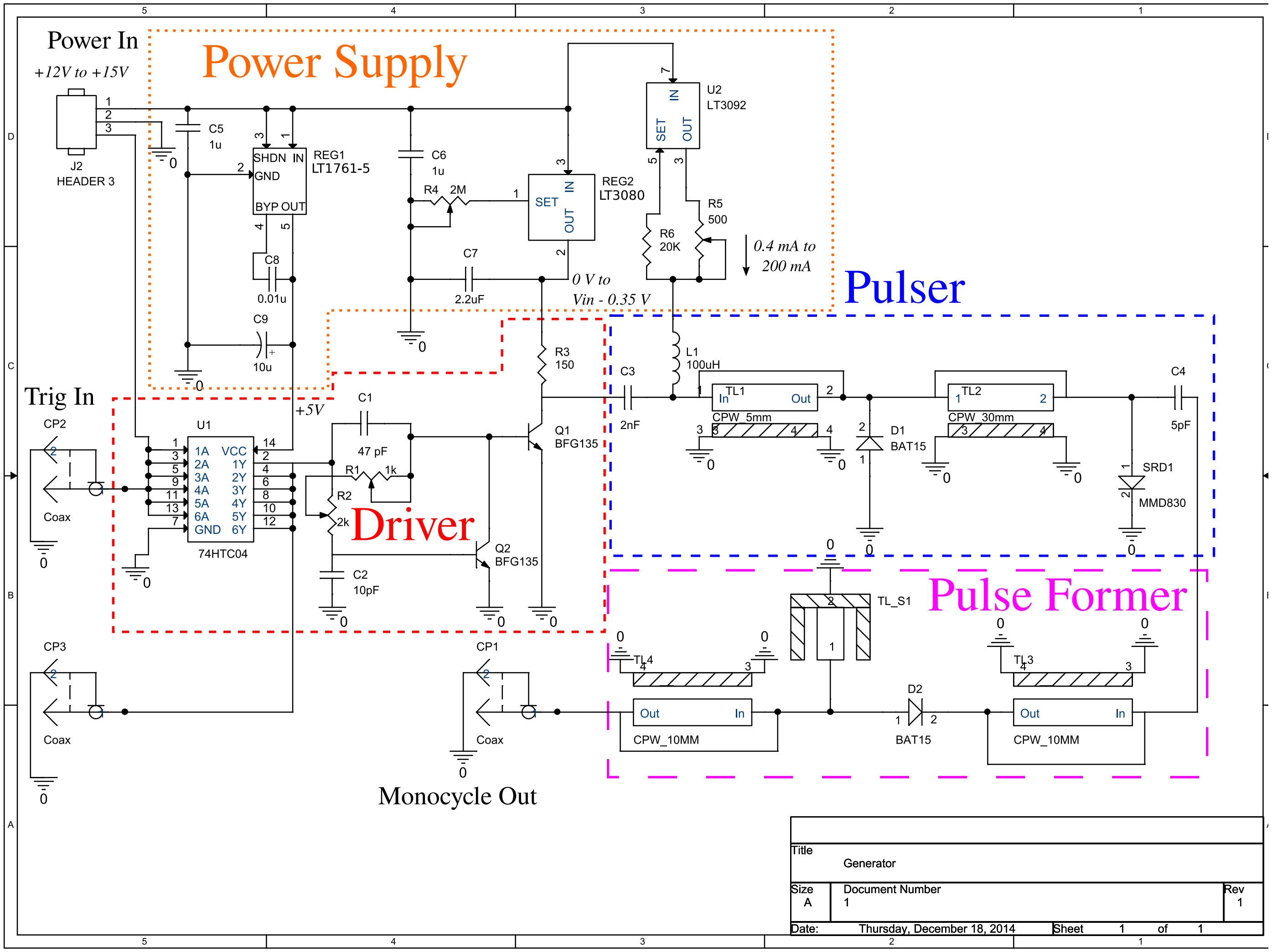

Figure 2.3: Annotated circuit schematic for revision 1 of the pulse generator.

The operating principles and details of the circuit may be found in [42] and [28]. A summary of the general SRD operation can be found in [37, pp. 47-48]. In the following summary of the operating principles, some components are referred to by their reference designators as seen in Figure 2.3.

The driver stage presents a high input impedance (high-Z) input port (CP2) which accepts a transistor-to-transistor logic (TTL) digital input signal (0 V low, 5 V high). Upon each falling edge of the input signal, the driver stage is triggered to output a broad (in time) negative voltage pulse. This broad pulse is then coupled into the SRD pulser stage through capacitor C3. Within the pulser stage a shunt SRD (SRD1) is forward biased with a constant current through inductor L1 (which forms a simple bias tee in combination with C3). When the negative driver pulse encounters SRD1, the diode is forced into reverse bias, rapidly releasing the stored junction charge and producing a sharp quasi-Gaussian (that is, empirically similar to a Gaussian waveform) negative voltage pulse. The quasi-Gaussian pulse propagates away from SRD1 towards the pulse forming network and also back towards the driver. A reverse shunt Schottky diode (D1) is strategically placed a distance away from SRD1 to effectively trap the driver-bound Gaussian pulse between the two diodes, who present as quasi-short-circuits to the pulse, by method of multiple internal reflection until the pulse has decayed enough to no longer forward bias the diodes. Meanwhile, the forward travelling quasi-Gaussian pulse encounters the pulse forming network which creates a positive quasi-Gaussian pulse from the original negative pulse using a shorted transmission line stub. The stub is connected in a tee configuration such that some of the incident quasi-Gaussian pulse continues down to the pulse generator output, while the other portion either travels down the stub and becomes a positive pulse or is reflected back. Another Schottky diode (D2) prevents the reflected pulse from fully reflecting back into the pulser stage such that most of the signal continues to bounce around within the pulse forming network until finally reaching the output port or being dissipated. At the generator output the signal is a combination of a negative quasi-Gaussian pulse, a delayed positive quasi-Gaussian pulse, and a tail of so-called ringing from the internal reflections of the generator stages. When the circuit is properly adjusted, the output signal resembles a Gaussian monocycle waveform.

Some parts of the circuit were designed to be hand-tuned. This was achieved through the use of adjustable resistors for components R1, R2, R4, and R5. Using a small screwdriver or purpose-designed tool, the value of each of these resistance values can be adjusted. Adjustment of R1 and R2 changes time constants within the driver stage which modifies the resulting driver pulse that is produced upon triggering. Adjustment of R4 allows the regulated voltage output of REG2 to be varied, also affecting the driver stage. Finally, adjusting R5 allows the regulated current output from U2 which affects the SRD1 bias point.

2.3.2 Physical Realization

The circuit was implemented on a two layer PCB designed for a specific Aluminum enclosure[3]. The PCB is made of either Rogers 4350B or Rogers 4003C microwave laminate[4]. Rogers RO4350B has $\epsilon_r = 3.66$ from 8 GHz to 40 GHz and loss of $\tan\delta = 0.0037$ at 10 GHz. Rogers RO4003C has $\epsilon_r = 3.55$ from 8 GHz to 40 GHz and loss of $\tan\delta = 0.0027$ at 10 GHz. The laminates are very similar in electrical performance and are reasonably interchangeable. The main difference is that RO4003C exhibits

---

[3] Boxenclosures B1-120BL (Datasheet)

[4] Rogers RO4000 series laminates (Datasheet)

Table 2.3: PCB stackup of the pulse generator.

Order	Name	Material	Thickness
1	Top Legend	Silkscreen	N/A
2	Top Solder Mask	Solder Mask	approx 0.6 mil
3	Top Copper	Copper	1.4 mil
4	Substrate	Rogers 4350B/4003C	30 mil/32 mil
5	Bottom Copper	Copper	1.4 mil
6	Bottom Solder Mask	Solder Mask	approx 0.6 mil
7	Bottom Legend	Silkscreen	N/A

somewhat lower loss. The PCB stackup is detailed in Table 2.3 and an annotated image of the assembled circuit is displayed in Figure 2.4. The RF portion of the board is composed of grounded CPW transmission line. The gap and trace width of the CPW line are 0.864 mm (34 mil) and 1.592 mm (62.7 mil). When using 30 mil RO4350B, Z_0 is about 49.9 Ω. When using RO4003C instead, Z_0 is about 52.6 Ω. These figures were calculated for each substrate by using the average value yielded from [60] and [61].

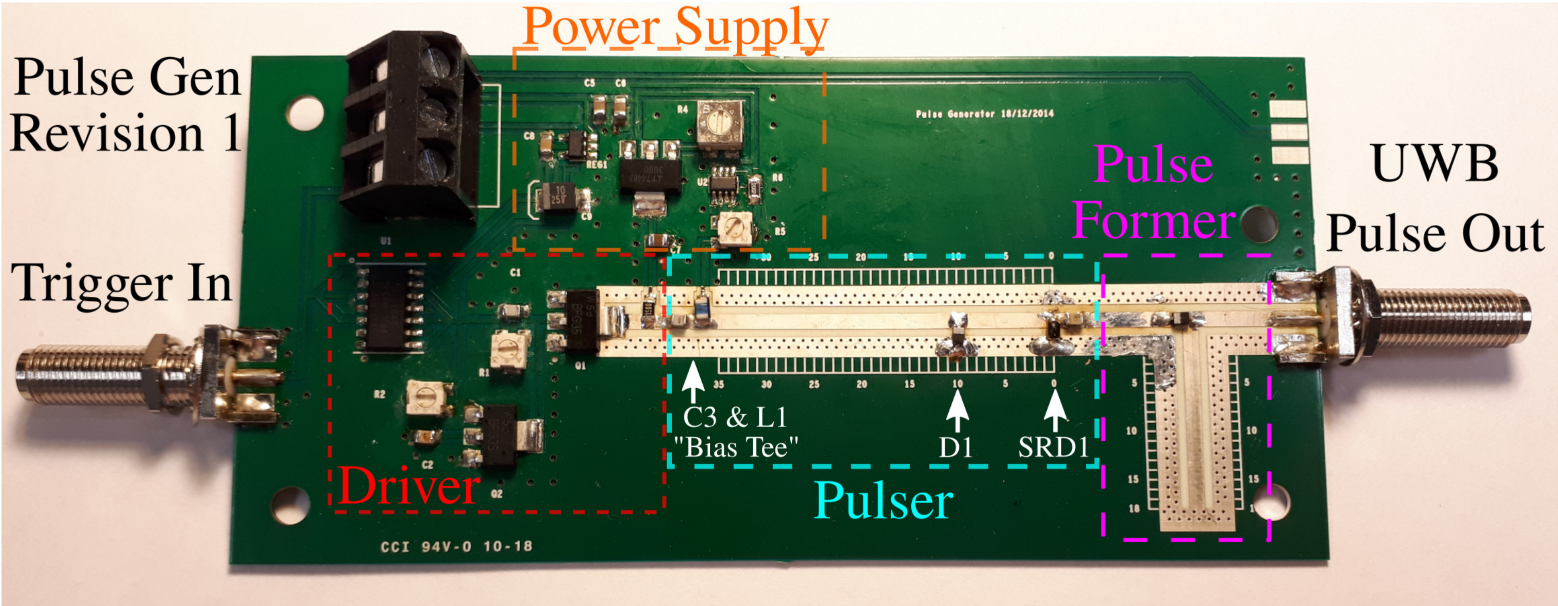

Figure 2.4: Annotated photo of a fabricated revision 1 pulse generator.

2.4 Experimental Setup

The experimental setup consisted of experimental variables, an appropriate measurement setup, and a design procedure. The variables were defined so that, by changing the variables, corresponding changes in the observable performance of the pulse generator occurred. The measurement setup was created to facilitate consistent, repeatable observation of the pulse generator performance. A design procedure was used to make use of the variables and the measurement setup in such a way that the generator performance would improve over repeated trials. The experimental variables, measurement setup, and the design procedure are detailed next.

2.4.1 Variables

The following variables were chosen:

- l_1 - the length of the CPW line between the output of the bias tee and SD1
- l_2 - the length of the CPW line between D1 and SRD1
- l_3 - the length of the CPW line that forms the shorted stub within the pulse former

These variables are indicated on the PCB artwork in Figure 2.5. In this work, the variable values were changed as follows. Variables l_1 and l_2 were adjusted by de-soldering and re-soldering D1 at different locations along the CPW line, while SRD1 remained at a fixed location. Since only D1 was moved, the sum of l_1 and l_2 remained a fixed value on a given PCB. Thus, the *sum* of l_1 and l_2 was modified only by changing the PCB artwork to alter the total length of the main CPW line. The next

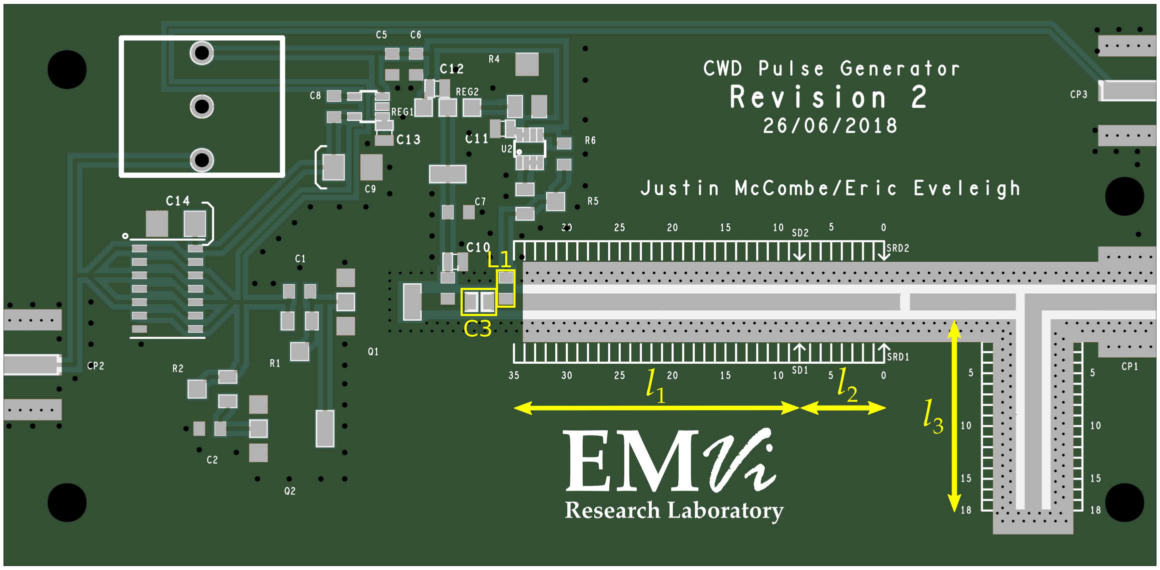

Figure 2.5: Physical variables of the pulse generator PCB.

variable, l_3, was changed by reducing the effective length of the shorted stub using metallic copper tape shunted across the exposed planar conductors. This lead to a certain fine-tuning of the shorted stub length wherein the stub length was not set permanently until after having adjusted the other length variables.

Many more variables might have been defined for the investigation, but this was forgone for practical reasons. For example, the trimmer resistors on board (R1, R2, R4, R5—see Figure 2.4) could have been used as variables, but it would have been difficult to have specified precise values to be set. Instead, the trimmer resistors were hand-tuned on each of the fabricated prototypes to yield good performance. Such hand tuning was not performed randomly, but with a certain intuition, guided by examination of the trimmer dial positions on other prototypes and the effects of individual tuning on the overall performance.

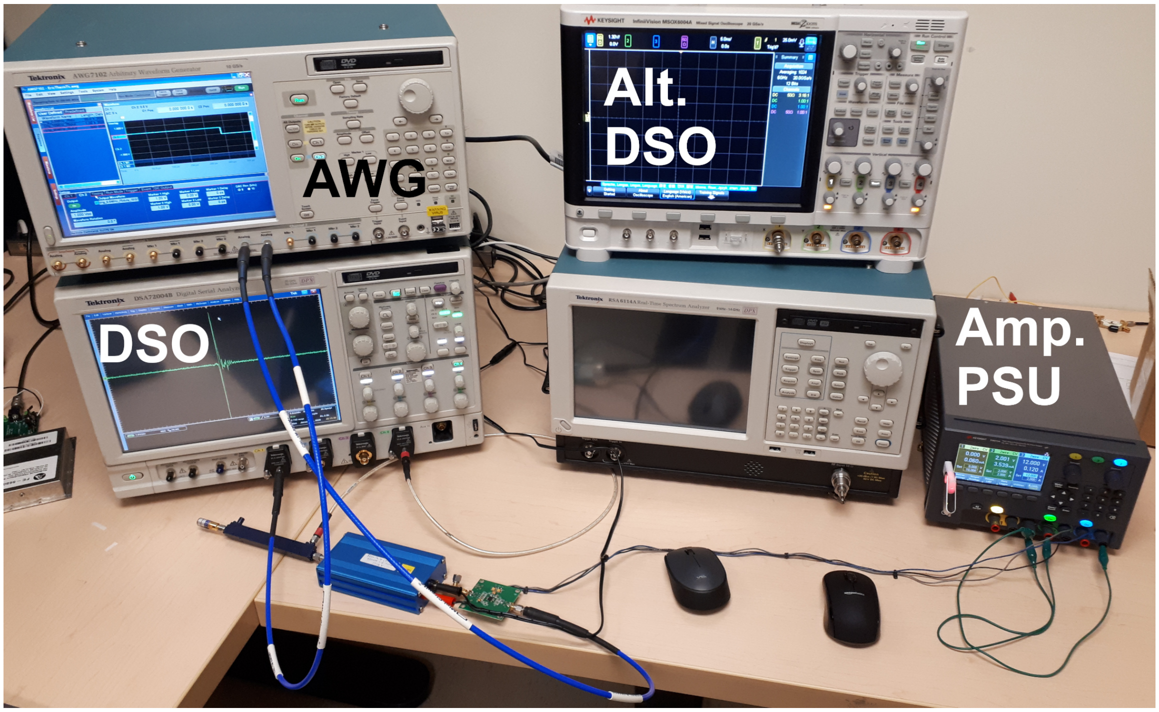

Figure 2.6: Overview of the pulse generator measurement setup. The alternate digital storage oscilloscope (DSO) was used to validate the signal measurements of the main DSO.

2.4.2 Measurement Setup

A certain measurement setup was used to acquire output signals from various generator boards over a range of PRF values. It consisted of specific hardware configured in a specific way as detailed below. Figure 2.6 shows an annotated photograph of the overall measurement setup in operation. Figure 2.7 shows specifically how a pulse generator was connected during testing.

Hardware

The measurement hardware consisted of:

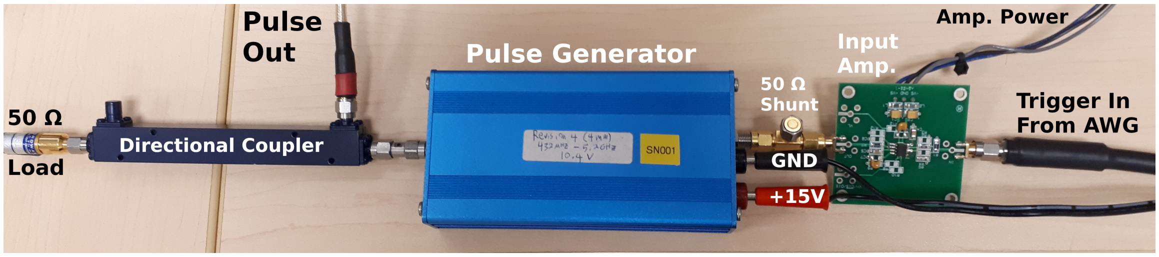

Figure 2.7: Detailed view of a pulse generator as connected during measurements.

- a high-speed DSO[5],
- a wideband directional coupler with −10 dB nominal coupling[6],
- an adjustable DC power supply,
- a 15 V DC fixed power supply with banana plug connectors,
- an arbitrary waveform generator (AWG)[7],
- a custom 20 dB amplifier with 50 Ω input and output impedance[8],
- three short runs of low-loss microwave coaxial sub-miniature A (SMA) cable assemblies with , and
- a handful of SMA adapters for interconnects.

Configuration

The configuration of the DSO is detailed in Table 2.4. The output captured from the DSO was a time-series of voltage samples that represented the pulse signal that

---

[5] Tektronix DSA72004B

[6] RF-Lambda RFDC5M06G10 (https://www.rflambda.com/pdf/directionalcoupler/RFDC5M06G10.pdf)

[7] Tektronix AWG7102

[8] Using the Texas Instruments OPA691 CFB OpAmp (https://www.ti.com/lit/ds/symlink/opa691.pdf)

TABLE 2.4: DSO CONFIGURATION FOR MEASURING THE PULSE GENERATOR OUTPUT.

Setting	Value
Sampling Mode	Real time
Sampling Rate	50 GSPS
Probe Compensation	10 dB
Bandwidth Limit	16 GHz
Record Length (Number of Samples)	2000
Averaging	1024
Trigger Threshold	0 V
Trigger Polarity	Rising edge

would be delivered to a well matched load (50 Ω) from the generator. Averaging was used to reduce the impact of zero-mean stochastic noise and jitter on the measurement and extract the underlying waveform produced by the generator for further analysis.

The AWG was configured to produce a periodic pulse wave at an adjustable PRF with 75% duty cycle (high for 75%, low for 25%), a low voltage of 0 V and a high voltage of 1 V. The duty cycle was empirically adjusted in an attempt to increase the maximum obtainable operating PRF of the generator during measurement. In this way, pulse generator operation of up to at least 20 MHz was obtained. In a more typical digital circuit scenario, the actual duty cycle would instead be closer to 50% unless some form of DDS or other form of waveform shaping were employed. The external custom amplifier was used to produce an output waveform with a low voltage of 0 V and a high voltage of 5 V from the AWG trigger signal. The amplifier output was terminated with 50 Ω using a SMA tee. The voltage levels were chosen for the purposes of mimicking TTL levels which are easily produced using common digital logic circuitry. The amplifier was designed with sufficiently high bandwidth and slew rate to be able to reproduce the sharp edges of the trigger waveform up to 20 MHz.

2.4.3 Design Procedure

Physical prototypes of the pulse generator were incrementally fabricated, tested, and refined in order to obtain improved performance. The basic methodology of this was as follows.

1. Baseline performance was recorded by measuring a prototype of a specific design revision under controlled measurement conditions (see previous sections on performance metrics and measurement setup)
2. The baseline design was modified in a way that changed the experimental variables
3. The performance of the modified prototype was measured under the same measurement conditions used in step 1
4. Compare the performance of the baseline and modified designs
    (a) If the newly observed performance was favourable, the modified design was kept as the new baseline
    (b) Otherwise, the tested design changes were either altered or discarded
5. The process was repeated from step 1 for a number of iterations

The performance of each board was recorded as follows. For each of the desired PRF values,

1. The pulse signal was measured
2. Time-domain performance metrics were derived from the measured pulse

3. The magnitude spectrum of the measured pulse was obtained using FFT
4. Frequency-domain performance metrics were derived from the magnitude spectrum

2.5 Summary of the Designs

The pulse generator was developed into three new PCB revisions through the experimental design procedure, starting from revision 1. Some notes are detailed here for each of the revisions.

2.5.1 Revision 1

The author experimented with existing prototypes of the initial generator design, called revision 1. This was limited to tests that could be performed without modifying the circuit board layout.

The first test was trimming the positions of four potentiometers on the PCB to observe their effects on generator performance. This was done since the potentiometers have been observed to affect peak-to-peak voltage, the level of unwanted ringing and time position of parasitic pulses, and the amplitude and time stability of the generator, although no precise characterization of these effects has been documented at the time of writing.

Another test was varying the DC input voltage to the generator. The DC input voltage was varied in order to observe its effect on the peak-to-peak voltage (also output power), and to make sure that the power supply stage of the generator was operating above the dropout voltage of the voltage regulator.

Finally, some component swapping (testing different component values) and repositioning was investigated. This was done in order to check if bandwidth enhancements or ringing reduction could be achieved without requiring layout modifications in the PCB. Ultimately it was decided that PCB revisions would be needed. The size of the revision 1 PCB is 11.2 cm by 5.33 cm.

2.5.2 Revision 2

Revision 2 is the first new version of the PCB that was created. The following electrical changes were made.

- l_1 was shortened by 1 mm
- D1 was placed 2 mm closer to SRD1 (l_2 decreased by 2 mm)
- overall PCB length was decreased by 3 mm to facilitate the 3 mm decrease in $l_1 + l_2$
- decoupling capacitors C10-C14 were added in order to check whether leakage of RF signals in to the power supply was related to ringing and glitches in the pulse output
- the footprint for connector CP1 was made the same as for CP2 and CP3 so that the same SMA connector part could be used for all three (see Figure 2.5), which simplified the bill of materials (BOM) and reduced total cost

The size of the revision 2 PCB is 10.9 cm by 5.32 cm.

2.5.3 Revision 3

The third revision was changed from revision 2 as follows.

- Components L1 and C3 were replaced with an integrated wideband bias tee (TEE1)[9] and its required capacitor (C15) as it was thought that high-frequency limitations of the discrete bias tee may have been limiting the bandwidth performance.
- Some ICs were slightly relocated, and power supply bypass capacitors were relocated to be closer to IC power pins in order to decrease power supply bypass loop inductance
- The power supply traces were widened to decrease their parasitic resistance and inductance
- CP3 and its feed trace were removed as they are unused, further reducing BOM cost

The size of the revision 3 PCB is 10.9 cm by 5.32 cm.

2.5.4 Revision 4 and Final Design

For revision 4, the only electrical change from revision 3 is the further shortening of l_2. Four versions of revision 4 were fabricated, with $l_2 = 2\,\text{mm}$, $l_2 = 4\,\text{mm}$, $l_2 = 6\,\text{mm}$, and, $l_2 = 7\,\text{mm}$. These variations were pursued in an attempt to observe the effect of l_2 on the output bandwidth and pulse amplitude. The length of each board is slightly different as a result of changing l_2. The final design is taken to be revision 4 with $l_2 = 4\,\text{mm}$. The size of the revision 4 (4 mm) PCB is 10.5 cm by 5.32 cm.

---

[9] Mini-Circuits TCBT-14R+ (https://www.minicircuits.com/pdfs/TCBT-14R+.pdf)

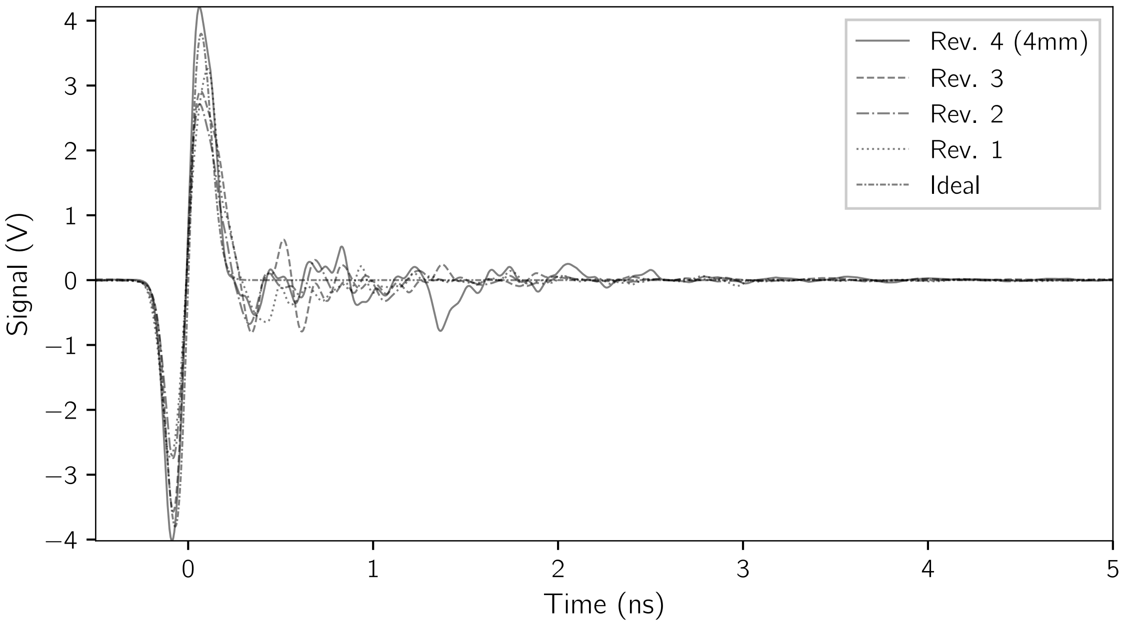

Figure 2.8: Average measured pulse at 5 MHz PRF versus design revision.

2.6 Measured Results

One fabricated prototype per design revision was produced for measurement and performance evaluation. The measured data consist of direct time-domain measurements as well as calculated performance metrics in the time-domain and the frequency-domain. In the time-domain, the measured output signal of each prototype is plotted in Figure 2.8. Performance metrics versus PRF are provided, including peak-to-peak-voltage (Figure 2.9), instantaneous output power (Figure 2.10), average power (Figure 2.11), envelope width (Figure 2.12) and envelope decay time (Figure 2.13). In the frequency-domain, the normalized magnitude spectrum is shown in Figure 2.14 and the −10 dB bandwidth versus PRF is plotted in Figure 2.15.

The plots offer qualitative insight into the performance across revisions and PRF ranges. See Table 2.5 for a quantitative summary of the results at one PRF value.

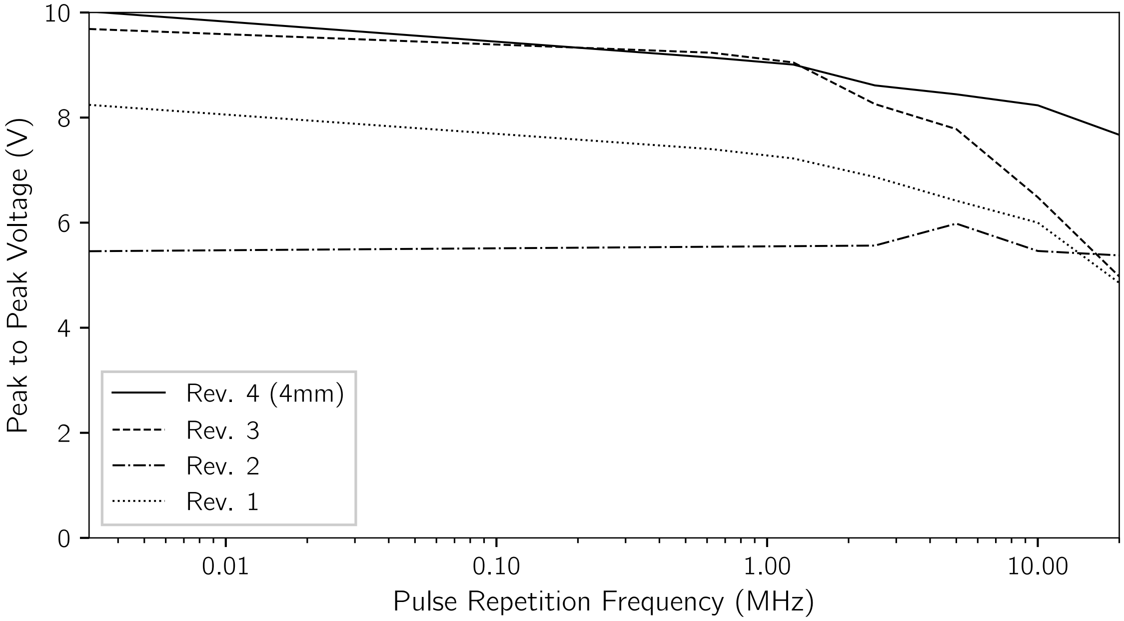

Figure 2.9: Amplitude of measured pulse versus PRF and design revision.

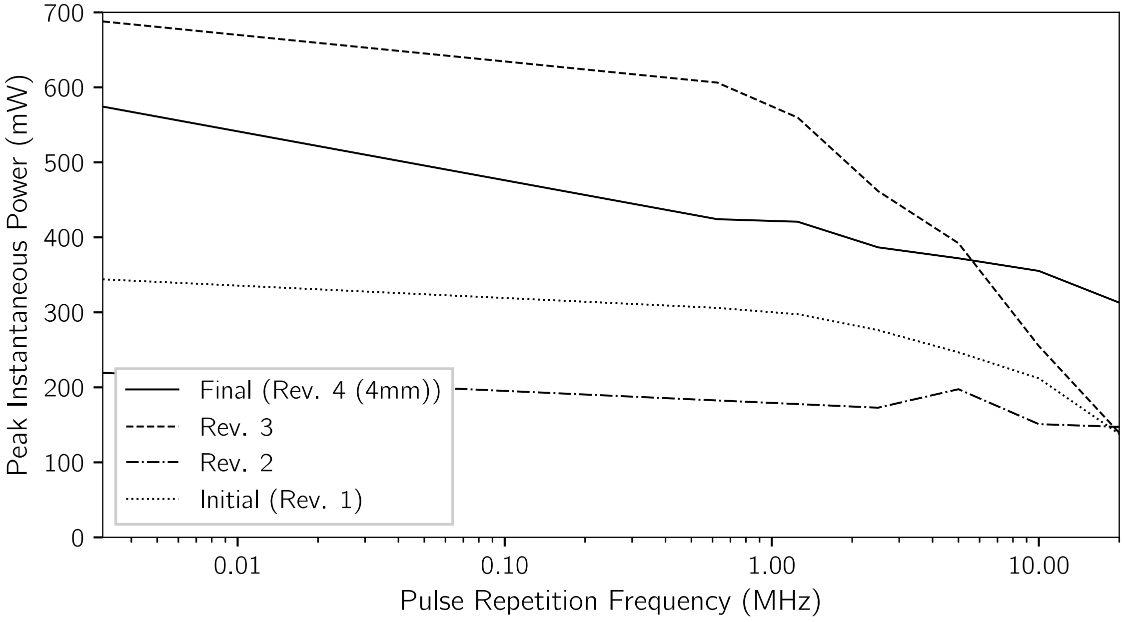

Figure 2.10: Peak power of measured pulse versus PRF and design revision.

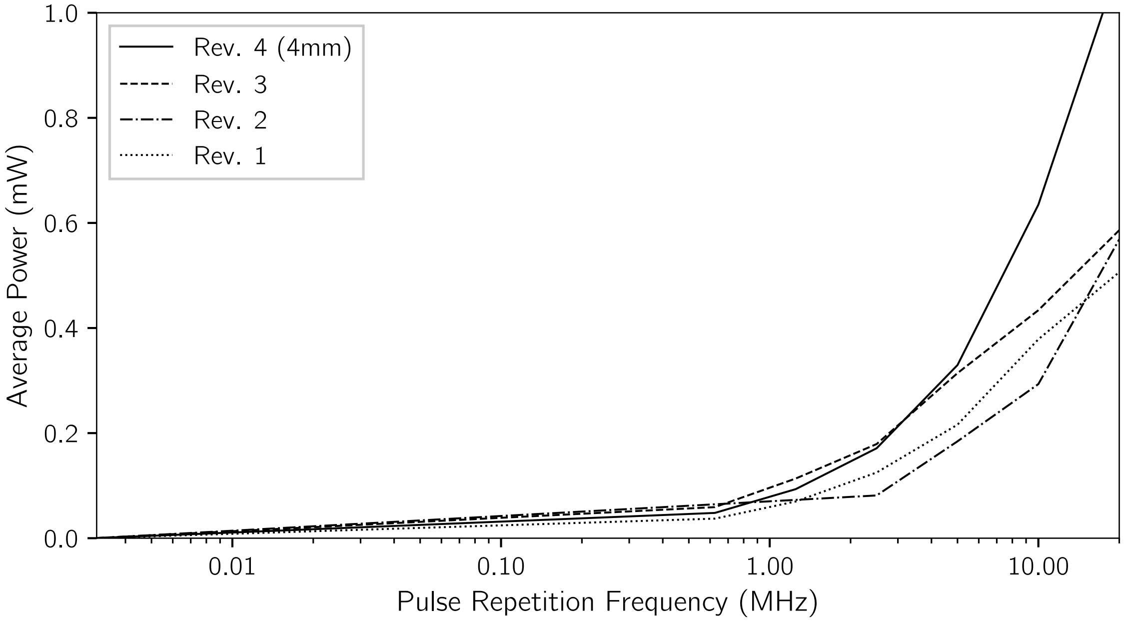

Figure 2.11: Average power of measured pulse versus PRF and design revision.

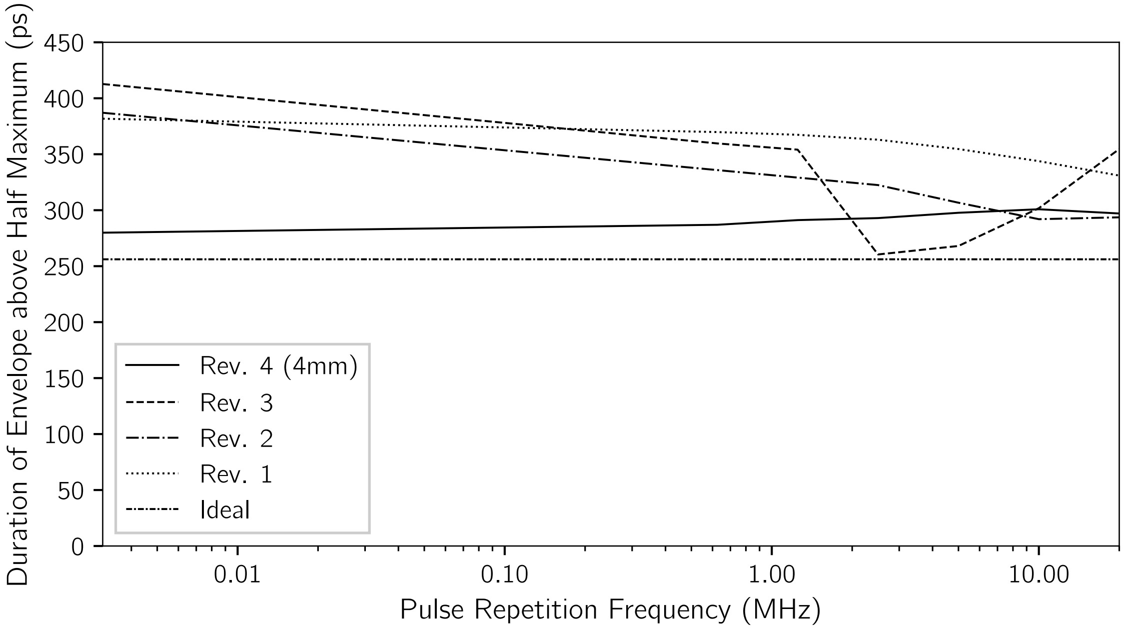

Figure 2.12: Envelope width of measured pulse versus PRF and design revision.

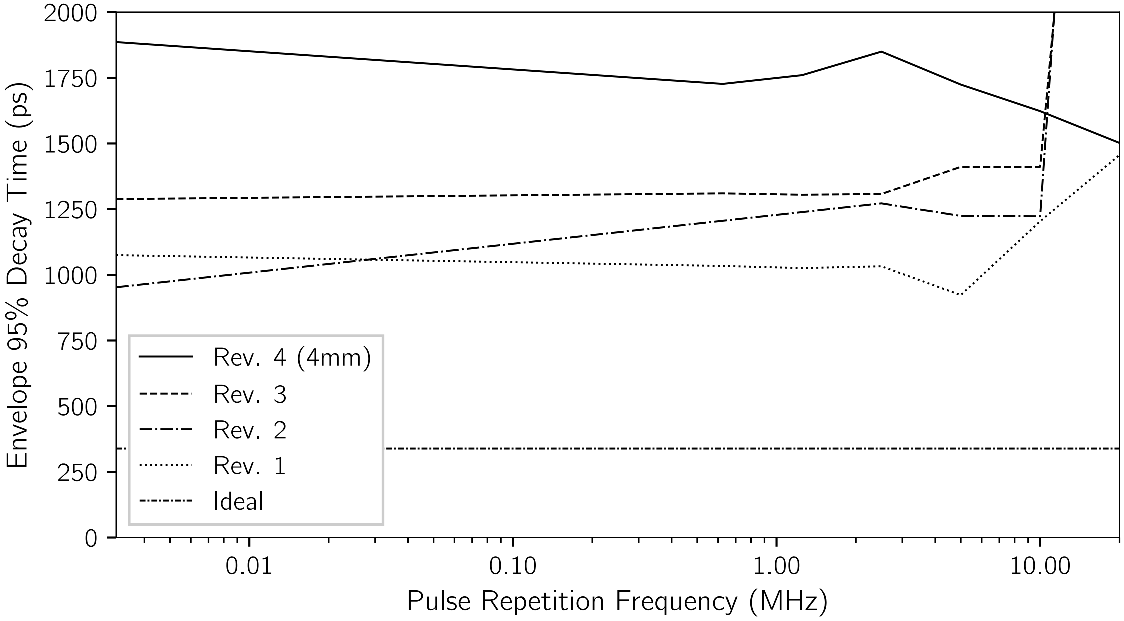

Figure 2.13: 95% envelope decay time of measured pulse versus PRF and design revision.

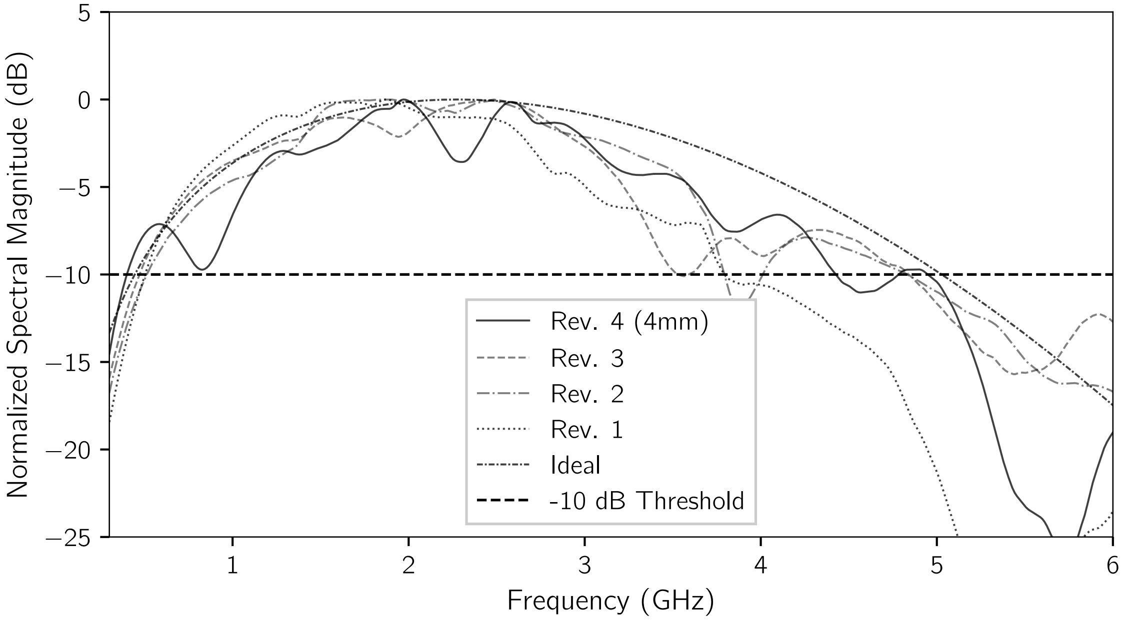

Figure 2.14: Normalized magnitude spectrum at 5 MHz PRF for all revisions.

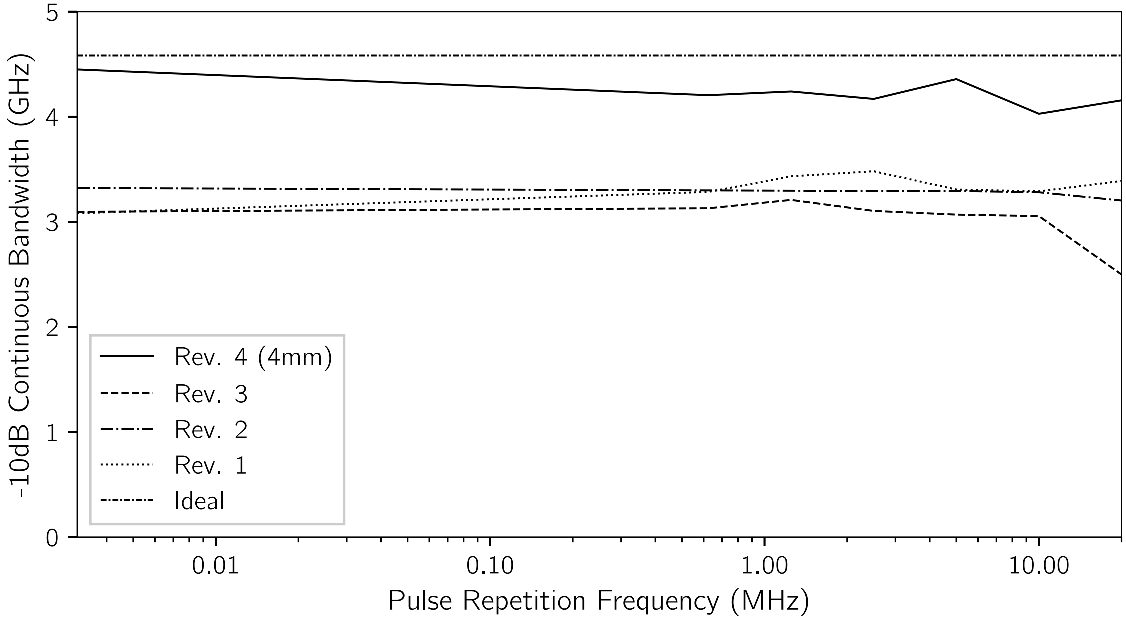

Figure 2.15: Measured pulse bandwidth versus PRF and design revision.

TABLE 2.5: MEASURED PERFORMANCE OF EACH PULSE GENERATOR PROTOTYPE AT 5 MHz PRF COMPARED TO THE EXPERIMENTAL VARIABLES.

Quantity	“Ideal”	Rev. 1	Rev. 2	Rev. 3	Rev. 4 (4 mm)
Peak to Peak Voltage V_{pp} (V)	1532	6.42	5.98	7.78	8.44
Peak Power (W)	11 735	0.247	0.198	0.392	0.372
Average Power P_{av} (mW)	10 000	0.216	0.184	0.314	0.329
Envelope Width t_w (ns)	0.259	0.355	0.307	0.268	0.298
95% Decay Time t_{decay} (ns)	0.342	0.923	1.224	1.411	1.724
-10 dB Bandwidth B (GHz)	4.53	3.31	3.29	3.07	4.36
f_l (GHz)	0.440	0.490	0.486	0.440	0.385
f_u (GHz)	4.98	3.78	3.78	3.51	4.74
l_1 (mm)		36	35	34	29
l_2 (mm)		10	8	8	4
l_3 (mm)		14	9	6	12
Is bias tee replaced?		No	No	Yes	Yes
Substrate Material		RO4350B	RO4003C	RO4003C	RO4003C

2.7 Analysis

When analyzing the data, we keep in mind that only one prototype was measured from each of the design revisions. This is important, since the performance of any fabricated prototype is the result of a stochastic process which itself is a function of electronic component tolerances, fabrication tolerances, and human error in physical component placement. Each of the measurements represent single samples of such a process, whose mean and variance is unknown. In this analogy, the mean represents the expected value of the generator performance, while the variance represents the spread of the performance around the expected value. It is assumed that each design revision would exhibit its own mean and variance, per performance metric. Sufficient data has not been collected to estimate these statistical parameters or their statistical distributions. Thus, with the current data it is impossible to prove the extent to which the positive and negative results have arisen from the actual design changes, as opposed to simple random chance. Nevertheless, for the sake of discussion it is assumed here that at least some component of the observed performance changes truly result from the physical design changes.

Based on the experimental results, the pulse generator performance appears to change with both PRF and design revision. We can identify trends within the performance metrics by examining the plots. For example, pulse magnitude decreases with increasing PRF. This can be seen both in the amplitude plot (Figure 2.9) and peak power plot (Figure 2.10). The trend holds true across all revisions, with slight exception of revision 2. Thus, for large pulse amplitude the PRF should be kept lower. On the other hand, however, we see also that the average output power (Figure 2.11) increases as PRF increases.

Certain changes are easier to see in the tabulated data. At 5 MHz PRF (see Table 2.5) the final design revision (revision 4 (4mm)) appears to have significant performance differences compared to earlier designs. The bandwidth is 31.7% higher than the revision 1 prototype (3.31 GHz versus 4.36 GHz) and closely approaches the specification of 4.5 GHz. The average output power is 52.3% higher than revision 1 (0.329 mW versus 0.216 mW). The final design also exhibits the largest peak-to-peak voltage of any measured prototype. The main disadvantage of the final design is that is has the largest 95% decay time, measuring in at 86.8% longer than in the initial design. This indicates that the duration of the unwanted ringing is longer than any of the other measured prototypes.

It is difficult to establish a precise cause and effect relationship between hardware changes and measured performance as multiple changes have occurred across each revision, and there are only a small number of data points. Nonetheless, some possible relationships are tentatively proposed:

- A decrease in l_2 appears related to increased pulse bandwidth.
- A decrease in l_1 appears weakly related to increased pulse bandwidth.
- A decrease in l_3 appears related to increased pulse bandwidth and reduced pulse amplitude.

It also appears that the inclusion of the integrated bias tee from revision 3 onward has allowed an increase in peak-to-peak amplitude. On the other hand, the bias tee may also have contributed to the bandwidth decrease from revision 2 to revision 3.

A seemingly clear effect is seen from changing the substrate after revision 1. The substrate change appears to have contributed to a decrease in amplitude, peak power, and average power, but also an increase in the envelope decay time. This is expected for two reasons, namely impedance mismatch and loss. The output impedance match is worse with the RO4003C substrate since, as shown in subsection 2.3.2, Z_0 is further away from the $50\,\Omega$ system impedance. This probably contributes to larger reflections at the output port, which reduces the peak of the transmitted pulse and increases internal reflections within the pulse generator. At the same time, the lower loss of the RO4003C substrate attenuates more slowly these internal reflections, leading to a larger and longer "tail" or ringing effect making its way to the output, increasing the envelope decay time (see Figure 2.8).

2.8 Conclusions and Future Work

In this chapter we have followed an empirical investigation of an UWB pulse generator design. The investigation produced a sequence of new hardware revisions, leading to apparently improved performance. The apparent changes in the final design versus the initial design at 5 MHz PRF are as follows:

- Improvements
    1. Absolute −10 dB bandwidth: from 3.31 GHz to 4.36 GHz (31.7% increase)
    2. FoM (fractional bandwidth): from 1.54 to 1.70 (10.4% increase)
    3. Peak-to-peak voltage: from 6.42 V to 8.44 V (31.5% increase)
    4. Peak power: from 247 mW to 372 mW (50.6% increase)
    5. Pulse width: from 355 ps to 298 ps (16% decrease)
    6. PCB area: from 59.7 cm^2 to 55.9 cm^2 (6.4% decrease)

  7. BOM per board from CAD$278 to CAD$249.84 (10% decrease)

- Degradations
  - Envelope decay time: from 0.923 ns to 1.724 ns (46.5% increase)

It appears possible that we have obtained a pulse generator with significantly improved performance in some areas through circuit modifications which did not fundamentally alter the underlying pulse generation topology. We determined this through quantitative and qualitative analysis of the defined performance metrics derived from the experimental data.

A logical next step in the research is to investigate methods to improve the output power. Even after the findings here, the generator output power falls short of the minimum specification of 10 W by a factor of more than 30 000 at 5 MHz PRF. Assuming the same pulse shape and PRF, a sufficiently powerful pulse would require a peak-to-peak voltage of more than 1.47 kV and peak power of 11.3 kW to reach the minimum output power specification. Can the current circuit topology be modified further to produce a strong enough pulse for the desired 20 m detection range, while simultaneously preserving superior bandwidth? To the author, this seems unlikely since SRDs are capable of generating pulses with amplitudes only up to about 200 V [37, p. 49]. On the other hand a RF power amplifier may be able to theoretically supply the required gain (45 dB) but a similar concern holds: can an amplifier be found which can handle the high peak signal? This amplifier needs also an ultra-wide bandwidth, covering at least from 0.5 GHz to 5 GHz. Can such an amplifier be bought off-the-shelf with a price tag and size that are suitable for deployment in the final radar system? This, again, seems unlikely to the author. On the other hand, is a detection range of 5 m perhaps reasonably attainable based on the estimated figures? Such a detection range would require a peak-to-peak voltage of only 91 V and peak power of 44 W based on data in Table 2.1 (21 dB gain needed). Such questions ought to be investigated in the future in order to better approach the output power specifications.

Suppression of the ringing of the generated pulse continues to be an issue for the pulse generator, especially since longer and larger ringing has been observed in the new designs. Specifically, the 95% decay time of the generated pulse appears monotonically increased with each new design revision. Possible sources of the increased ringing are

- change of substrate from revision 1 to revision 2 causing increased internal reflections and lower attenuation of these reflections,
- substitution of bias tee from revision 2 to revision 3 allowing increased leakage of RF signals into driver stage (causing delay of some internal reflections to be longer?), and,
- the ever decreasing distance between D1 and SRD1 (l_2) in new revisions.

These proposed causes remain unsubstantiated until future testing is performed.

Future research should also examine the stochastic nature of the pulse generator performance. An investigation of the statistical performance variation of, say, ten fabricated prototypes of the final and initial design revisions would be useful to either confirm or refute the findings of this thesis. This has not been pursued thus far due to time and funding limits.

References in Chapter 2

[28] J. J. McCombe, “Cognitive microwave radar for the stand-off detection of on-body concealed weapons: Midterm report,” McMaster University, CEM-R- 70, Mar. 2015 (cit. on pp. 10, 11, 31, 38).

[29] J. J. McCombe and N. K. Nikolova, “Transmitter specifications for the stand-off detection of on-body concealed weapons: NATO SPS G4992,” McMaster University, CEM-R- 72, Jul. 2015 (cit. on pp. 10, 11, 31, 32, 34, 36).

[30] A. D. Pitcher, J. J. McCombe, E. A. Eveleigh, and N. K. Nikolova, “Compact transmitter for pulsed-radar detection of on-body concealed weapons,” in *2018 IEEE/MTT-S International Microwave Symposium-IMS*, IEEE, 2018, pp. 919–922 (cit. on pp. 13, 23, 35).

[32] Industry Canada, “Radio standards specification RSS-220, issue 1, devices using ultra-wideband (UWB) technology,” Jul. 2018. [Online]. Available: https://www.ic.gc.ca/eic/site/smt-gst.nsf/eng/sf09347.html (cit. on pp. 21, 78).

[33] United States of America, “Title 47 CFR part 15, subpart F–ultra-wideband operation, §15.503,” May 2002. [Online]. Available: https://www.ecfr.gov/cgi-bin/text-idx?node=pt47.1.15#sp47.1.15.f (cit. on pp. 21, 78).

[34] “UWB regulations, A summary of worldwide telecommunications regulations governing the use of ultra-wideband radio,” Application Note: APR001, English, version 1.2, 2015. [Online]. Available: https://www.decawave.com/sites/default/files/apr001_uwb_worldwide_regulations_summaryrev1.2.pdf (cit. on pp. 21, 78).

[35] S. Haykin and B. Van Veen, *Signals and Systems*, 2nd ed., ser. Wiley Series in Microwave and Optical Engineering. 111 River Street, Hoboken, NJ 07030-5774: John Wiley & Sons, Feb. 2002, ISBN: 0-471-16474-7 (cit. on p. 21).

[36] H. Schantz, *The Art and Science of Ultrawideband Antennas*, 1st ed., ser. Artech House Antennas and Propagation Library. 685 Canton Street Norwood, MA 02062: Artech House, 2005 (cit. on pp. 21, 22, 23, 33, 70, 71, 72, 73, 74, 75, 76).

[37] F. Nekoogar, *Ultra-wideband Communications, Fundamentals and Applications*, 1st ed., ser. Prentice Hall Communications Engineering and Emerging Technologies Series. One Lake Street, Upper Saddle River, NJ 07458: Prentice Hall, Sep. 2005, ISBN: 0-13-146326-8 (cit. on pp. 21, 22, 23, 38, 60).

[38] J. Sachs, *Handbook of Ultra-Wideband Short-Range Sensing: Theory, Sensors, Applications*, 1st ed. Boschstr. 12, 69469 Weinheim, Germany: Wiley-VCH, 2012 (cit. on pp. 22, 28, 33, 75, 76, 79).

[39] T. Zwick, W. Wiesbeck, J. Timmermann, and G. Adamiuk, Eds., *Ultra-wideband RF System Engineering*, 1st ed., ser. EuMA High Frequency Technologies Series. Cambridge CB2 8BS, United Kingdom: Cambridge University Press, 2013 (cit. on pp. 22, 28, 29, 79).

[40] I. Oppermann, M. Hämäläinen, and J. Iinatti, Eds., *UWB Theory and Applications*, 1st ed. The Atrium, Southern Gate, Chichester, West Sussex PO19 8SQ, England: John Wiley & Sons, Oct. 2004, ISBN: 0-470-86917-8 (cit. on p. 22).

[41] E. W. Weisstein. (2020). “Gamma function.” From MathWorld–A Wolfram Web Resource, Wolfram Mathworld, [Online]. Available: http://mathworld.wolfram.com/GammaFunction.html (cit. on p. 23).

[42] P. Protiva, J. Mrkvica, and J. Macháč, “Universal generator of ultra-wideband pulses,” *Radioengineering*, vol. 17, no. 4, pp. 74–78, 2008 (cit. on pp. 23, 35, 36, 38).

[43] ——, “A compact step recovery diode subnanosecond pulse generator,” *Microwave and optical technology letters*, vol. 52, no. 2, pp. 438–440, 2010 (cit. on pp. 23, 35).

[44] G. Avdeyenko, “Simulation and development of impulse ultrawideband signal generators for wireless communication systems,” in *2018 International Scientific-Practical Conference Problems of Infocommunications. Science and Technology (PIC S T)*, Oct. 2018, pp. 349–353. DOI: 10.1109/INFOCOMMST.2018.8632056 (cit. on pp. 23, 35, 36).

[45] G. V. Fierro and G. E. Flores-Verdad, “A CMOS low complexity gaussian pulse generator for ultra wideband communications,” in *2009 52nd IEEE International Midwest Symposium on Circuits and Systems*, Aug. 2009, pp. 70–73. DOI: 10.1109/MWSCAS.2009.5236151 (cit. on pp. 23, 35).

[46] W. Feng, N. Li, and X. Li, “A 3–5 GHz UWB impulse generator in 0.13 µm CMOS,” *Microwave and Optical Technology Letters*, vol. 58, no. 9, pp. 2242–2245, 2016 (cit. on pp. 23, 35, 36).

[47] I. Mahbub, S. K. Islam, and A. Fathy, “Impulse radio ultra-wideband (IR-UWB) transmitter for low power low data rate biomedical sensor applications,” in *2016 IEEE Topical Conference on Biomedical Wireless Technologies, Networks, and Sensing Systems (BioWireleSS)*, Jan. 2016, pp. 88–90. DOI: 10.1109/BIOWIRELESS.2016.7445570 (cit. on pp. 23, 35).

[48] W. I. Jang, W. S. Choi, T. O. Kong, M. C. Park, and Y. S. Eo, "A power efficient impulse generator for 6-9 GHz UWB applications," *Microwave and Optical Technology Letters*, vol. 61, no. 3, pp. 587–591, 2019 (cit. on pp. 23, 35, 36).

[49] C. Fang, C. L. Law, and J. Hwang, "High-voltage high-efficiency ultrawideband pulse synthesizer," *IEEE Microwave and Wireless Components Letters*, vol. 20, no. 1, pp. 49–51, 2010 (cit. on pp. 25, 35, 36).

[50] C. Fang, C. L. Law, J. Hwang, and J. Xia, "Design and analysis of high-voltage high-efficiency ultra-wideband pulse synthesizer," *Progress In Electromagnetics Research C*, vol. 20, pp. 187–201, 2011 (cit. on pp. 25, 35).

[51] K. Kim, S. Kim, M. Park, J. Choi, B. Koo, and P. Park, "A high voltage GaN impulse generator for human detection UWB radar sensor," in *2017 14th International Conference on Ubiquitous Robots and Ambient Intelligence (URAI)*, Jun. 2017, pp. 527–528. DOI: 10.1109/URAI.2017.7992660 (cit. on pp. 25, 35).

[52] J. Xia, C. L. Law, Y. Zhou, and K. S. Koh, "3–5 GHz UWB impulse radio transmitter and receiver MMIC optimized for long range precision wireless sensor networks," *IEEE Transactions on Microwave Theory and Techniques*, vol. 58, no. 12, pp. 4040–4051, 2010 (cit. on pp. 25, 35, 36).

[53] M. A. H. Ansari and C. L. Law, "High voltage high efficiency UWB pulse generator for precision localization wireless sensor network," in *2016 International Symposium on Integrated Circuits (ISIC)*, Dec. 2016, pp. 1–4. DOI: 10.1109/ISICIR.2016.7829696 (cit. on pp. 25, 35).

[54] F. Zito, D. Zito, and D. Pepe, “Uwb 3.1-10.6 GHz CMOS transmitter for system-on-a-chip nano-power pulse radars,” in *2007 Ph.D Research in Microelectronics and Electronics Conference*, 2007, pp. 189–192 (cit. on p. 35).

[55] S. Bourdel, Y. Bachelet, J. Gaubert, R. Vauche, O. Fourquin, N. Dehaese, and H. Barthelemy, “A 9-pJ/pulse 1.42-Vpp OOK CMOS UWB pulse generator for the 3.1–10.6-GHz FCC band,” *IEEE Transactions on Microwave Theory and Techniques*, vol. 58, no. 1, pp. 65–73, 2010 (cit. on p. 35).

[56] J. B. Radic, A. M. Djugova, and M. S. Videnovic-Misic, “A 3.1–10.6 GHz impulse-radio UWB pulse generator in 0.18µm,” in *2011 IEEE 9th International Symposium on Intelligent Systems and Informatics*, 2011, pp. 335–338 (cit. on p. 35).

[57] M. J. Copps and K. J. Martin, “First report and order in the matter of revision of part 15 of the commission’s rules regarding ultra-wideband transmission systems,” United States Federal Communications Commission, FCC 02-48, Apr. 2002 (cit. on p. 35).

[58] D. Oloumi and E. Fear, “A picosecond pulse generator using srd diodes: Design, analysis, and measurements,” in *2018 USNC-URSI Radio Science Meeting (Joint with AP-S Symposium)*, 2018, pp. 159–160 (cit. on p. 35).

[59] M. Jafari and S. V. Mir-Moghtadaei, “A uwb pulse generator with step recovery diode (srd) for the characterizing and evaluation of materials using dielectric spectroscopy,” in *2019 27th Iranian Conference on Electrical Engineering (ICEE)*, 2019, pp. 427–430 (cit. on p. 35).

[60] (Oct. 29, 2019). “Coplanar waveguide with ground calculator.” English, Chemandy Electronics Ltd, [Online]. Available: https://chemandy.com/calculators/coplanar-waveguide-with-ground-calculator.htm (visited on 03/25/2020) (cit. on p. 40).

[61] B. Spokoinyi. (2020). “CPW (grounded) line calculator.” English, Spok Engineering Consulting, [Online]. Available: http://spok.ca/index.php/resources/tools/99-cpwcalc (visited on 03/25/2020) (cit. on p. 40).

Chapter 3

Development of the Ultra-wideband Antenna Element

3.1 Introduction

An initial prototype antenna element was developed prior to this thesis for use in the concealed weapons detection (CWD) radar project. The prototype is a modified printed circuit board (PCB) ultra-wideband (UWB) "cactus" antenna. Some examples of cactus antennas from the literature are found in [62]–[67].

Antennas shown in [65] and [67] demonstrate impedance bandwidth ratios of up to 4:1. The measured impedance bandwidth ratio is less than 2:1 for the previously developed CWD project antenna, which also happens to fall significantly short of project requirements. Topological modifications of the CWD antenna such as the addition of a metallic cavity backing, and the reduction of relative ground plane and substrate size are factors in the noted bandwidth disparity. These modifications reflect design goals of the CWD project antenna, which include suppression of back radiation, antenna compactness, and wide impedance bandwidth. The initial prototype of the CWD antenna succeeds in the first two design goals, while falling short of the third goal as just noted. Even the cited designs in the literature do not meet the impedance bandwidth goal of the CWD project, which is to achieve a 10:1 ratio in a specific frequency band. Thus, meeting the bandwidth goal is an evidently difficult task.

Research efforts were undertaken by the author to improve the CWD antenna element performance. The main purpose of this research was to create a modified version of the antenna prototype with enhanced impedance bandwidth to more closely match the design goals. It was hypothesized that the impedance bandwidth could be improved by modifying the shape of the antenna metallization, including the feed structures of the antenna.

In this chapter, the aforementioned research efforts and results are presented. Initially, the specifics of the antenna specifications are outlined. Then, the design methods are provided, with some intermediate designs touched upon as examples of the design process. Afterwards, the simulated performance of both the initial and final designs is presented using plots of impedance matching and far-field parameters. Then, measurement results of fabricated antenna prototypes are used to verify the simulation results and to characterize the real-world performance of initial and final designs. Finally, conclusions are drawn about outcome of the research efforts. At the end of the thesis in Appendix B, replication instructions for the initial and final antenna designs are detailed such that the antennas can be precisely re-created in electromagnetic (EM) simulators or for further fabrication.

Before delving into the details of this research, an overview of related antenna concepts are presented.

3.1.1 Fundamental Antenna Parameters

"Traditionally, engineers study antennas from the 'frequency-domain' point of view" [36, p. 37]. In the frequency-domain, antenna performance is usually specified in terms of standardized parameters [68], [69]. A detailed treatment of antenna parameters is found in [70, chap. 2] which draws definitions directly from the relevant standard [68] of the Institute of Electrical and Electronics Engineers (IEEE). At the time of writing, the most up-to date version of this IEEE standard is [69]. Most of the standard antenna parameters characterize the radiation properties of antennas, while some others relate to the antenna port behaviour.

Radiation Parameters

Radiation parameters describe the antenna radiated electromagnetic fields when driven with a certain, usually sinusoidal, input signal. The parameters may describe the directional distribution of an antenna's

- radiation power density,
- radiation intensity,
- gain & directivity, or
- polarization.

The sinusoidal input signal is of a certain frequency (f) and root-mean-square (RMS) power. Thus, the parameters are generally functions of frequency and power. They also depend on the angular direction relative to the antenna coordinate system. A spherical coordinate system is convenient in this situation, where direction from the antenna origin is specified in terms of azimuth (ϕ) and elevation (θ) angles [70, p. 27]. Some parameters depend also on the radial distance from the antenna (r), an example being the radiation power density which follows an inverse square law [36, p. 52]. Thus, the radiation parameters are functions of 2, 3 or even 4 variables. In the narrowband case, the radiation parameters "are essentially constant" [36, p. 55] within the antenna operating band. In such a case, the parameters depend mostly on azimuth, elevation, and, possibly, radial distance. In the general, wideband case, however, this assumption does not hold and the parameters are expected to exhibit significant changes across the antenna's operating band.

In order to present the radiation parameters in print media such as this document, it is necessary to distil down the data such that it can be plotted in 2D.

One option is to examine each parameter in a specific set of planes. The resulting plots are called plane cuts. Each plane cut is then a function of the independent angle, frequency, and, possibly, radial distance. In this approach, a discrete set of frequencies and planes is selected over which to plot or measure the data. Then, the parameters are determined for each frequency point over the entire range of the independent angle in each plane. Cuts are usually made in the x-y plane (θ=90°, azimuth) and x-z plane (ϕ=0°, elevation) [70, p. 33] as well as the y-z plane (ϕ=90°, elevation).

A second option is to project a view (or number of views) of the parameter, plotted as a 3D surface in spherical coordinates (a 3D pattern), into a 2D image for a number of frequency points. In this way the reader is able to appreciate the overall "shape" of the parameter versus direction and how it changes over frequency in a qualitative way.

Port Parameters

Antenna port parameters describe the antenna's behaviour as part of a circuit or microwave network. A primary port parameter is the antenna input impedance, defined as "the impedance presented by an antenna at its terminals" [69, p. 19] when driven with a sinusoidal signal. More concretely, "the impedance of an antenna is the ratio (Z_A) of the electric to magnetic fields at the antenna's terminals" [36, p. 78] if it is fed by a transverse-electric-magnetic (TEM) transmission line. This quantity is an intrinsic property of the antenna and its feed geometry that is independent of the system to which the antenna is a part of. Mathematically, it is defined [70, pp. 80-81] as

$$Z_A = R_A + \jmath X_A \tag{3.1}$$

where R_A and X_A are the antenna input resistance and reactance, respectively. It is important to note that *both* components of the antenna impedance are generally strong functions of frequency, and this has important system design ramifications (see subsection 3.1.2).

3.1.2 Impedance Matching

Impedance matching is an important system property which depends on the antenna port characteristics (input impedance) and the system characteristic impedance. Since the antenna input impedance may vary strongly with frequency, while the system impedance remains mostly constant, antenna impedance matching is also a function of frequency. There are at least four equivalent ways in which impedance matching of an antenna is quantified in practice, all based on the antenna reflection coefficient.

Reflection Coefficient, Return Loss, and SWR

Reflection coefficient magnitude, return loss, and standing wave ratio (SWR) are three equivalent ways of examining the impedance matching of an antenna within a system. First, the antenna reflection coefficient (Γ) is understood through transmission line theory [71, chap. 2] as the complex-valued voltage reflection coefficient at the antenna terminals. From [36, p. 78] we have that

$$\Gamma = \frac{Z_A - Z_0}{Z_A + Z_0} \tag{3.2}$$

where Z_A is the antenna input impedance and Z_0 is the characteristic impedance of the feed line. A smaller reflection coefficient magnitude ($|\Gamma|$) indicates better impedance matching since less incident power is reflected back to the generator in transmitting mode.

Second, return loss is used to indicate $|\Gamma|$ ($|\mathrm{S}_{11}|$) as a positive loss value [71], [72]. The formula for return loss is

$$\text{return loss} = 20\log_{10}\frac{1}{|\Gamma|} = -20\log_{10}|\Gamma| \tag{3.3}$$

whereby a larger loss value indicates better impedance matching as more power has been lost to the antenna as either radiation or heating.

A third indicator of impedance matching is SWR, which partly describes the standing wave that occurs within a transmission line due to the reflected power wave.

The formula for SWR is

$$\mathrm{SWR} = \frac{1 + |\Gamma|}{1 - |\Gamma|} \tag{3.4}$$

as shown, for example, in [36], [71], [72]. A lower SWR value indicates a lesser presence of standing waves in the transmission line and thus a better impedance match.

Impedance Mismatch Factor (Efficiency)

Finally, the impedance mismatch factor is "the ratio of the power accepted by an antenna to the power incident at the antenna terminals from the " and it is

$$e_r = 1 - |\Gamma|^2 \tag{3.5}$$

which can be seen as the efficiency of power transfer from the transmission line to the antenna. Indeed, some (i.e. [70, p. 65], [36, pp. 287, 288]) treat this as a component of antenna efficiency, and call it either mismatch efficiency or reflection efficiency.

3.1.3 Antenna Bandwidth

Antenna bandwidth is a very important topic for UWB antennas. It is the large bandwidth that distinguishes UWB antennas from narrowband antennas [36, p. 31]. In order to formally draw this distinction, antenna bandwidth must first be defined.

The bandwidth of an antenna is "the range of frequencies within which the performance of the antenna conforms to a specified standard with respect to some characteristic" [69, p. 7]. When defined in this way, bandwidth cannot be characterized uniquely [70, p. 70]. Generally, the antenna bandwidth is either specified in terms of a radiation property (i.e. pattern, gain, polarization) or in terms of impedance matching (see [70, p. 70] and [36, p. 40]). These are usually called pattern bandwidth and impedance bandwidth, respectively [36], [70]. Another form of bandwidth is the radiated bandwidth [36, p. 41] which depends on the antenna input signal. Regardless of which way bandwidth is defined, its limits are specified by its lower and upper frequency points. These points are used to calculate the absolute and relative bandwidths.

Absolute versus Relative Bandwidth

Absolute bandwidth is simply the difference between the upper and lower frequency points [38, p. 8]. Using the notation from [38] that is,

$$B = f_u - f_l \tag{3.6}$$

where f_u and f_l are the upper and lower frequencies. An antenna operates adequately with respect to a specified parameter over at least as much spectrum as the absolute bandwidth reports.

Two forms of relative bandwidth are the fractional bandwidth and the frequency ratio. The fractional bandwidth is simply the absolute bandwidth divided by the centre frequency [36], [38]. Depending on the definition, the centre frequency is the arithmetic mean of the upper and lower frequencies or, less often, the geometric mean [36, p. 39]. With the more common (yet less physically meaningful [36, p. 39]) definition we have the following:

$$f_c = \frac{f_u + f_l}{2} \tag{3.7}$$

$$b_{\mathrm{f}} = \frac{B}{f_c} = 2\frac{f_u - f_l}{f_u + f_l}. \tag{3.8}$$

The frequency ratio is the ratio of the upper to lower frequency [38], that is

$$b_{\mathrm{fr}} = \frac{f_u}{f_l} \tag{3.9}$$

and it is often expressed in the form of $b_{\mathrm{fr}} : 1$ such as $10 : 1$ (a decade bandwidth) or $2 : 1$ (an octave bandwidth) [36].

An antenna may have multiple frequency ranges wherein it performs adequately. In such a case, there are multiple possible pairs of f_u and f_l, one for each band, so the absolute and relative bandwidths are not uniquely defined. We may select one of these bands, say whichever has the maximum bandwidth, and use that to report the antenna absolute and relative bandwidths. Nevertheless, an antenna may still perform adequately within other frequency bands that do not get reported. This suggests that absolute and relative bandwidth figures do not necessarily portray the full extent of an antenna's spectral performance.

Band Coverage

Antenna band coverage is an alternate indicator of antenna performance within a specific desired operating band. Consider a scenario where the desired operating band contains 1 GHz of bandwidth. Consider further that an antenna is measured as operating adequately over 0.75 GHz of spectrum *in total* between the upper and lower frequency bounds of the desired operating band. We can then say that the band coverage of this specific antenna is 75% ($\frac{0.75\,\mathrm{GHz}}{1\,\mathrm{GHz}} \times 100\%$) given the desired operating band.

The author believes that evaluation of band coverage facilitates a concise, like-for-like comparison of multiple antennas when considering their operation within the desired band. Whether an antenna operates adequately over a single continuous frequency range (one pair of f_u and f_l), or over multiple such ranges (multiple pairs of f_u and f_l), the band coverage figure is defined unambiguously if specific performance criteria are commonly defined and used. This is in contrast to the potential lack of uniqueness of the absolute and relative bandwidth figures.

Impedance Bandwidth

The impedance bandwidth may be specified by applying a threshold constraint to the reflection coefficient magnitude, return loss, or SWR value. For example, let f_u and f_l be those frequencies that bound a frequency band wherein the reflection coefficient magnitude is less than or equal to some fixed value in dB or, equivalently, wherein the SWR is less than or equal to some fixed value. In this way, we can determine absolute and relative impedance bandwidths by Equation 3.6, Equation 3.8, and Equation 3.9. There may be multiple possible pairs of f_u and f_l for a given antenna, caused in this case when the reflection coefficient or SWR crosses the performance threshold more than twice within the measurement. Then the impedance bandwidth is not unique for the particular antenna. In response, we may also examine the impedance-matched band coverage. The impedance-matched band coverage is determined by finding the total amount of spectrum over which a given antenna satisfies the threshold constraint on reflection coefficient magnitude, return loss, or SWR within the bounds of the desired operating band.

UWB Bandwidth

Another form of bandwidth is the UWB bandwidth. The so-called UWB bandwidth is distinct in that it is not a property of the antenna itself, but also of other system components. As decreed by the United States Federal Communications Commission (FCC), “the UWB bandwidth is the frequency band bounded by the points that are 10 dB below the [frequency of] highest radiated emission, as based on the complete transmission system including the antenna” [33, §15.503]. The actual “radiated emission” is a function of the properties of the antenna, the transmitter (Tx) that the antenna is connected to, and the interconnects between these components. The UWB bandwidth is defined similarly within the corresponding Canadian regulations [32].

UWB bandwidth is used to characterize UWB transmitting systems from the regulatory perspective. For the United States, “[an] ultra-wideband (UWB) transmitter [is] [an] intentional radiator that, at any point in time, has a fractional bandwidth equal to or greater than 0.20 or has a UWB bandwidth equal to or greater than 500 MHz, regardless of the fractional bandwidth” [33, §15.503]. Again, the Canadian definition is essentially identical to that of the United States. A summary with other worldwide UWB regulations can be found in [34].

At the stage where regulatory compliance is a concern, characterizing the UWB bandwidth of the transmitting system is paramount, along with ensuring that the emission limits specified in [33], [32] or [34] are satisfied depending on the intended country of deployment. The figures are not to be determined by examining individual system components, rather, they are to be determined using measurements of the fully operational transmission system as prescribed by the aforementioned regulatory documents.

3.1.4 Time-Domain Performance

UWB antennas are distinct from narrowband antennas in that they are often employed to radiate signals with very large instantaneous bandwidths such as sub-nanosecond pulses as opposed to sinusoid-like signals. The spectrum of the transmitted and received signals may be less important than the actual shape in the time-domain. For example, in situations such as UWB radar, the time shape of the received pulse is important as it effects range resolution (see [38], [39]). In UWB radio transmission, some time-domain parameters of an impulse excited antenna are

- impulse response function (IRF) [39, pp. 18, 19, 38–43],
- analytic envelope of the IRF [39, p. 19],
- peak value of the envelope [39, p. 20],
- envelope width [39, pp. 20],
- ringing [39, p. 20], and,
- fidelity [39, p. 22].

Antenna IRF is the primary parameter from which other parameters are derived. The antenna IRF along reference boresight may be derived through Fourier theory from vector network analyzer (VNA) measurements of the free-space transmission coefficient between two identical antennas [39, p. 38] while considering the linear model of the propagation channel, including both antennas [39, pp. 7-8]. Such measurement must be performed in an anechoic chamber.

3.2 Antenna Element Specifications and Prior Designs

An antenna is required that can serve as a transmitting and receiving element for a dual-polarization radar system. The antenna must be well-matched over the desired operating band and exhibit predominantly forward-looking radiation patterns. It must able to be easily configured for dual-polarization operation, in that pairs of antennas can be made to produce complementary polarizations (i.e. horizontal polarization and vertical polarization, left-handed circular polarization (LHCP) and right-handed circular polarization (RHCP), or dual elliptical polarizations). The envisioned system uses four such antennas in an unconventional two by two panel (see Figure 3.1). Each antenna will have its own independent feed port so this is not an array in the traditional sense. Two antennas will be used in transmitting mode, while the other two will be used in receiving mode. The antennas will be configured such that co-and cross-pol backscatter can be measured by the radar. By operating one Tx at a time, four different backscatter quantities will be available: co-pol to co-pol, co-pol to cross-pol, cross-pol to cross-pol, and cross-pol to co-pol. This permits additional target information to be obtained and used for classification when compared with a single-polarization system.

The specifications of the antenna element are discussed next, followed by a comparison of these specifications with designs from the literature.

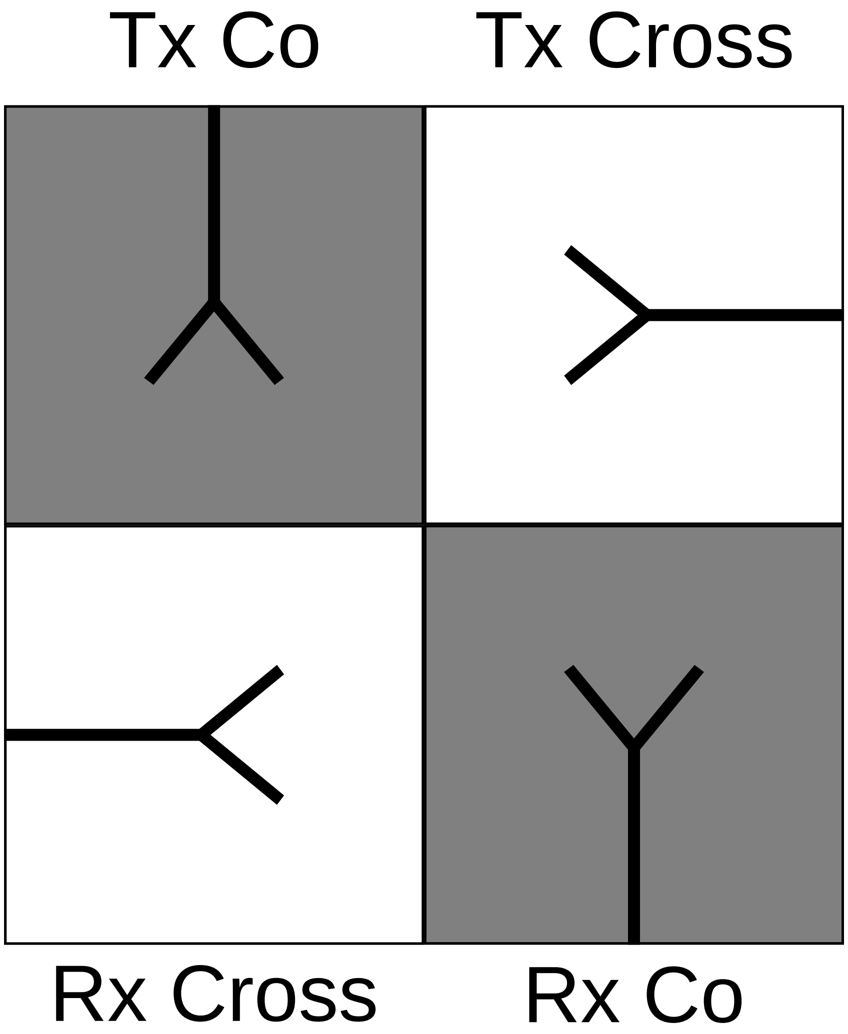

Figure 3.1: Diagram representing an envisioned 2 by 2 antenna panel for dual-polarization short-range radar. Each fork shape represents an antenna, with the narrow end being the feed location. The rotation of the forks represents how antennas might be oriented to produce co- (gray) and cross- (white) polarizations.

3.2.1 Impedance Matched Band

The antenna should operate in the frequency band from 0.5 GHz to 5 GHz. In this band, the reflection coefficient should be at most $-10\,\mathrm{dB}$ in magnitude. Thus, one of the design specifications requires $|\Gamma| \leq -10\,\mathrm{dB}$ from 0.5 GHz to 5 GHz.

3.2.2 Size

The antenna size should be less than 15 cm in width by 15 cm in length by 8 cm in depth. This accounts for an antenna which includes cavity backing.

3.2.3 Radiation Characteristics

The radiation patterns should be primarily directed forwards. A broad forward pattern is desirable while, at the same time, back radiation is reasonably suppressed. Ideally, the antenna will be linearly polarized. A pattern that does not change over frequency would be preferred but, unfortunately, this is not feasible.

3.2.4 Material Composition and Cost

The antenna should be constructed out of a low-cost materials, such as Flame Retardant 4 (FR-4) laminate, which also offers ease of fabrication. The antenna is to be fed with a sub-miniature A (SMA) connector.

3.2.5 Figure of Merit

A simple figure of merit (FoM) for comparing the wideband impedance matching of antennas can be defined based on the fractional impedance bandwidth (see subsection 3.1.3) and antenna electrical size. We first consider the fractional impedance bandwidth and how it changes. Then, we consider a definition of antenna electrical size and how that changes. Finally, the two figures are combined to form the overall FoM.

The fractional impedance bandwidth is the ratio of the absolute impedance bandwidth to the centre frequency of the impedance-matched band. If the antenna impedance bandwidth is doubled, but the centre frequency stays constant, the fractional impedance bandwidth becomes doubled. Likewise, if the centre frequency is doubled, but impedance bandwidth remains constant, the fractional impedance bandwidth is halved. If, therefore, both of these changes are implemented at the same time, the fractional impedance bandwidth remains the same. Fractional impedance bandwidth itself can be seen as a FoM itself, with a larger value being more desirable. In this way, we can see that the significance of the antenna impedance bandwidth is not just based on its absolute value, but where it resides in the frequency spectrum.

The antenna electrical size can be characterized as the ratio of the radius of the smallest sphere that can completely enclose the antenna to the free-space wavelength radiated by the antenna at a particular frequency. If the radius is doubled but the wavelength remains the same then the electrical size becomes doubled. Similarly, if the wavelength is doubled (frequency halved), but the radius remains the same the electrical size is halved. When both of these changes happen at the same time, the antenna electrical size remains constant. For an UWB antenna, we will consider the

TABLE 3.1: COMPARISON OF EXISTING ANTENNAS' MEASURED PERFORMANCE TO THE DESIGN SPECIFICATIONS

Reference	f_l (GHz)	f_u (GHz)	b_{fr}	Area (cm^2)	R (cm)	Substrate Material	ϵ_r	FoM
[65]	3	12	1.2	8.96	2.26	LCP	3	17.7
[66]	2.1	11.7	1.39	5.6	1.98	LCP	3	33.46
[73]†	0.3	3	1.636	1029	32.07	RT5880	2.2	17
Ideal	0.5	5	1.636	225	11.3	FR-4	4.4	28.96

†Simulated results

lowest frequency of operation when evaluating the electrical size.

The FoM is defined as the product of the fractional impedance bandwidth and the reciprocal of the antenna electrical size. Mathematically this is

$$\text{FoM} = \frac{B}{f_c} \times \frac{1}{f_l R} \tag{3.10}$$

where R is the radius of the smallest sphere that encloses the entire antenna. It is important to note that the expression has been simplified by replacing the constant vacuum phase velocity c in the wavelength to a value of 1. This is valid simplification as the FoM is not an absolute indication of performance, but a tool for comparison.

3.2.6 Prior Designs

We compare antennas in [65], [66], and [73] with the ideal specifications of the antenna element for the CWD project (Table 3.1). The antennas in [65] and [66] are small printed UWB cactus monopoles, while [73] is a large printed "fat" dipole with a "super wide" decade impedance and pattern bandwidth. Advantages of [65] and

[66] are that they are quite compact and fed with an unbalanced feed. Disadvantages of these antennas are that they do not exhibit sufficiently wide fractional bandwidth for the CWD project, and that they use unconventional Liquid Crystal Polymer (LCP) substrate (higher cost). The advantage of [73] is clearly the exceptional decade bandwidth performance. Disadvantages of [73] include significantly large size, the use of a specialized microwave substrate (i.e. higher cost), and the requirement of a balanced feed (i.e. requiring a decade bandwidth balun and increasing system complexity).

3.3 Design Methods

The main goal of the research was the enhancement of the well-matched impedance bandwidth of the antenna design. The specified impedance bandwidth constitutes a 10:1 ratio, which is exceptionally wide for a compact antenna. It was accepted that the optimization of the return loss would likely come at the expense of other antenna parameters.

To begin, the initial antenna design was simulated in order to characterize its performance with respect to the design specifications. This design was used as a point of reference. Then, a multitude of topological changes were tested using EM simulations in an attempt to enhance the impedance bandwidth. Each change was either accepted or discarded depending on its observed effect on the impedance matching. As this process progressed, an incremental design was formed which included multiple of the accepted changes. Eventually, the incremental design reached a stage where its performance gain was considered substantial with respect to the initial reference. At this point, the incremental design was taken as a “final design”. Then, the final design was characterized in the same way as the initial design and a second point of reference was established. The two points of reference were compared. Finally, both the initial and final designs were fabricated and measured in order verify the simulated results and to draw conclusions from the research.

3.3.1 Simulation Setup

The antenna was first modelled in ANSYS High Frequency Structure Simulator (HFSS). The simulation was set up in the following way. First, the solution type was configured. The solution type was set as a terminal network analysis ("DrivenTerminal" and "Network Analysis" options). This instructs the simulator to compute the antenna reflection coefficient in terms of scattered voltage and current at the port terminals with respect to some reference impedance Z_0, similar to a VNA [see 74, p. Technical Notes 31-147].

Second, the antenna excitation was prepared. A wave port was formed at the input of the SMA coaxial structure and was backed by a perfect electric conductor () cap as required by HFSS. The DrivenTerminal solution type was used. The coaxial shield was assigned as the reference terminal (akin to ground) and the center pin was assigned as the second terminal. This allowed for a port excitation based on voltage and current at the reference plane instead of scattered power of the EM modes. The terminal port characteristic impedance (Z_0) was validated numerically by the simulator to be very close to $50\,\Omega$.

Third, the adaptive meshing parameters were configured. The finite element method (FEM) mesh was generated using broadband adaptive meshing, where the simulator automatically chooses a number of in-band frequencies at which to refine the mesh. This is recommended for wideband designs in the HFSS documentation for increased reliability and accuracy of the results [see 75, p. Multi-Frequency Adaptive Meshing 1-5]. The maximum delta S was set to 0.02 or lower.

Next, a frequency sweep was created. The model is mainly excited with a frequency sweep from 0.3 to 6 GHz, with 96 frequency points.

Finally, the antenna open problem was modelled. The solution space must be made finite for the computational method, while also approximating free-space radiation conditions. This was accomplished by truncating the volume using perfectly matched layer (PML) regions created by the "Auto-Open" feature of HFSS. The padding between the PML and the antenna is determined based on the antenna operating frequency, which HFSS assumes to be the center frequency of the configured frequency sweep.

Note

An important distinction is made for the presentation of the final simulated results shown in this chapter. First, the open region was expanded semi-manually using the "Create Open Region" feature in HFSS with the operating frequency explicitly set as 0.3 GHz. The operating frequency was set to such a low value to ensure that the PML boundary did not impinge on the near-field of the antenna. This is important to reduce errors in the far-field results (i.e. negative radiation efficiency values). Second, multi-frequency meshing was used instead, with refinement at 0.3 GHz, 3.15 GHz and 6 GHz and a maximum delta S of 0.02. The meshing change was used to reduce the computation time, since expanding the open region increased the problem size (and computation time at the original settings) dramatically.

3.4 Antenna Design Progression

3.4.1 Initial Antenna Design

The initial antenna design for this research was developed by Dr. Natalia Nikolova and Alex Beaverstone and this version of the antenna has not been published in the literature. The design was given a code name of "design04sma", since it has an SMA feed. Here we explore the design04sma simulation model.

Simulation Model

The design04sma antenna is modelled in HFSS. The model consists of four parts:

1. A printed substrate
2. A metallized cavity
3. A shorting post
4. An SMA connector

The printed substrate (seen in Figure 3.2a and Figure 3.3) consists of a planar monopole-like antenna with a cactus-shaped radiator fed by tapered co-planar waveguide (CPW), a finite split ground plane, and a triangular hedge structure. The substrate itself is a 1.57 mm (62 mil) thick finite, homogeneous, isotropic dielectric region with $\epsilon_r = 4.4$ and $\tan\delta = 0.018$ to approximate FR-4. For the sake of simulation speed, all metal is modelled as PEC sheets, as this is a good enough approximation of the actual copper in the simulation-based design process.

The cavity consists of five rectangular PEC sheets which form a hollow box shape that is open at the top. The missing top face and its opposite have width and length equal to that of the printed substrate. The third dimension defines the depth of the cavity. One cavity wall contains a small cut-out to accommodate the feed SMA connector. A metallic shorting post electrically connects one part of the substrate metallization to the bottom of the cavity. This post is modelled as a PEC cylinder. The SMA connector is modelled using PEC and polytetrafluoroethylene (PTFE) regions ($\epsilon_r = 2.1$, $\tan\delta = 0.001$) and it is excited with a HFSS wave port so that it subsequently excites the CPW feed of the antenna. The cavity and shorting the post are seen in Figure 3.2b and Figure 3.2c. The length and width of the antenna substrate is 150 mm by 151 mm. The total antenna depth is 43.9 mm with the cavity included.

3.4.2 Final Design Revision

The final antenna design is shown in Figure 3.17. This design has been published [31] and can be referred to as the APS2019 design.

Simulation Model

The APS2019 antenna consists of a metallized FR-4 substrate and an SMA connector. The metallization pattern (Figure 3.4) appears similar to that of design04sma, however, important changes have been made to the CPW-based feed geometry and the ground plane. The dimensions of the substrate are increased to 150 mm by 180.6 mm. This design does not have any cavity backing, so the total depth is only 1.57 mm.

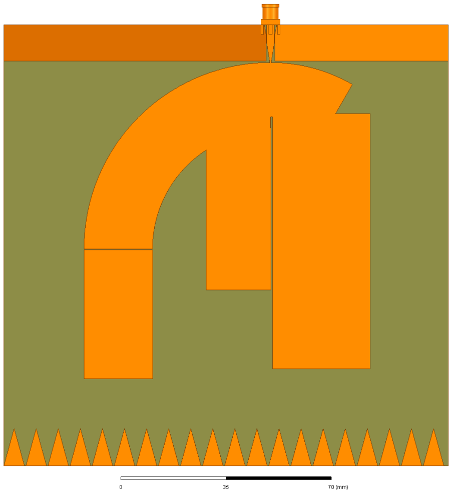

(a) Top view

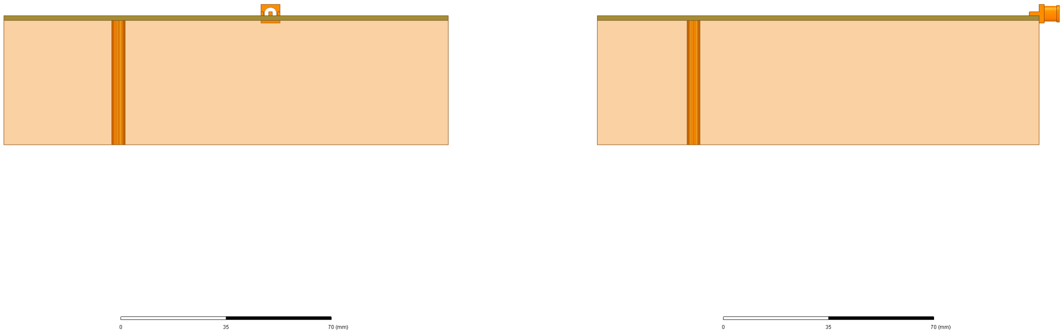

(b) Front view

(c) Right view

Figure 3.2: Views of the simulation model of the initial antenna design. The length and width of the antenna substrate is 150 mm by 151 mm and the total depth is 43.9 mm with the cavity included.

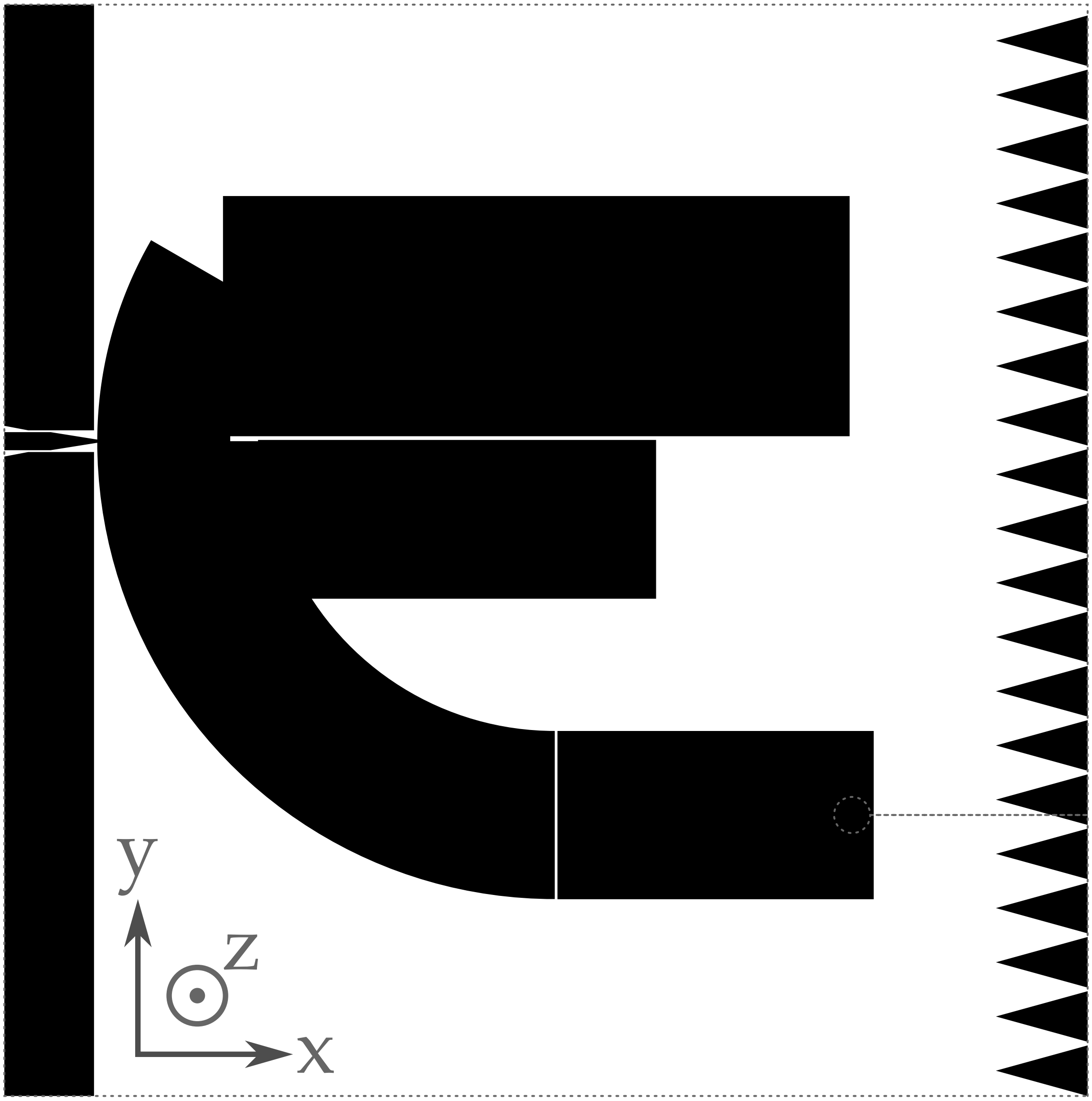

Figure 3.3: Actual size metallization pattern of the initial antenna design (design04sma). Solid black indicates presence of metallization, white indicates absence, and the dotted line indicates the substrate boundary.

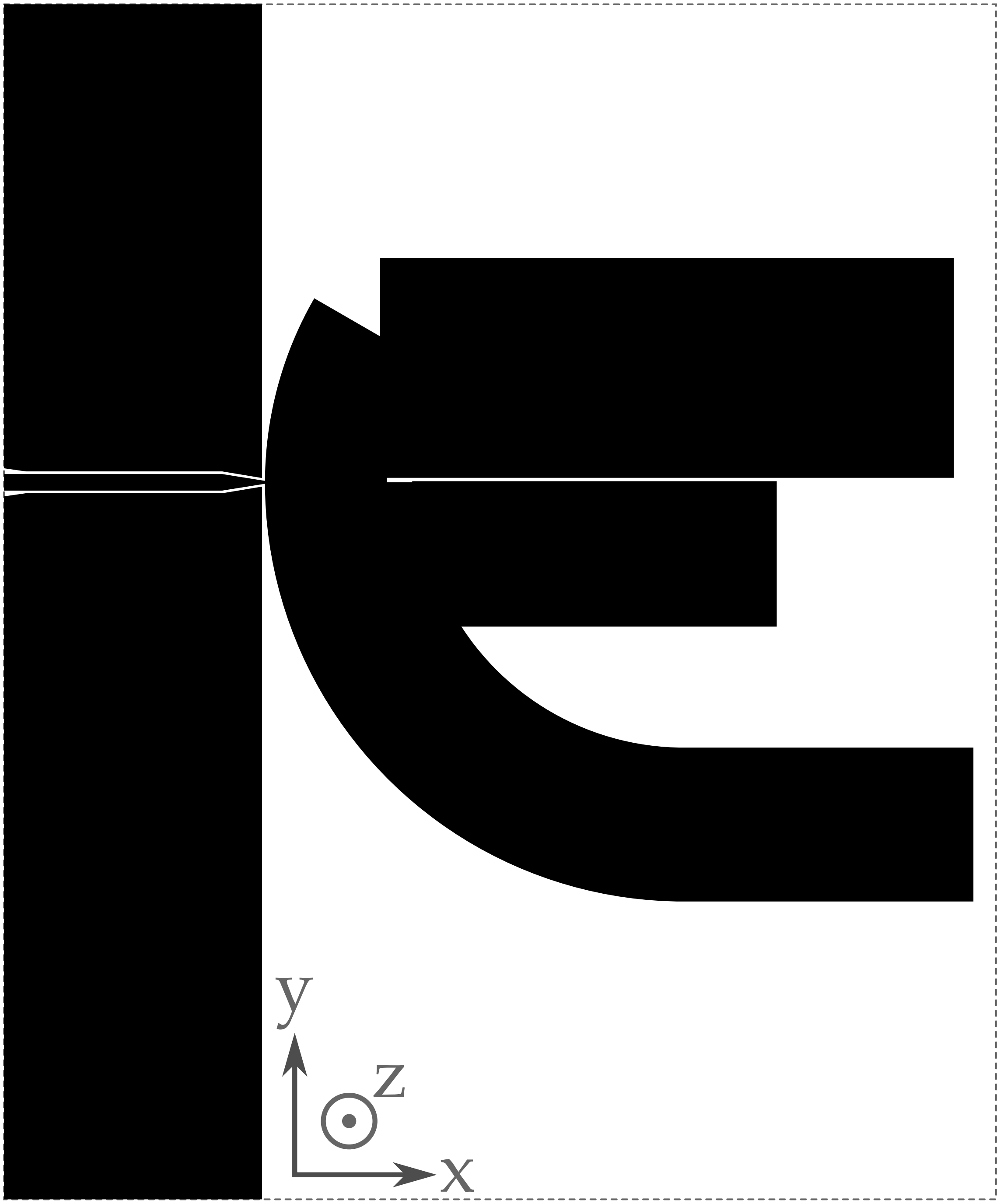

Figure 3.4: Actual size metallization pattern of the final antenna design. Solid black indicates presence of metallization, white indicates absence, and the dotted line indicates the substrate boundary.

3.4.3 Summary of Design Changes

A concise summary of the incremental changes from the initial to the final antenna design is as follows:

1. Initial antenna design (design04sma)
2. Removal of the triangular hedge (compare right side of Figure 3.3 and Figure 3.4) to reduce simulation complexity
3. Removal of the shorting post to reduce simulation and fabrication complexity
4. Modification of the feed CPW (see Figure 3.5) to improve impedance matching
5. Removal of the cavity altogether for the purposes of improving the "base antenna"
6. Expansion of the ground plane & substrate (again compare Figure 3.3 and Figure 3.4) to obtain improved matching at low frequencies
7. Removal of the slot between a rectangular patch and its closest cactus bend (Figure 3.3, bottom)
8. Final antenna design (APS2019)

A brief discussion of the reasoning behind these changes is given next.

First, the removal of the triangular hedge was performed for the purposes of reducing the simulation complexity. Reducing the simulation complexity means less physical features need to be solved for, leading to reduced simulation time. This was beneficial during the simulation-driven design process where many design changes were being tested.

(a) design04sma (b) APS2019

Figure 3.5: Comparison of the feed structures of the initial and final antennas. The scale is 2:1. The left side of each view is the antenna feedpoint while the right side is where the cactus-shaped radiator is connected. In the APS2019 design, the ground plane has been modified to follow the CPW taper as it meets the cactus such that the gap width remains fixed. The gap between the conductors has also been widened. These changes partly improved the broadband impedance matching.

Second, the removal of the shorting post was performed for similar purposes, as well as for the reduction of fabrication complexity. The shorting post is one of the more exotic features of the initial antenna, in that it entails a custom metallic rod that can somehow penetrate the antenna substrate and connect electrically to both the metallization of the substrate and of the bottom cavity wall. Such properties complicate the antenna fabrication (increasing eventual costs), so it was preferred to find an antenna design which does not require the post.

Third, the CPW feed was modified as shown in Figure 3.5 in order to improve the impedance matching. The modification consists mainly of the extension of the continuity of the CPW gap distance within the linear taper at the cactus end of the transmission line. It was thought that perhaps this would reduce impedance discontinuities, lowering the magnitude of reflections, and thus improving the impedance matching as seen through the reflection coefficient. The CPW gap as a whole was also slightly widened in an attempt to reduce reflection coefficient sensitivity of the design to fabrication tolerances, especially in the case of computer numerical control (CNC) mill-based fabrication wherein minimum gap size of the fabrication process was in reality slightly larger than the actual CPW gap size used in the initial antenna design due to the available tooling.

Fourth, the antenna cavity was removed altogether for the purposes of improving the base antenna which consists of merely a printed FR-4 substrate and a SMA connector. This change was related also to the reduction of simulation complexity to attain more rapid simulation time. The presence of the cavity backing significantly affects the antenna reflection coefficient, tending to increase the magnitude of reflections (and impedance mismatch) as it acts as a partial metallic wall in the antenna near-field. Thus, it was assumed that it would be a better approach to find a base antenna with the required impedance bandwidth at the desired size, then figure out a method to carefully re-introduce radiation-directing elements to the design.

Fifth, the ground plane and antenna substrate were both expanded for the purposes of improving the low-frequency impedance matching. It was determined by examining the real and imaginary parts of the antenna input impedance that the antenna did not radiate very well at the lower frequencies (low radiation resistance). This was assumed to be due, at least in part, to the antenna being insufficiently large at such frequencies to allow radiation to occur. In order for the antenna to be well-matched, the real part of the input impedance must be at least somewhat close to the $50\,\Omega$ system impedance, which is not possible when the radiation resistance is close to $0\,\Omega$. Therefore, the antenna ground plane was increased in both width and length, which also increased the width of the antenna substrate, in a successful attempt to increase this component of the input impedance.

Finally, the isolation slot between the rectangular patch (which used to be connected to the shorting post) and the long annular bend of the antenna was removed. This was done for testing purposes to observe whether such slot notably impacts the performance of the base antenna. It was determined that the removal of the slot did not degrade the performance so it was kept as an additional design simplification.

3.5 Simulated Performance

Here, the simulated impedance matching and radiation characteristics of the initial and final antennas are presented.

3.5.1 Simulated Impedance Matching

The simulated reflection coefficient magnitude (Γ) (in dB) and the reflection efficiency (e_r) are shown in Figure 3.6 and Figure 3.7. The impedance bandwidth, its associated frequency ratio, and the impedance-matched band coverage of the APS2019 antenna is significantly improved compared to design04sma. The simulated reflection efficiency (Figure 3.7) is also generally increased for the APS2019 design, which illustrates the effect of the improved impedance matching on the power transfer to the antenna.

3.5.2 Simulated Radiation Properties

For UWB antennas, radiation properties are a complicated topic. All antenna patterns are functions of frequency, which simply cannot be ignored over the large bandwidth of a UWB antenna. A gain pattern, for example, is generally a strong

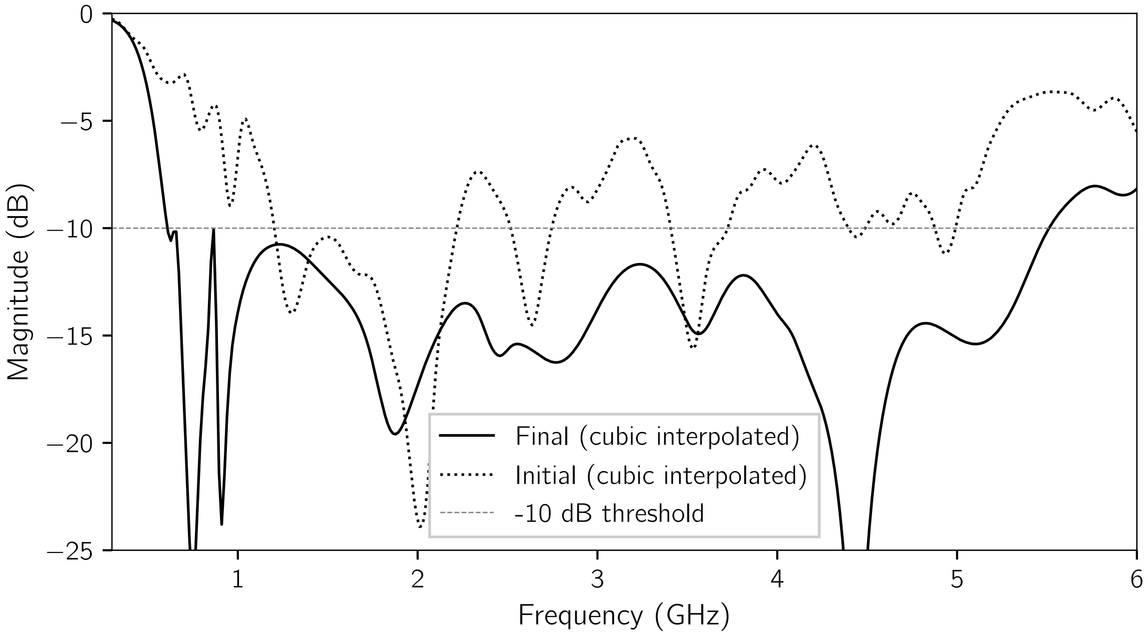

Figure 3.6: Simulated reflection coefficient of the initial (design04sma) and final (APS2019) antennas. For design04sma, the matched band coverage is 39.3% with a maximum absolute impedance bandwidth of 1.01 GHz from 1.20 GHz to 2.2 GHz (1.83:1). For APS2019, the matched band coverage is 97.6% with a maximum absolute impedance bandwidth of 4.9 GHz from 0.61 GHz to 5.51 GHz (9.03:1).

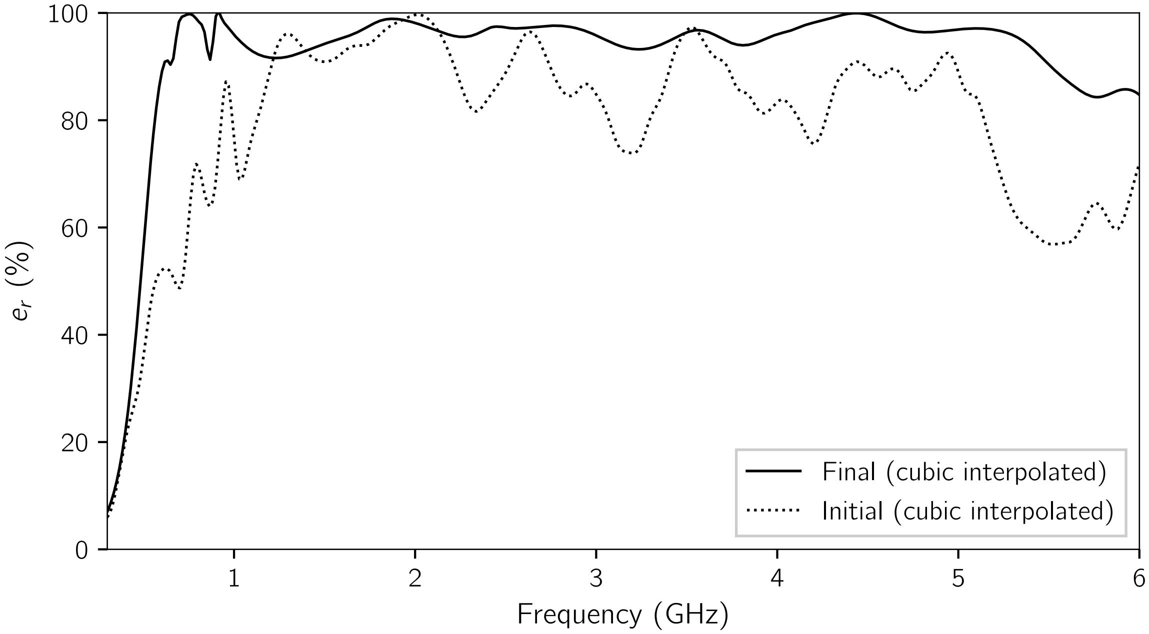

Figure 3.7: Simulated reflection efficiency of the initial (design04sma) and final (APS2019) antennas.

function of direction and frequency, making it difficult to describe concisely. Even when plots are restricted to a handful of principal plane cuts, it is impossible to convey the complete picture. The antenna polarization is similarly convoluted. The only relatively straightforward radiation parameter is the radiation efficiency, which is a simple 1D function of frequency. Here, the gain, polarization, and radiation efficiency of both antenna designs are described with as many details as possible.

Gain

Samples of the antenna gain pattern are provided at frequencies of 0.5 GHz, 2.75 GHz, and 5 GHz for both the initial (Figure 3.8, Figure 3.9, Figure 3.10) and final (Figure 3.11, Figure 3.12, Figure 3.13) designs. The gain patterns of both antennas are complicated. We define the reference boresight direction as perpendicular to the antenna substrate, which is defined by the angles $\theta = 0°, \phi = 0°$. Upon examination it is evident that the direction of peak gain is not always around the reference boresight. Additionally, many lobes and nulls in the pattern form, disappear, and shift around as the frequency changes. For these reasons, it is not useful to evaluate antenna beam parameters such as beamwidths.

Some elevation plane cuts of the design04sma antenna gain (Figure 3.9c, Figure 3.10c) are asymmetrical and indicate stronger radiation (by roughly 6 dB) within the forward-looking half-space ($0° \leq \theta \leq 90°$, $270° \leq \theta \leq 360°$) compared to that within the backward-looking half-space. In contrast, the corresponding plane cuts of the APS2019 design (Figure 3.12c, Figure 3.13c) appear nearly symmetrical and comparatively omnidirectional. These differences are expected, with the cavity backing of the design04sma apparently functioning as intended and suppressing back radiation.

Polarization

The reference boresight axial ratio (Figure 3.14) is a partial indication of the antenna polarization in the forward direction. A value close to 1 (0 dB) indicates circular polarization, while a large value (> 10 dB) indicates near-linear polarization. An intermediate value indicates elliptical polarization.

Radiation Efficiency

The simulated radiation efficiency is shown in Figure 3.15. We see that both antennas exhibit radiation efficiency above 80% for most of the band, with design04sma being slightly less efficient below 1 GHz. This is an excellent result since the antennas are fabricated using FR-4 laminate, which is low-cost but quite lossy at microwave

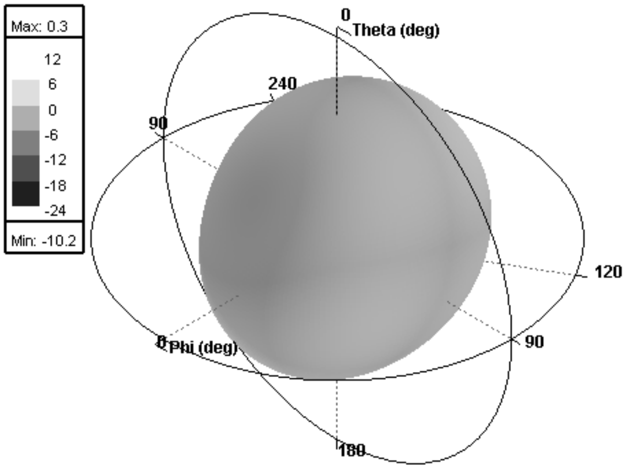

(a) 3D Pattern

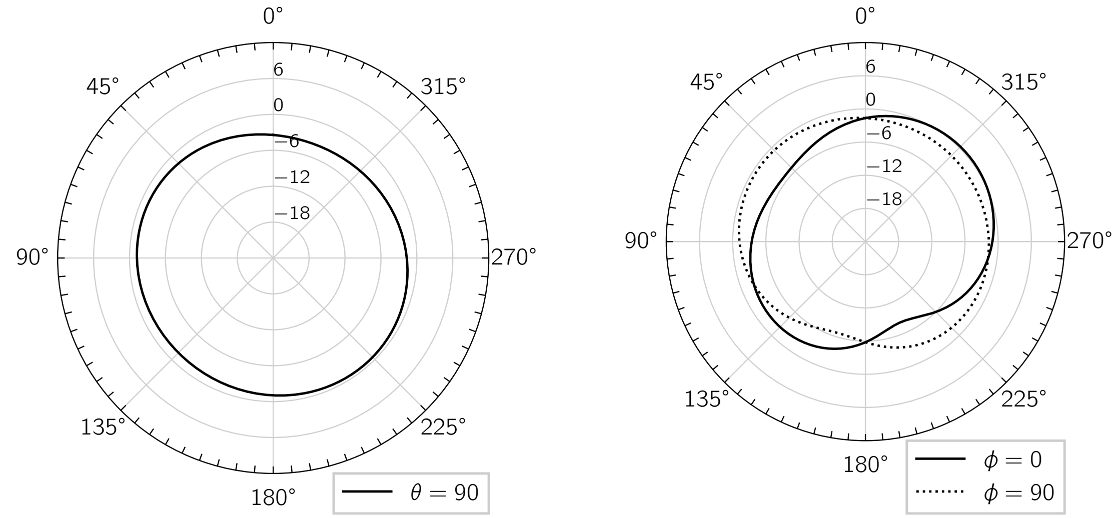

(b) Azimuth Plane (c) Elevation Planes

Figure 3.8: Gain (dBi) of the initial antenna (design04sma) at 0.5 GHz.

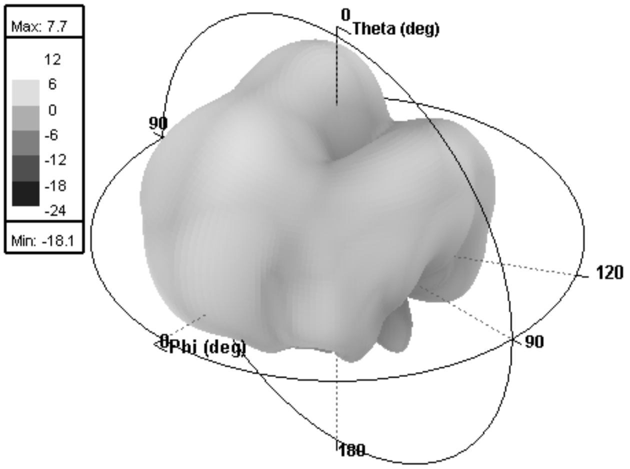

(a) 3D Pattern

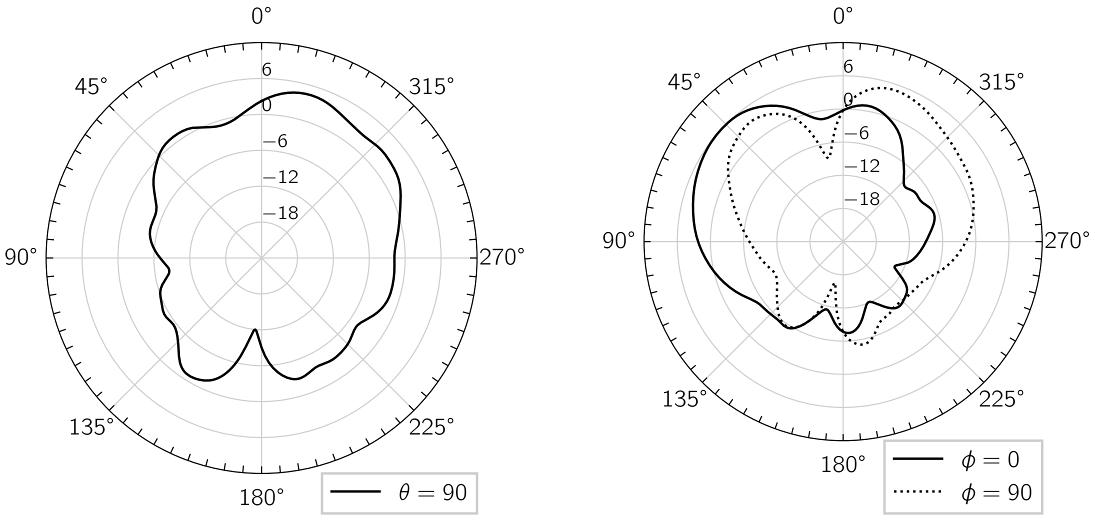

(b) Azimuth Plane (c) Elevation Planes

Figure 3.9: Gain (dBi) of the initial antenna (design04sma) at 2.75 GHz.

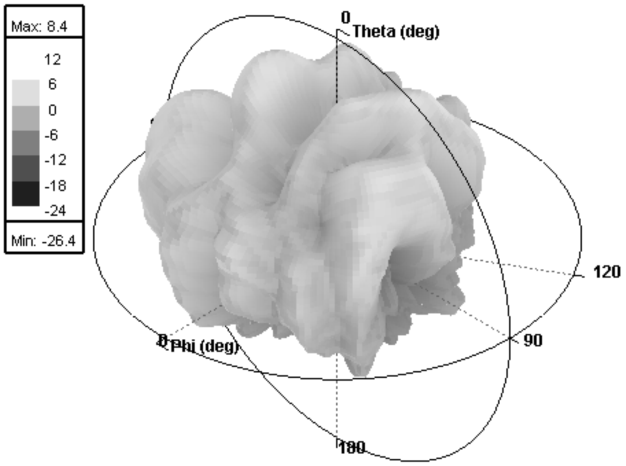

(a) 3D Pattern

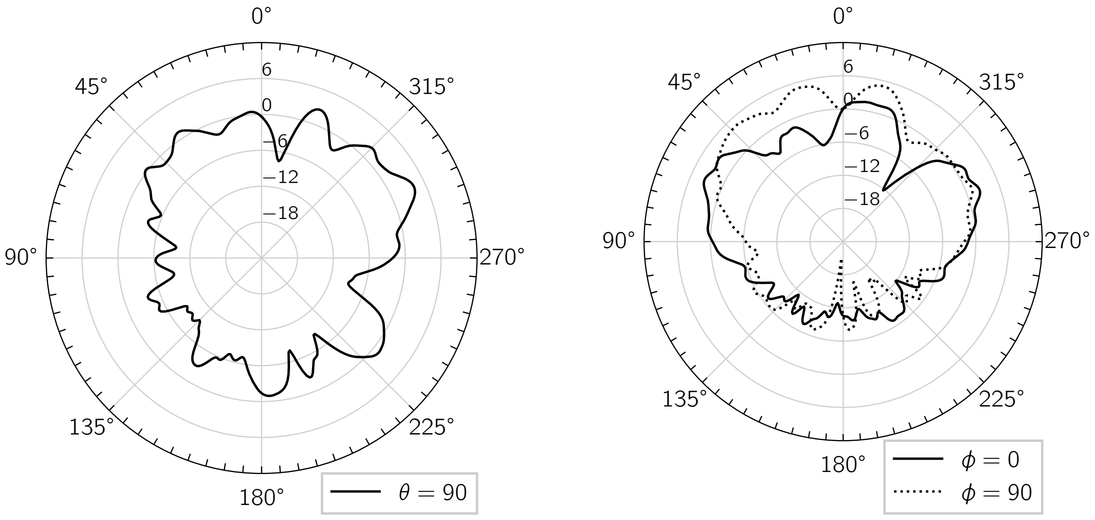

(b) Azimuth Plane (c) Elevation Planes

Figure 3.10: Gain (dBi) of the initial antenna (design04sma) at 5 GHz.

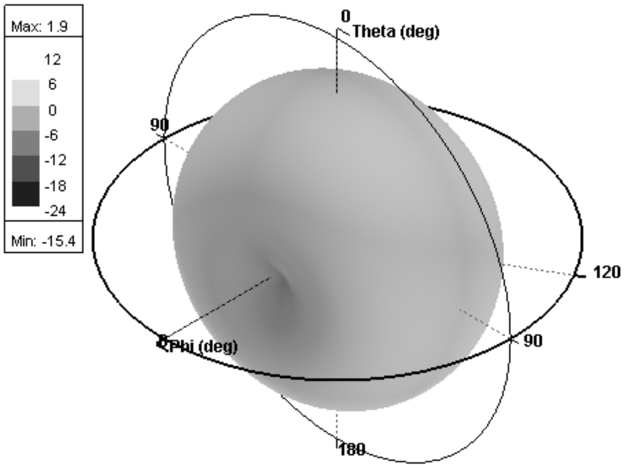

(a) 3D Pattern

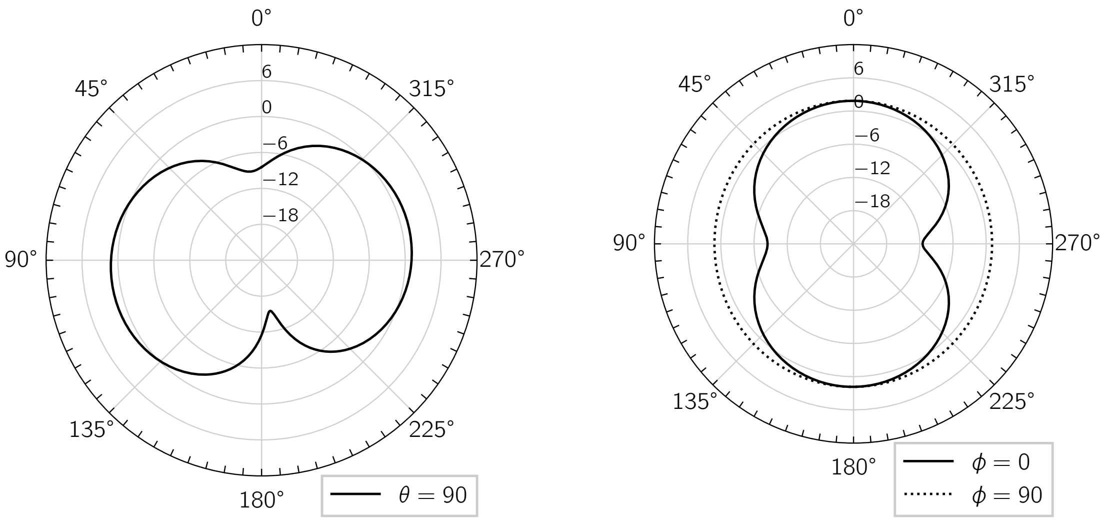

(b) Azimuth Plane

(c) Elevation Planes

Figure 3.11: Gain (dBi) of the final antenna (APS2019) at 0.5 GHz.

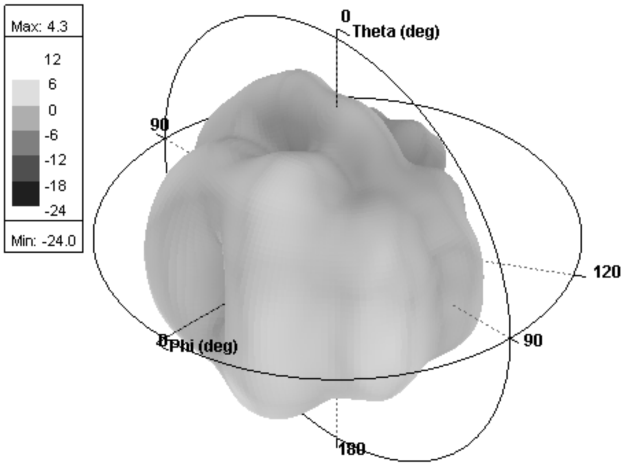

(a) 3D Pattern

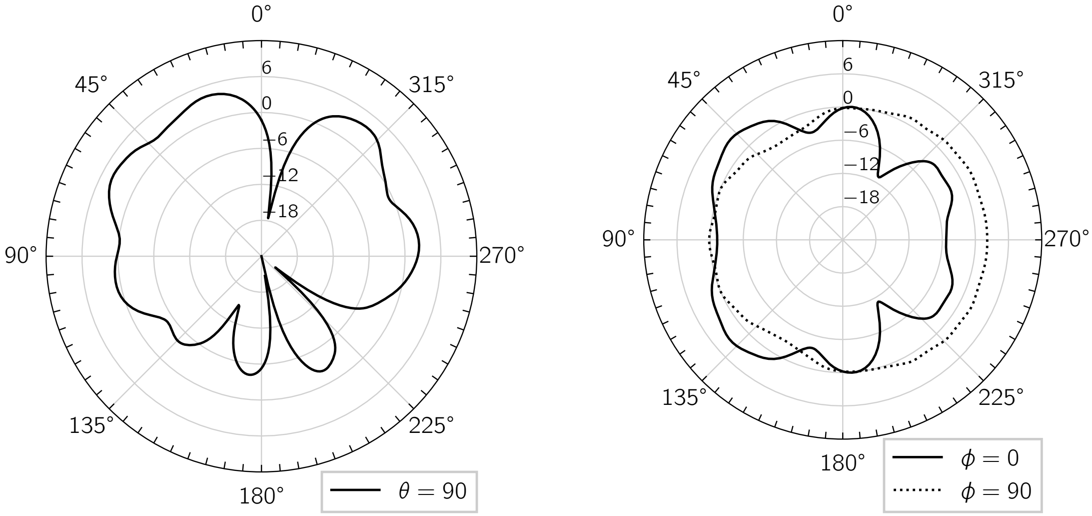

(b) Azimuth Plane (c) Elevation Planes

Figure 3.12: Gain (dBi) of the final antenna (APS2019) at 2.75 GHz.

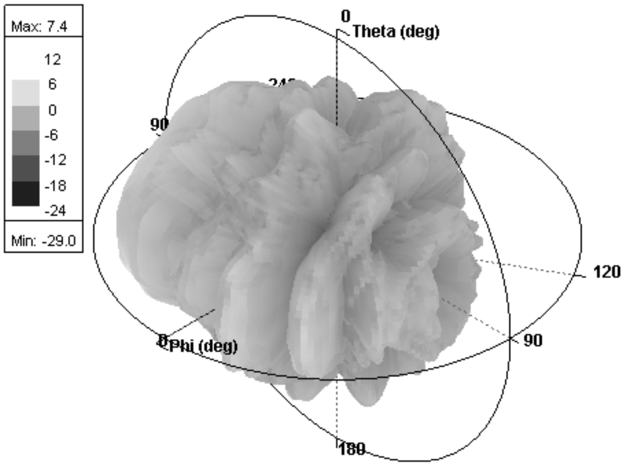

(a) 3D Pattern

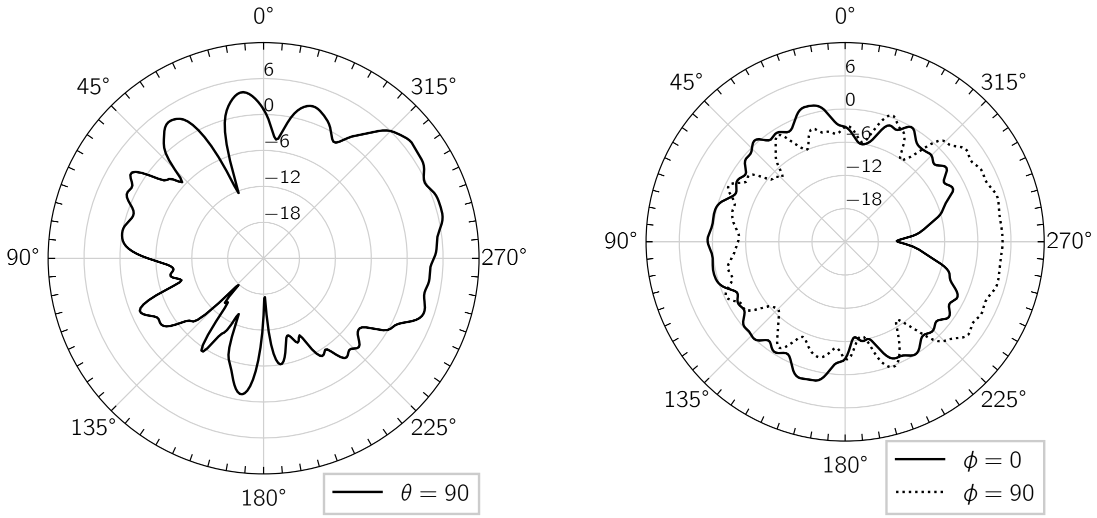

(b) Azimuth Plane (c) Elevation Planes

Figure 3.13: Gain (dBi) of the final antenna (APS2019) at 5 GHz.

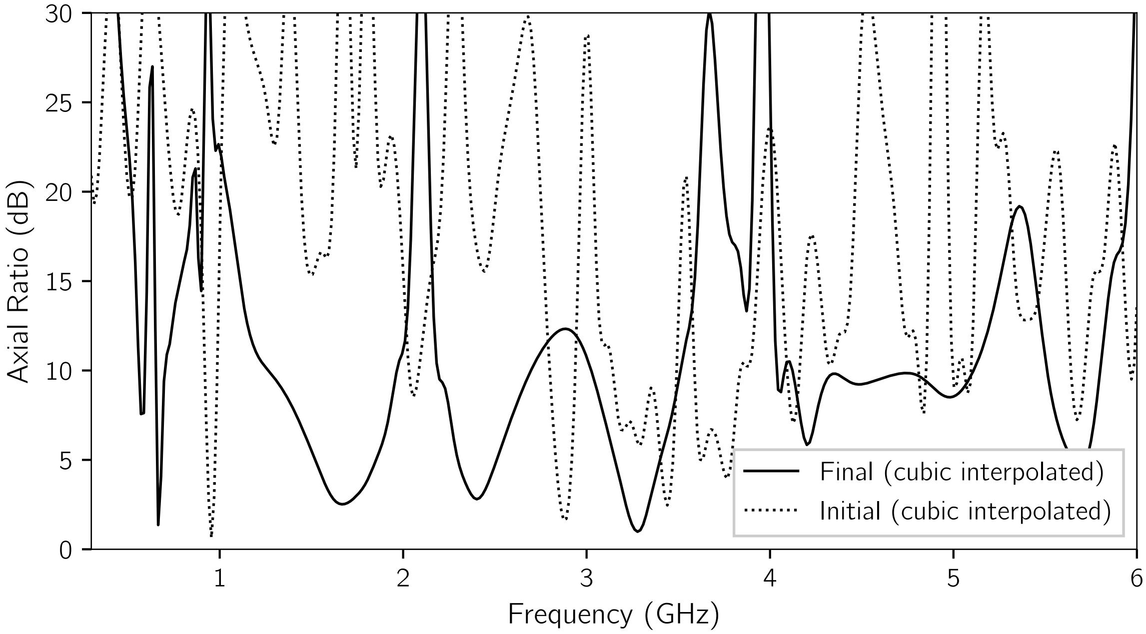

Figure 3.14: Reference boresight axial ratio of the initial and final antennas.

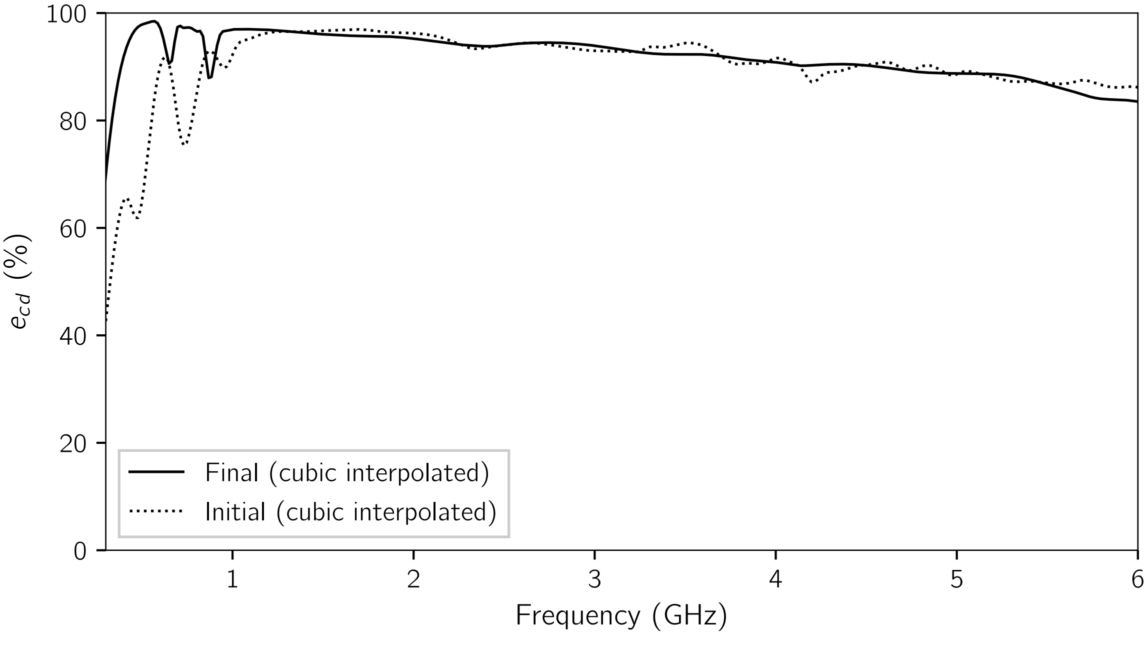

Figure 3.15: Radiation efficiency of the initial (design04sma) and final (APS2019) antennas.

frequencies. One should note that conduction losses are not included in these results since PEC was used in the simulation. Nevertheless, it is a fair assumption that the FR-4 dielectric loss is the dominant loss component since copper is a very good conductor.

3.6 Fabrication and Measured Performance

The design04sma and APS2019 designs were fabricated and subsequently measured for comparison with the simulated results. Each design was fabricated in a different way, so the process is detailed for each design separately. Afterward, the setup that was used for measuring the reflection coefficient of the prototypes is detailed. Finally, the reflection coefficient measurements of the designs are presented.

3.6.1 Fabrication of Initial Design

First, the design04sma antenna was fabricated. This design is much less trivial to fabricate than a regular printed antenna due to the cavity and the shorting post. In realizing the design, all idealized media were replaced with actual materials:

- The printed substrate: FR-4 of 1.6 mm 62 mil thickness and 35.6 µm (1.4 mil) copper lamination
- The metallized cavity: implemented with the same FR-4 laminate as the printed substrate, with copper on one side
- The shorting post: implemented as a bolt and a hexagonal nut made from galvanized steel (zinc plated) to allow adjustment of cavity depth

- The SMA connector: a PCB edge mount SMA connector[1]

Geometrical differences between the simulation model and the fabricated prototype arose during fabrication. One difference is the presence of additional FR-4 regions forming the cavity. This additional FR-4 is located outside of the cavity to minimize its impact on the near-field of the antenna. Another difference is that the effective cavity depth was made adjustable by using the shorting post and threaded nut.

The FR-4 pieces were shaped with the use of a CNC mill. This included the milling of the metallized copper pattern on the printed substrate. One complete antenna requires six rectangular pieces of FR-4 material to be cut out. One of these pieces is the printed substrate. Four of these pieces are the side walls of the cavity. The last of these pieces is the bottom wall of the cavity, cut with a precise hexagonal hole to accommodate a hex nut.

The antenna was constructed as follows. First, the four cavity walls were soldered at the corners to form a box with two missing sides. Next, the printed substrate was inserted at the top of the box, whose ground plane and triangular hedge were then electrically connected to the cavity metallization with solder. Finally, a hexagonal nut was placed into an appropriately milled hexagonal hole in the bottom of the cavity and soldered in place. A bolt was fed through the printed substrate to be screwed into the nut. Photographs of a fabricated prototype are shown in Figure 3.16.

3.6.2 Fabrication of Final Design

The APS2019 antenna was comparatively straightforward to fabricate. Instead of milling the antenna substrate in the lab, this design was professionally manufactured

---

[1] Cinch Connectivity Solutions P/N 142-0711-821 https://www.belfuse.com/product/part-details?partn=142-0711-821

(a) Perspective

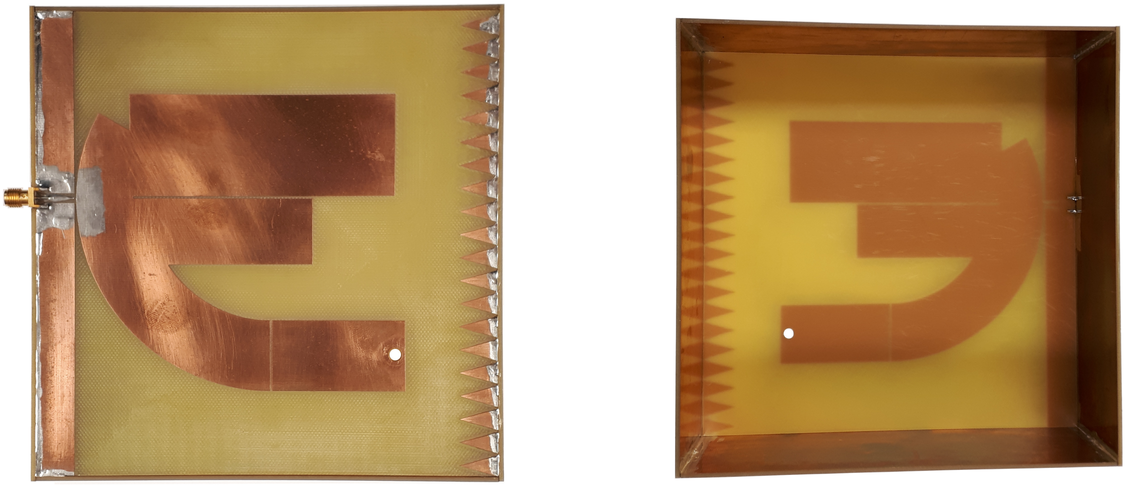

(b) Top

(c) Bottom

Figure 3.16: Images of a fabricated prototype of the initial (design04sma) antenna design.

by ALLPCB[2]. The only manual task involved in the fabrication was the soldering of a SMA connector to the feed of each PCB. Six samples of this design were produced by the manufacturer. Top and bottom photographs of one sample are shown in Figure 3.17.

3.6.3 Measurement Setup

The antenna measurement setup (Figure 3.18) consisted of a VNA, a coaxial cable, a semi-vacant lab room, a makeshift antenna stand, and the fabricated antenna prototypes. The reflection coefficient of the antenna was measured using a VNA which was short-open-load (SOL) calibrated using an HP 85052D 3.5mm calibration kit. With this setup, the antenna reflection coefficient was approximately measured. The effect of the room on the reflection coefficient measurement was reduced by ensuring the antenna was placed far away from metals and other objects with high permittivity that would interfere with the antenna near-field. To reduce the effect of the antenna stand, Styrofoam was used. Styrofoam is mostly air by volume percentage so it has an effective ϵ_r very close to that of air. This means that the antenna stand likely had only a small effect on the measured antenna return loss.

3.6.4 Impedance Matching Measurements

The reflection coefficient measurements of the fabricated prototypes are shown in Figure 3.19 for the initial design and Figure 3.20 for the final design. The measured reflection coefficient of both designs is also compared simultaneously in Figure 3.21.

---

[2] https://www.allpcb.com/

(a) Top

(b) Bottom

Figure 3.17: Images of a fabricated prototype of the initial (APS2019) antenna design.

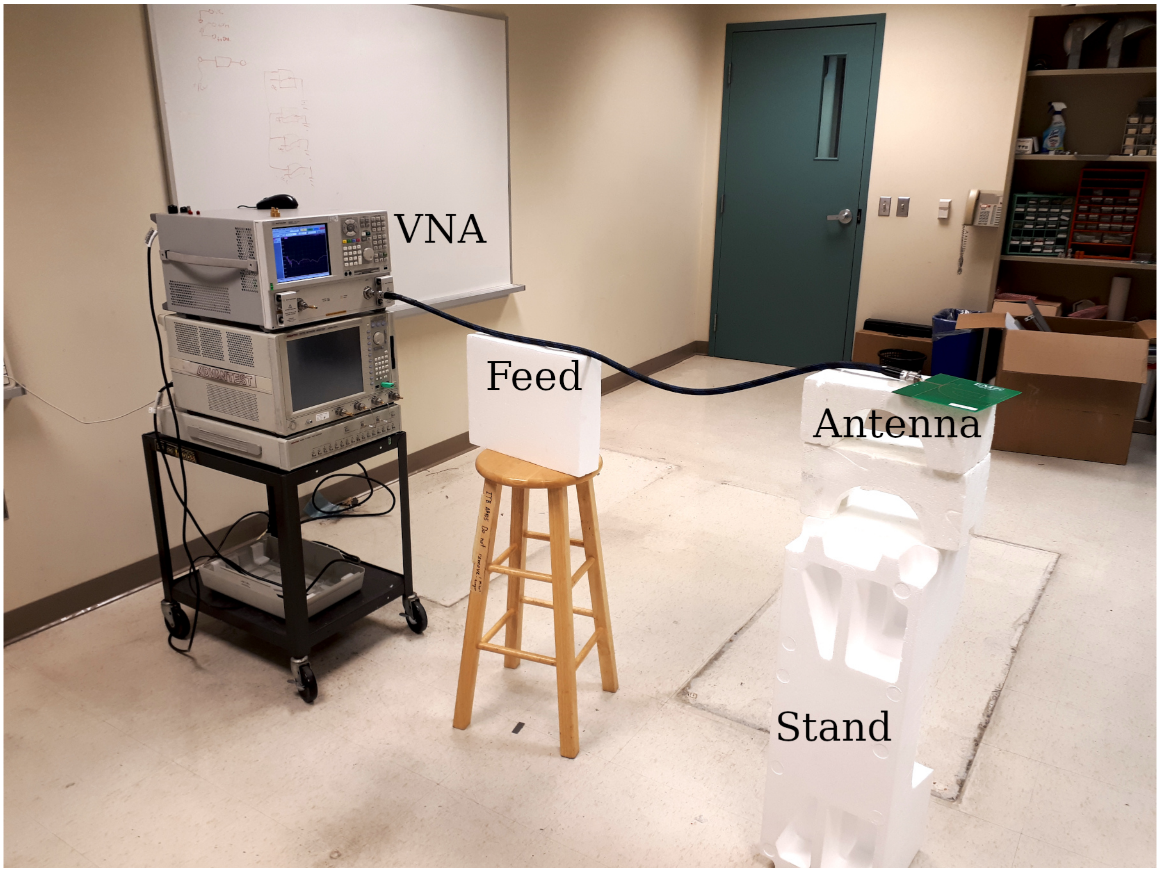

Figure 3.18: Measuring the antenna reflection coefficient in a semi-vacant lab room.

TABLE 3.2: THE VNA SETUP FOR MEASURING REFLECTION COEFFICIENT.

Option	Value
IF Bandwidth	10 kHz
Averaging	10
Start Frequency	15 MHz
Stop Frequency	12 GHz
Number of Frequency Points	1599
Frequency Spacing	7.5 MHz
Error Correction	Full 1-Port SOL Correction (HP 85052D)

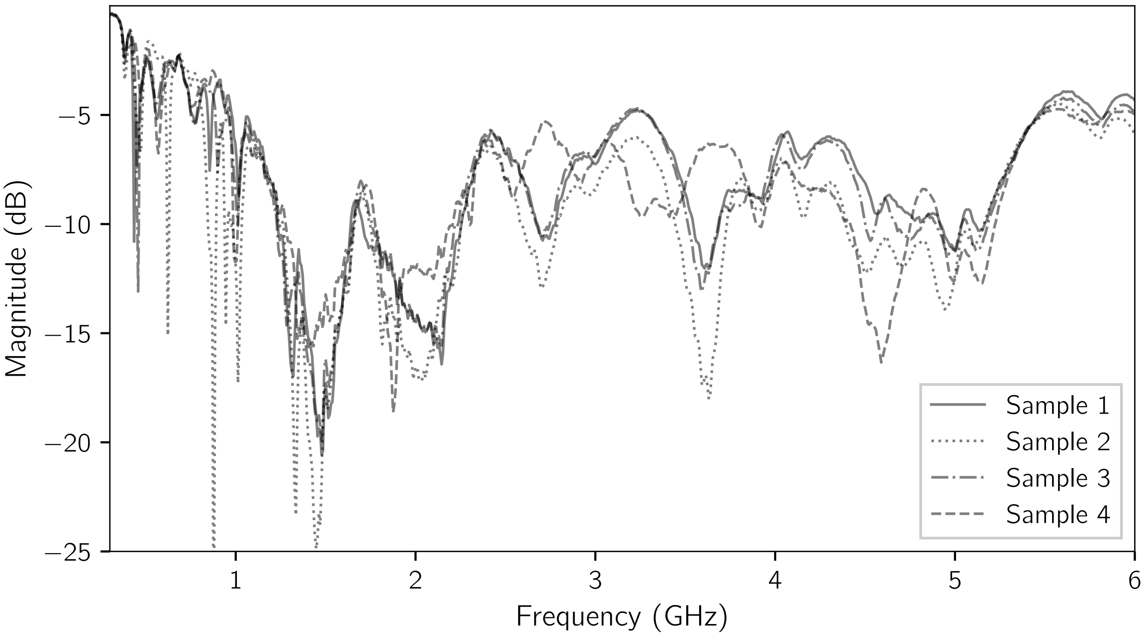

(a) All measured prototypes

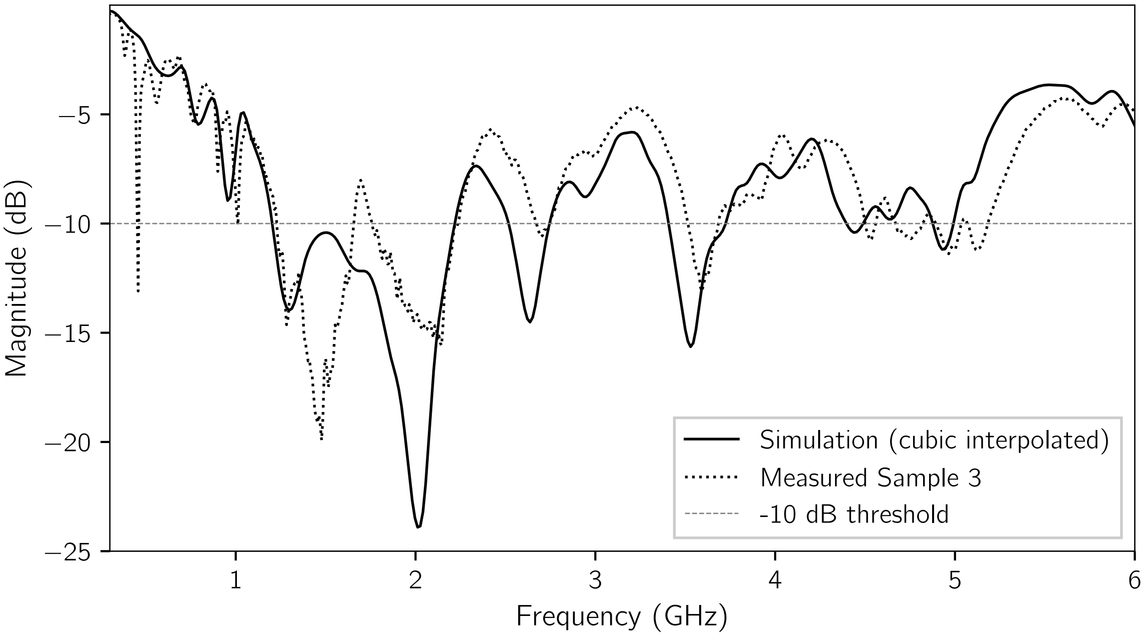

(b) Simulation versus a single prototype

Figure 3.19: Comparison of measured and simulated reflection coefficient magnitude of the initial antenna design.

The four fabricated prototypes of the initial design have similar, but not identical, impedance matching performance (Figure 3.19a). Performance variation between simulation and measurement and also between the individual prototypes is not unexpected, since fabrication was performed manually.

The six fabricated prototypes of the final design exhibit tighter impedance matching performance (Figure 3.20a) variation. Prototype 6 deviates in performance due to fabrication with a slightly different SMA connector. It turns out that the performance of prototype 6 is more similar to the simulation than any of the other prototypes so it is used for comparison later.

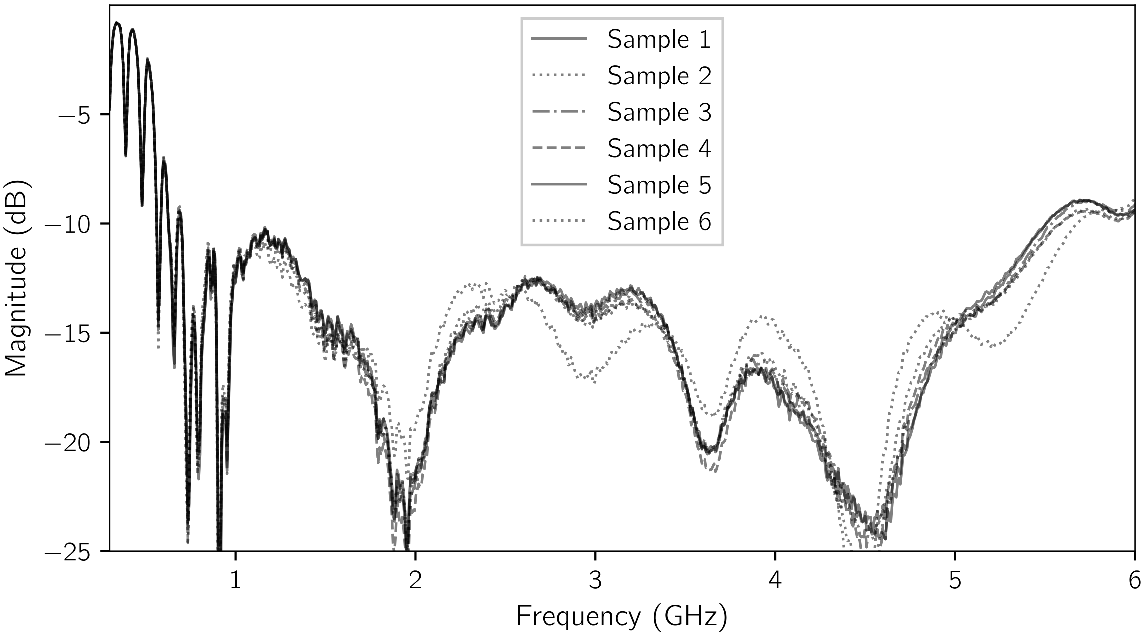

(a) All measured prototypes

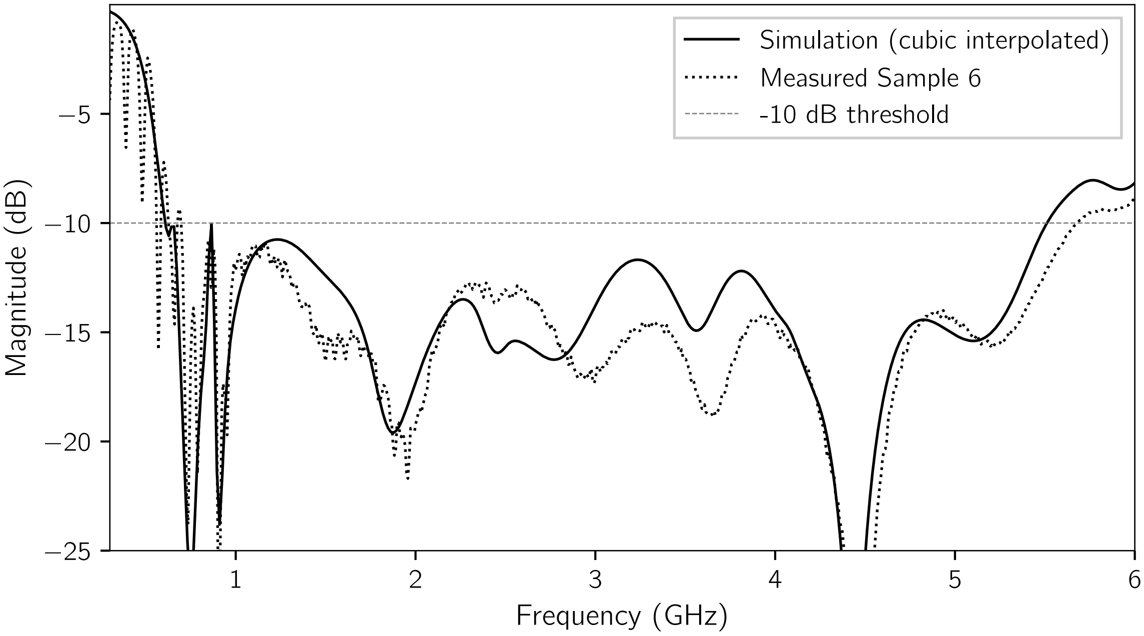

(b) Simulation versus a single prototype

Figure 3.20: Comparison of measured and simulated reflection coefficient magnitude of the final antenna design.

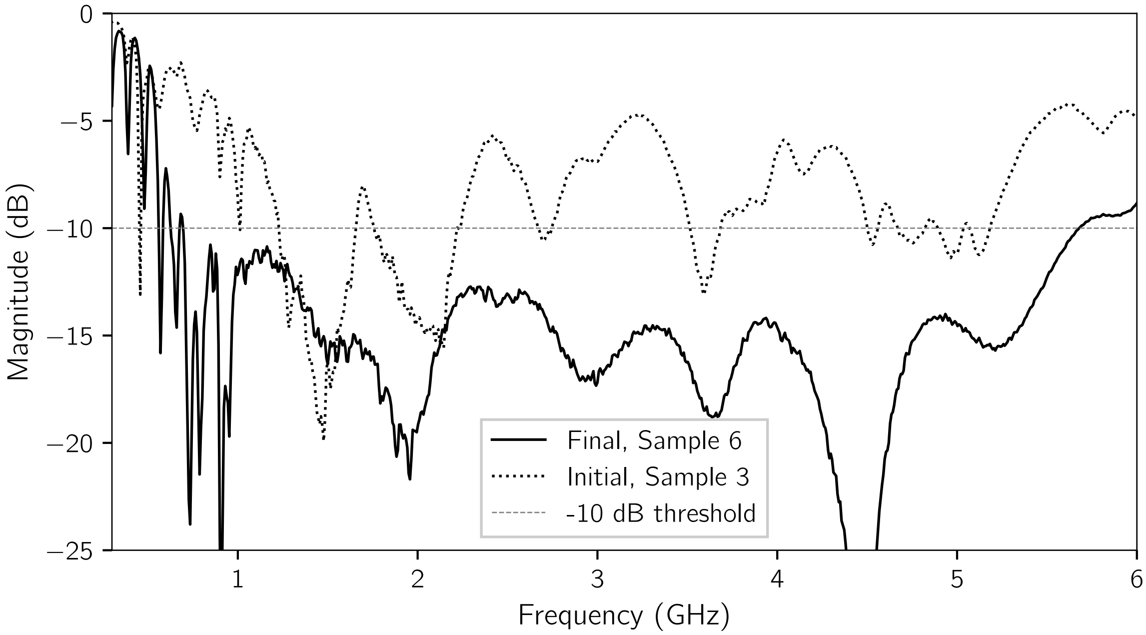

Figure 3.21: Measured reflection coefficient of the initial (design04sma) and final (APS2019) antennas. For design04sma, the matched band coverage is 32.5% with a maximum continuous impedance bandwidth of 0.46 GHz from 1.76 GHz to 2.2 GHz (1.26:1). For APS2019, the matched band coverage is 97.3% with a maximum continuous impedance bandwidth of 4.98 GHz from 0.7 GHz to 5.68 GHz (8.1:1).

3.7 Summary of Impedance Matching Results

The quantitative impedance matching results from section 3.5 and section 3.6 are summarized in Table 3.3 for convenience. Additionally, Table 3.4 compares the measured performance of the initial and final designs with the design specifications, and evaluates the FoM.

In terms of the measured impedance performance, the APS2019 design appears to be much improved over design04sma. When comparing prototype 3 of design04sma to prototype 6 of APS2019, the following changes are observed:

- The maximum absolute impedance bandwidth increased 983% from 0.46 GHz to 4.98 GHz.
- The associated frequency ratio increased 543% from 1.26:1 to 8.1:1.
- The impedance-matched band coverage of the 0.5 GHz to 5 GHz band increased nearly 200% from 32.5% to 97.3%.

Thus, the impedance performance of the final design appears to be significantly improved compared to the impedance performance of the initial design. Similar increases are seen in the simulated performance, where both designs perform slightly better than their measured prototypes.

Table 3.3: Impedance matching performance of initial (design04sma), final (APS2019), and ideal antennas.

(a) Initial design

Quantity	Ideal	Simulation	Measurement
f_l (GHz)	0.5	1.20	1.76
f_u (GHz)	5	2.22	2.22
Impedance bandwidth (GHz)	4.5	1.02	0.46
Frequency ratio	10:1	1.84:1	1.26:1
Band coverage (%)	100	39.3	32.5

(b) Final design

Quantity	Ideal	Simulation	Measurement
f_l (GHz)	0.5	0.61	0.7
f_u (GHz)	5	5.51	5.68
Impedance bandwidth (GHz)	4.5	4.90	4.98
Frequency ratio	10:1	9.03:1	8.1:1
Band coverage (%)	100	97.6	97.3

Table 3.4: Comparison of initial and final antennas measured performance to design specifications

Design	f_l (GHz)	f_u (GHz)	b_{fr}	Area (cm^2)	R (cm)	Substrate Material	ϵ_r	FoM
Initial	1.2	2.22	0.596	226	10.9	FR-4	4.4	4.56
Final	0.7	5.68	1.56	271	12.8	FR-4	4.4	17.42
Ideal	0.5	5	1.636	225	11.3	FR-4	4.4	28.96

3.8 Conclusions and Future Work

In this chapter we have examined the empirical investigation of an antenna design with respect to a particular application. The author has applied a handful of physical changes to this antenna with the goal of improving the impedance matching performance. The original impedance matching goal was to achieve $-10\,\mathrm{dB}$ reflection coefficient over the $0.5\,\mathrm{GHz}$ to $5\,\mathrm{GHz}$ band in a $50\,\Omega$ system. Changes pertaining to the feed geometry, the removal of the antenna cavity, and the resizing of the antenna ground plane and substrate have contributed to modified impedance matching and radiation performance. The difference in impedance matching performance is demonstrated through simulation and measurement of multiple fabricated prototypes of initial and final designs.

The apparent changes in the final design versus the initial design are as follows:

- Improvements
    1. Figure of merit (FoM): from 4.56 to 17.42 (282% increase)
    2. Adequate impedance matching: from 32.5% to 97.3% of the operating band
    3. The impedance matching FoM (fractional impedance bandwidth): from 0.231 to 1.561 (576% increase)
    4. Maximum absolute impedance bandwidth: from $0.46\,\mathrm{GHz}$ to $4.98\,\mathrm{GHz}$ (983% increase)
- Degradations
    - Substrate area: from $227\,\mathrm{cm}^2$ to $271\,\mathrm{cm}^2$ (19.4% increase)

  - Suppression of back radiation has degraded by roughly 6 dB across the band

The improvements in the final design have allowed it to exhibit comparable FoM to the designs in [65] and [73] (see Table 3.1 and Table 3.4). The final design is still not as compact as [66] or the specified ideal as can also be seen by examining the FoM.

The demonstrated impedance performance gains have come at the expense of the antenna radiation characteristics. We have seen that the original antenna exhibits better forward-looking characteristics due to the cavity backing, whereas the final antenna has more of an omnidirectional pattern which spreads radiated energy more evenly. The original antenna is also 16.7% smaller in width than the final antenna and has a more desirable square-shaped profile. Thus, with respect to the design specifications, the initial antenna has better size and radiation properties, while the final antenna wins with respect to impedance matching.

Future succession of this research should focus on improving the antenna radiation characteristics while preserving superior impedance matching. This likely involves a re-introduction of the cavity backing to the APS2019 design with careful shape optimization. This will be a challenging design task. In the current body of work, none of the presented far-field quantities have yet been verified through measurement. Thus, additional work which focuses on the radiation characteristics should include actual measurements of the gain patterns and the polarization in order to verify the simulated results.

References in Chapter 3

[31] E. A. Eveleigh, A. S. Beaverstone, and N. K. Nikolova, "Printed cactus monopole antenna with enhanced impedance bandwidth," in *2019 IEEE International Symposium on Antennas and Propagation and USNC-URSI Radio Science Meeting*, IEEE, 2019, pp. 1085–1086 (cit. on pp. 13, 89).

[32] Industry Canada, "Radio standards specification RSS-220, issue 1, devices using ultra-wideband (UWB) technology," Jul. 2018. [Online]. Available: https://www.ic.gc.ca/eic/site/smt-gst.nsf/eng/sf09347.html (cit. on pp. 21, 78).

[33] United States of America, "Title 47 CFR part 15, subpart F–ultra-wideband operation, §15.503," May 2002. [Online]. Available: https://www.ecfr.gov/cgi-bin/text-idx?node=pt47.1.15#sp47.1.15.f (cit. on pp. 21, 78).

[34] "UWB regulations, A summary of worldwide telecommunications regulations governing the use of ultra-wideband radio," Application Note: APR001, English, version 1.2, 2015. [Online]. Available: https://www.decawave.com/sites/default/files/apr001_uwb_worldwide_regulations_summaryrev1.2.pdf (cit. on pp. 21, 78).

[36] H. Schantz, *The Art and Science of Ultrawideband Antennas*, 1st ed., ser. Artech House Antennas and Propagation Library. 685 Canton Street Norwood, MA 02062: Artech House, 2005 (cit. on pp. 21, 22, 23, 33, 70, 71, 72, 73, 74, 75, 76).

[38] J. Sachs, *Handbook of Ultra-Wideband Short-Range Sensing: Theory, Sensors, Applications*, 1st ed. Boschstr. 12, 69469 Weinheim, Germany: Wiley-VCH, 2012 (cit. on pp. 22, 28, 33, 75, 76, 79).

[39] T. Zwick, W. Wiesbeck, J. Timmermann, and G. Adamiuk, Eds., *Ultra-wideband RF System Engineering*, 1st ed., ser. EuMA High Frequency Technologies Series. Cambridge CB2 8BS, United Kingdom: Cambridge University Press, 2013 (cit. on pp. 22, 28, 29, 79).

[62] V. Zachou, C. G. Christodoulou, M. T. Chryssomallis, D. Anagnostou, and S. Barbin, "Planar monopole antenna with attached sleeves," *IEEE Antennas and Wireless Propagation Letters*, vol. 5, pp. 286–289, 2006, ISSN: 1536-1225. DOI: 10.1109/LAWP.2006.876970 (cit. on p. 68).

[63] V. Zachou, C. G. Christodoulou, M. T. Chryssomallis, and D. Anagnostou, "Reconfigurable printed cactus antenna," in *2006 IEEE Antennas and Propagation Society International Symposium*, Jul. 2006, pp. 201–204. DOI: 10.1109/APS.2006.1710489 (cit. on p. 68).

[64] C. Saephan, H. Khaleel, B. Valdovinos, A. Isaac, and A. Bihnam, "Tri-band cactus shaped printed monopole," in *2014 IEEE Antennas and Propagation Society International Symposium (APSURSI)*, Jul. 2014, pp. 1704–1705. DOI: 10.1109/APS.2014.6905178 (cit. on p. 68).

[65] S. Nikolaou, G. E. Ponchak, M. M. Tentzeris, and J. Papapolymerou, "Compact cactus-shaped ultra wide-band (UWB) monopole on organic substrate," in *2007 IEEE Antennas and Propagation Society International Symposium*, IEEE, 2007, pp. 4637–4640 (cit. on pp. 68, 84, 120).

[66] S. Nikolaou and M. A. B. Abbasi, "Miniaturization of UWB antennas on organic material," *International Journal of Antennas and Propagation*, vol. 2016, 2016 (cit. on pp. 68, 84, 85, 120).

[67] ——, “Design and development of a compact UWB monopole antenna with easily-controllable return loss,” *IEEE Transactions on Antennas and Propagation*, vol. 65, no. 4, pp. 2063–2067, 2017 (cit. on p. 68).

[68] “IEEE standard definitions of terms for antennas,” *IEEE Std 145-1983*, pp. 1–31, Jun. 1983, ISSN: null. DOI: 10.1109/IEEESTD.1983.82386 (cit. on p. 70).

[69] “IEEE standard for definitions of terms for antennas,” *IEEE Std 145-2013 (Revision of IEEE Std 145-1993)*, pp. 1–50, Mar. 2014, ISSN: null. DOI: 10.1109/IEEESTD.2014.6758443 (cit. on pp. 70, 72, 74).

[70] C. A. Balanis, *Antenna Theory: Analysis and Design*, 3rd ed. 111 River Street, Hoboken, NJ 07030-5774: John Wiley & Sons, 2005 (cit. on pp. 70, 71, 72, 74, 75).

[71] D. M. Pozar, *Microwave Engineering*, 4th ed. 111 River Street, Hoboken, NJ 07030-5774: John Wiley & Sons, 2012 (cit. on pp. 73, 74).

[72] J.-F. Zürcher and F. E. Gardiol, *Broadband Patch Antennas*, 1st ed. 685 Canton Street Norwood, MA 02062: Artech House, 1995 (cit. on pp. 73, 74).

[73] D. Tran, V. Paraforou, and A. Yarovoy, “A novel 1-decade super wideband uhf antenna for gpr and impulse radio applications,” in *The 8th European Conference on Antennas and Propagation (EuCAP 2014)*, 2014, pp. 3073–3077 (cit. on pp. 84, 85, 120).

[74] *HFSS help, release 2019 r2*, ANSYS, Inc, Apr. 2019 (cit. on p. 86).

[75] *An introduction to multi-frequency adaptive meshing in hfss, release 2019 r2*, ANSYS, Inc, Apr. 2019 (cit. on p. 87).

Chapter 4

Conclusion

In this thesis, we have seen an account of the research efforts of the author. The research efforts were undertaken in the context of a research project into concealed weapons detection (CWD) radar. Prior to the thesis, prototype designs of a pulse generator and an antenna were developed by other project researchers, intended for use in the envisioned radar system. Considering the ultra-wideband (UWB) nature of the CWD project, the bandwidth and operating band specification of the devices has been of key concern. Neither the antenna nor the pulse generator met the bandwidth specifications at the research outset. For this reason, the author sought to improve the performance of the initial design prototypes.

To achieve this end, the author performed empirical investigations of the antenna and the pulse generator. In the investigations, incremental changes were applied to the designs of both devices. Some of the modified designs were fabricated and measured. As a result, revised final designs for both the antenna and the pulse generator were produced.

The final designs of both devices appear to manifest significantly improved bandwidth performance compared to the respective initial designs. For both designs, the desired operating band is from 0.5 GHz to 5 GHz. For the pulse generator, the −10 dB bandwidth of the output signal is increased about 31.7% from 3.31 GHz to 4.36 GHz based on the acquired data from a single prototype of both the initial and final designs. The measured −10 dB band of the final pulse generator output signal is from 0.385 GHz to 4.74 GHz. For the antenna, the maximum −10 dB reflection coefficient bandwidth is increased about 983% from 0.46 GHz to 4.98 GHz in the best performing prototypes. Additionally, the −10 dB reflection coefficient band coverage of the 0.5 GHz to 5 GHz band is nearly tripled from 32.5% to 97.3%. The largest measured −10 dB reflection coefficient operating band of the final antenna design is from 0.7 GHz to 5.68 GHz.

In conclusion, this thesis has demonstrated the possibility of improving the measured performance of a specific UWB pulse generator and antenna for a specific application. These improvements are the result of physical changes to the designs as implemented by the author. Despite the observed improvements in some areas, the new designs still fall somewhat short of the original design specifications.

Future research with the UWB pulse generator and antenna may need to be performed to identify additional performance enhancements. First, it would be desirable to measure the performance of the pulse generator and the antenna as a whole when connected as a system. Perhaps this could be done in such a way that the maximum detection range of the CWD system could be estimated for the initial designs versus the final designs. Also, the stability and repeatability of the measured device performance has not been rigorously established, especially in the pulse generator. We have seen as well the existence of performance variation between individual prototypes of the antenna, even within the same design, as a result of fabrication tolerance and human factors. Similar variation surely exists for the pulse generator design. Characterization of the extent of the device performance variation would be useful information for the project with regards to fabrication yield (i.e. what percentage of fabricated devices are expected to perform in an adequate fashion). It is the hope of the author that the contents of this thesis will serve as a useful reference of his work on the project which will aid in the continuing efforts of his colleagues.

Bibliography

[1] A. G. Yarovoy, L. P. Ligthart, J. Matuzas, and B. Levitas, "UWB radar for human being detection," *IEEE Aerospace and Electronic Systems Magazine*, vol. 21, no. 3, pp. 10–14, Mar. 2006, ISSN: 0885-8985. DOI: 10.1109/MAES.2006.1624185 (cit. on p. 1).

[2] S. Chang, N. Mitsumoto, and J. W. Burdick, "An algorithm for UWB radar-based human detection," in *2009 IEEE Radar Conference*, May 2009, pp. 1–6. DOI: 10.1109/RADAR.2009.4976999 (cit. on p. 1).

[3] D. J. Daniels, *EM Detection of Concealed Targets*, 1st ed., ser. Wiley Series in Microwave and Optical Engineering. 111 River Street, Hoboken, NJ 07030-5774: John Wiley & Sons, 2010 (cit. on p. 1).

[4] J. J. McCombe, "Noise reduction and clutter suppression in microwave imaging and detection," MASc Thesis, McMaster University, 2014. [Online]. Available: http://hdl.handle.net/11375/16345 (cit. on pp. 2, 4, 6, 9).

[5] G. R. Huguenin, "Millimeter-wave concealed weapons detection and through-the-wall imaging systems," in *Command, Control, Communications, and Intelligence Systems for Law Enforcement*, E. M. Carapezza and D. Spector, Eds., International Society for Optics and Photonics, vol. 2938, SPIE, 1997, pp. 152–

159. DOI: 10.1117/12.266735. [Online]. Available: https://doi.org/10.1117/12.266735 (cit. on pp. 2, 4, 5, 6, 8, 9).

[6] Y.-W. Chang, M. Juhola, W. Grainger, B. Wang, and B. Manahan, "Millimeter-wave concealed weapon detection," in *Command, Control, Communications, and Intelligence Systems for Law Enforcement*, E. M. Carapezza and D. Spector, Eds., International Society for Optics and Photonics, vol. 2938, SPIE, 1997, pp. 131–138. DOI: 10.1117/12.266731. [Online]. Available: https://doi.org/10.1117/12.266731 (cit. on pp. 2, 4).

[7] R. W. McMillan, O. Milton, M. C. Hetzler, R. S. Hyde, and W. R. Owerns, "Detection of concealed weapons using far-infrared bolometer arrays," in *25th International Conference on Infrared and Millimeter Waves (Cat. No.00EX442)*, 2000, pp. 259–260 (cit. on pp. 2, 4).

[8] N. C. Wild, F. Doft, D. Breuner, and F. S. Felber, "Handheld ultrasonic concealed weapon detector," in *Enabling Technologies for Law Enforcement and Security*, S. K. Bramble, E. M. Carapezza, L. I. Rudin, L. I. Rudin, and S. K. Bramble, Eds., International Society for Optics and Photonics, vol. 4232, SPIE, 2001, pp. 152–158. DOI: 10.1117/12.417527. [Online]. Available: https://doi.org/10.1117/12.417527 (cit. on p. 2).

[9] D. M. Sheen, D. L. McMakin, and T. E. Hall, "Three-dimensional millimeter-wave imaging for concealed weapon detection," *IEEE Transactions on Microwave Theory and Techniques*, vol. 49, no. 9, pp. 1581–1592, 2001 (cit. on pp. 2, 4).

[10] V. N. Radzikhovsky, V. P. Gorishniak, S. E. Kuzmin, and B. M. Shevchuk, "Radiometric imaging for concealed weapon detection," in *12th International*

Conference Microwave and Telecommunication Technology, 2002, pp. 596–597 (cit. on pp. 2, 4).

[11] D. Notel, J. Huck, S. Neubert, S. Wirtz, and A. Tessmann, “A compact mmw imaging radiometer for concealed weapon detection,” in *2007 Joint 32nd International Conference on Infrared and Millimeter Waves and the 15th International Conference on Terahertz Electronics*, 2007, pp. 269–270 (cit. on pp. 2, 4).

[12] S. Stanko, D. Notel, A. Wahlen, J. Huck, F. Kloppel, R. Sommer, M. Hagelen, and H. Essen, “Active and passive mm-wave imaging for concealed weapon detection and surveillance,” in *2008 33rd International Conference on Infrared, Millimeter and Terahertz Waves*, 2008, pp. 1–2 (cit. on pp. 2, 4).

[13] D. M. Sheen, T. E. Hall, R. H. Severtsen, D. L. McMakin, B. K. Hatchell, and P. L. J. Valdez, “Standoff concealed weapon detection using a 350-GHz radar imaging system,” in *Passive Millimeter-Wave Imaging Technology XIII*, D. A. Wikner and A. R. Luukanen, Eds., International Society for Optics and Photonics, vol. 7670, SPIE, 2010, pp. 57–68. DOI: 10.1117/12.852788. [Online]. Available: https://doi.org/10.1117/12.852788 (cit. on pp. 2, 4, 9).

[14] X. Zhuge and A. G. Yarovoy, “A sparse aperture mimo-sar-based uwb imaging system for concealed weapon detection,” *IEEE Transactions on Geoscience and Remote Sensing*, vol. 49, no. 1, pp. 509–518, 2011 (cit. on pp. 2, 4).

[15] A. Kumar and B. Jassal, “94 ghz radiometer for benchmarking its operational parameters for the remote detecton of concealed threat.,” *Defence Science Journal*, vol. 65, no. 5, 2015 (cit. on pp. 2, 4).

[16] W. F. Moulder, J. D. Krieger, J. J. Majewski, C. M. Coldwell, H. T. Nguyen, D. T. Maurais-Galejs, T. L. Anderson, P. Dufilie, and J. S. Herd, "Development of a high-throughput microwave imaging system for concealed weapons detection," in *2016 IEEE International Symposium on Phased Array Systems and Technology (PAST)*, 2016, pp. 1–6 (cit. on pp. 2, 4, 9).

[17] Y. Li, Z. Peng, and C. Li, "Potential active shooter detection using a portable radar sensor with micro-doppler and range-doppler analysis," in *2017 International Applied Computational Electromagnetics Society Symposium (ACES)*, 2017, pp. 1–2 (cit. on p. 2).

[18] Z. Sang and Y. Zhao, "Portable sub-terahertz radar for rapid long-range detecting concealed carried threat," in *2019 44th International Conference on Infrared, Millimeter, and Terahertz Waves (IRMMW-THz)*, 2019, pp. 1–2 (cit. on pp. 2, 4, 9).

[19] C. A. Martin and V. G. Kolinko, "Concealed weapons detection with an improved passive millimeter-wave imager," in *Radar Sensor Technology VIII and Passive Millimeter-Wave Imaging Technology VII*, R. Trebits, J. L. Kurtz, R. Appleby, D. A. Wikner, and N. N. Salmon, Eds., International Society for Optics and Photonics, vol. 5410, SPIE, 2004, pp. 252–259. DOI: 10.1117/12.543352. [Online]. Available: https://doi.org/10.1117/12.543352 (cit. on pp. 2, 4, 5, 8, 9).

[20] A. Achanta, M. McKenna, and J. Heyman, "Nonlinear acoustic concealed weapons detection," in *34th Applied Imagery and Pattern Recognition Workshop (AIPR'05)*, 2005, 7 pp.–27 (cit. on p. 2).

[21] J. Hausner, "Radar-based concealed threat detector," in *Radar Sensor Technology XIII*, K. I. Ranney and A. W. Doerry, Eds., International Society for Optics and Photonics, vol. 7308, SPIE, 2009, pp. 143–151. DOI: 10.1117/12.817478. [Online]. Available: https://doi.org/10.1117/12.817478 (cit. on pp. 2, 4, 5, 6, 8, 9).

[22] D. A. Andrews, S. W. Harmer, N. J. Bowring, N. D. Rezgui, and M. J. Southgate, "Active millimeter wave sensor for standoff concealed threat detection," *IEEE Sensors Journal*, vol. 13, no. 12, pp. 4948–4954, 2013 (cit. on pp. 2, 5).

[23] N. J. Bowring, M. J. Southgate, D. A. Andrews, N. D. Rezgui, S. W. Harmer, and D. O'Reilly, "Development of a longer range standoff millimetre wave radar concealed threat detector," in *Radar Sensor Technology XVII*, K. I. Ranney and A. Doerry, Eds., International Society for Optics and Photonics, vol. 8714, SPIE, 2013, pp. 96–106. DOI: 10.1117/12.2016554. [Online]. Available: https://doi.org/10.1117/12.2016554 (cit. on pp. 2, 4, 5, 6, 8, 9).

[24] B. Kapilevich, B. Litvak, A. Shulzinger, and M. Einat, "Portable passive millimeter-wave sensor for detecting concealed weapons and explosives hidden on a human body," *IEEE Sensors Journal*, vol. 13, no. 11, pp. 4224–4228, 2013 (cit. on pp. 2, 4, 5, 8, 9).

[25] Y. Li, Z. Peng, R. Pal, and C. Li, "Potential active shooter detection based on radar micro-doppler and range-doppler analysis using artificial neural network," *IEEE Sensors Journal*, vol. 19, no. 3, pp. 1052–1063, 2019 (cit. on pp. 2, 4, 5, 6, 8, 9).

[26] N. K. Nikolova and J. J. McCombe, *On-body concealed weapon detection system*, US Patent 10,229,328, Mar. 2019 (cit. on p. 2).

[27] L. Carrer and A. G. Yarovoy, “Concealed weapon detection using uwb 3-d radar imaging and automatic target recognition,” in *The 8th European Conference on Antennas and Propagation (EuCAP 2014)*, 2014, pp. 2786–2790 (cit. on pp. 4, 5).

[28] J. J. McCombe, “Cognitive microwave radar for the stand-off detection of on-body concealed weapons: Midterm report,” McMaster University, CEM-R- 70, Mar. 2015 (cit. on pp. 10, 11, 31, 38).

[29] J. J. McCombe and N. K. Nikolova, “Transmitter specifications for the stand-off detection of on-body concealed weapons: NATO SPS G4992,” McMaster University, CEM-R- 72, Jul. 2015 (cit. on pp. 10, 11, 31, 32, 34, 36).

[30] A. D. Pitcher, J. J. McCombe, E. A. Eveleigh, and N. K. Nikolova, “Compact transmitter for pulsed-radar detection of on-body concealed weapons,” in *2018 IEEE/MTT-S International Microwave Symposium-IMS*, IEEE, 2018, pp. 919–922 (cit. on pp. 13, 23, 35).

[31] E. A. Eveleigh, A. S. Beaverstone, and N. K. Nikolova, “Printed cactus monopole antenna with enhanced impedance bandwidth,” in *2019 IEEE International Symposium on Antennas and Propagation and USNC-URSI Radio Science Meeting*, IEEE, 2019, pp. 1085–1086 (cit. on pp. 13, 89).

[32] Industry Canada, “Radio standards specification RSS-220, issue 1, devices using ultra-wideband (UWB) technology,” Jul. 2018. [Online]. Available: https://www.ic.gc.ca/eic/site/smt-gst.nsf/eng/sf09347.html (cit. on pp. 21, 78).

[33] United States of America, “Title 47 CFR part 15, subpart F–ultra-wideband operation, §15.503,” May 2002. [Online]. Available: https://www.ecfr.gov/cgi-bin/text-idx?node=pt47.1.15#sp47.1.15.f (cit. on pp. 21, 78).

[34] “UWB regulations, A summary of worldwide telecommunications regulations governing the use of ultra-wideband radio,” Application Note: APR001, English, version 1.2, 2015. [Online]. Available: https://www.decawave.com/sites/default/files/apr001_uwb_worldwide_regulations_summaryrev1.2.pdf (cit. on pp. 21, 78).

[35] S. Haykin and B. Van Veen, *Signals and Systems*, 2nd ed., ser. Wiley Series in Microwave and Optical Engineering. 111 River Street, Hoboken, NJ 07030-5774: John Wiley & Sons, Feb. 2002, ISBN: 0-471-16474-7 (cit. on p. 21).

[36] H. Schantz, *The Art and Science of Ultrawideband Antennas*, 1st ed., ser. Artech House Antennas and Propagation Library. 685 Canton Street Norwood, MA 02062: Artech House, 2005 (cit. on pp. 21, 22, 23, 33, 70, 71, 72, 73, 74, 75, 76).

[37] F. Nekoogar, *Ultra-wideband Communications, Fundamentals and Applications*, 1st ed., ser. Prentice Hall Communications Engineering and Emerging Technologies Series. One Lake Street, Upper Saddle River, NJ 07458: Prentice Hall, Sep. 2005, ISBN: 0-13-146326-8 (cit. on pp. 21, 22, 23, 38, 60).

[38] J. Sachs, *Handbook of Ultra-Wideband Short-Range Sensing: Theory, Sensors, Applications*, 1st ed. Boschstr. 12, 69469 Weinheim, Germany: Wiley-VCH, 2012 (cit. on pp. 22, 28, 33, 75, 76, 79).

[39] T. Zwick, W. Wiesbeck, J. Timmermann, and G. Adamiuk, Eds., *Ultra-wideband RF System Engineering*, 1st ed., ser. EuMA High Frequency Technologies Series. Cambridge CB2 8BS, United Kingdom: Cambridge University Press, 2013 (cit. on pp. 22, 28, 29, 79).

[40] I. Oppermann, M. Hämäläinen, and J. Iinatti, Eds., *UWB Theory and Applications*, 1st ed. The Atrium, Southern Gate, Chichester, West Sussex PO19 8SQ, England: John Wiley & Sons, Oct. 2004, ISBN: 0-470-86917-8 (cit. on p. 22).

[41] E. W. Weisstein. (2020). "Gamma function." From MathWorld–A Wolfram Web Resource, Wolfram Mathworld, [Online]. Available: http://mathworld.wolfram.com/GammaFunction.html (cit. on p. 23).

[42] P. Protiva, J. Mrkvica, and J. Macháč, "Universal generator of ultra-wideband pulses," *Radioengineering*, vol. 17, no. 4, pp. 74–78, 2008 (cit. on pp. 23, 35, 36, 38).

[43] ——, "A compact step recovery diode subnanosecond pulse generator," *Microwave and optical technology letters*, vol. 52, no. 2, pp. 438–440, 2010 (cit. on pp. 23, 35).

[44] G. Avdeyenko, "Simulation and development of impulse ultrawideband signal generators for wireless communication systems," in *2018 International Scientific-Practical Conference Problems of Infocommunications. Science and Technology (PIC S T)*, Oct. 2018, pp. 349–353. DOI: 10.1109/INFOCOMMST.2018.8632056 (cit. on pp. 23, 35, 36).

[45] G. V. Fierro and G. E. Flores-Verdad, “A CMOS low complexity gaussian pulse generator for ultra wideband communications,” in *2009 52nd IEEE International Midwest Symposium on Circuits and Systems*, Aug. 2009, pp. 70–73. DOI: 10.1109/MWSCAS.2009.5236151 (cit. on pp. 23, 35).

[46] W. Feng, N. Li, and X. Li, “A 3–5 GHz UWB impulse generator in 0.13 µm CMOS,” *Microwave and Optical Technology Letters*, vol. 58, no. 9, pp. 2242–2245, 2016 (cit. on pp. 23, 35, 36).

[47] I. Mahbub, S. K. Islam, and A. Fathy, “Impulse radio ultra-wideband (IR-UWB) transmitter for low power low data rate biomedical sensor applications,” in *2016 IEEE Topical Conference on Biomedical Wireless Technologies, Networks, and Sensing Systems (BioWireleSS)*, Jan. 2016, pp. 88–90. DOI: 10.1109/BIOWIRELESS.2016.7445570 (cit. on pp. 23, 35).

[48] W. I. Jang, W. S. Choi, T. O. Kong, M. C. Park, and Y. S. Eo, “A power efficient impulse generator for 6-9 GHz UWB applications,” *Microwave and Optical Technology Letters*, vol. 61, no. 3, pp. 587–591, 2019 (cit. on pp. 23, 35, 36).

[49] C. Fang, C. L. Law, and J. Hwang, “High-voltage high-efficiency ultrawideband pulse synthesizer,” *IEEE Microwave and Wireless Components Letters*, vol. 20, no. 1, pp. 49–51, 2010 (cit. on pp. 25, 35, 36).

[50] C. Fang, C. L. Law, J. Hwang, and J. Xia, “Design and analysis of high-voltage high-efficiency ultra-wideband pulse synthesizer,” *Progress In Electromagnetics Research C*, vol. 20, pp. 187–201, 2011 (cit. on pp. 25, 35).

[51] K. Kim, S. Kim, M. Park, J. Choi, B. Koo, and P. Park, “A high voltage GaN impulse generator for human detection UWB radar sensor,” in *2017 14th International Conference on Ubiquitous Robots and Ambient Intelligence (URAI)*, Jun. 2017, pp. 527–528. DOI: 10.1109/URAI.2017.7992660 (cit. on pp. 25, 35).

[52] J. Xia, C. L. Law, Y. Zhou, and K. S. Koh, “3–5 GHz UWB impulse radio transmitter and receiver MMIC optimized for long range precision wireless sensor networks,” *IEEE Transactions on Microwave Theory and Techniques*, vol. 58, no. 12, pp. 4040–4051, 2010 (cit. on pp. 25, 35, 36).

[53] M. A. H. Ansari and C. L. Law, “High voltage high efficiency UWB pulse generator for precision localization wireless sensor network,” in *2016 International Symposium on Integrated Circuits (ISIC)*, Dec. 2016, pp. 1–4. DOI: 10.1109/ISICIR.2016.7829696 (cit. on pp. 25, 35).

[54] F. Zito, D. Zito, and D. Pepe, “Uwb 3.1-10.6 GHz CMOS transmitter for system-on-a-chip nano-power pulse radars,” in *2007 Ph.D Research in Microelectronics and Electronics Conference*, 2007, pp. 189–192 (cit. on p. 35).

[55] S. Bourdel, Y. Bachelet, J. Gaubert, R. Vauche, O. Fourquin, N. Dehaese, and H. Barthelemy, “A 9-pJ/pulse 1.42-Vpp OOK CMOS UWB pulse generator for the 3.1–10.6-GHz FCC band,” *IEEE Transactions on Microwave Theory and Techniques*, vol. 58, no. 1, pp. 65–73, 2010 (cit. on p. 35).

[56] J. B. Radic, A. M. Djugova, and M. S. Videnovic-Misic, “A 3.1–10.6 GHz impulse-radio UWB pulse generator in 0.18µm,” in *2011 IEEE 9th International Symposium on Intelligent Systems and Informatics*, 2011, pp. 335–338 (cit. on p. 35).

[57] M. J. Copps and K. J. Martin, “First report and order in the matter of revision of part 15 of the commission’s rules regarding ultra-wideband transmission systems,” United States Federal Communications Commission, FCC 02-48, Apr. 2002 (cit. on p. 35).

[58] D. Oloumi and E. Fear, “A picosecond pulse generator using srd diodes: Design, analysis, and measurements,” in *2018 USNC-URSI Radio Science Meeting (Joint with AP-S Symposium)*, 2018, pp. 159–160 (cit. on p. 35).

[59] M. Jafari and S. V. Mir-Moghtadaei, “A uwb pulse generator with step recovery diode (srd) for the characterizing and evaluation of materials using dielectric spectroscopy,” in *2019 27th Iranian Conference on Electrical Engineering (ICEE)*, 2019, pp. 427–430 (cit. on p. 35).

[60] (Oct. 29, 2019). “Coplanar waveguide with ground calculator.” English, Chemandy Electronics Ltd, [Online]. Available: https://chemandy.com/calculators/coplanar-waveguide-with-ground-calculator.htm (visited on 03/25/2020) (cit. on p. 40).

[61] B. Spokoinyi. (2020). “CPW (grounded) line calculator.” English, Spok Engineering Consulting, [Online]. Available: http://spok.ca/index.php/resources/tools/99-cpwcalc (visited on 03/25/2020) (cit. on p. 40).

[62] V. Zachou, C. G. Christodoulou, M. T. Chryssomallis, D. Anagnostou, and S. Barbin, “Planar monopole antenna with attached sleeves,” *IEEE Antennas and Wireless Propagation Letters*, vol. 5, pp. 286–289, 2006, ISSN: 1536-1225. DOI: 10.1109/LAWP.2006.876970 (cit. on p. 68).

[63] V. Zachou, C. G. Christodoulou, M. T. Chryssomallis, and D. Anagnostou, "Reconfigurable printed cactus antenna," in *2006 IEEE Antennas and Propagation Society International Symposium*, Jul. 2006, pp. 201–204. DOI: 10.1109/APS.2006.1710489 (cit. on p. 68).

[64] C. Saephan, H. Khaleel, B. Valdovinos, A. Isaac, and A. Bihnam, "Tri-band cactus shaped printed monopole," in *2014 IEEE Antennas and Propagation Society International Symposium (APSURSI)*, Jul. 2014, pp. 1704–1705. DOI: 10.1109/APS.2014.6905178 (cit. on p. 68).

[65] S. Nikolaou, G. E. Ponchak, M. M. Tentzeris, and J. Papapolymerou, "Compact cactus-shaped ultra wide-band (UWB) monopole on organic substrate," in *2007 IEEE Antennas and Propagation Society International Symposium*, IEEE, 2007, pp. 4637–4640 (cit. on pp. 68, 84, 120).

[66] S. Nikolaou and M. A. B. Abbasi, "Miniaturization of UWB antennas on organic material," *International Journal of Antennas and Propagation*, vol. 2016, 2016 (cit. on pp. 68, 84, 85, 120).

[67] ——, "Design and development of a compact UWB monopole antenna with easily-controllable return loss," *IEEE Transactions on Antennas and Propagation*, vol. 65, no. 4, pp. 2063–2067, 2017 (cit. on p. 68).

[68] "IEEE standard definitions of terms for antennas," *IEEE Std 145-1983*, pp. 1–31, Jun. 1983, ISSN: null. DOI: 10.1109/IEEESTD.1983.82386 (cit. on p. 70).

[69] "IEEE standard for definitions of terms for antennas," *IEEE Std 145-2013 (Revision of IEEE Std 145-1993)*, pp. 1–50, Mar. 2014, ISSN: null. DOI: 10.1109/IEEESTD.2014.6758443 (cit. on pp. 70, 72, 74).

[70] C. A. Balanis, *Antenna Theory: Analysis and Design*, 3rd ed. 111 River Street, Hoboken, NJ 07030-5774: John Wiley & Sons, 2005 (cit. on pp. 70, 71, 72, 74, 75).

[71] D. M. Pozar, *Microwave Engineering*, 4th ed. 111 River Street, Hoboken, NJ 07030-5774: John Wiley & Sons, 2012 (cit. on pp. 73, 74).

[72] J.-F. Zürcher and F. E. Gardiol, *Broadband Patch Antennas*, 1st ed. 685 Canton Street Norwood, MA 02062: Artech House, 1995 (cit. on pp. 73, 74).

[73] D. Tran, V. Paraforou, and A. Yarovoy, "A novel 1-decade super wideband uhf antenna for gpr and impulse radio applications," in *The 8th European Conference on Antennas and Propagation (EuCAP 2014)*, 2014, pp. 3073–3077 (cit. on pp. 84, 85, 120).

[74] *HFSS help, release 2019 r2*, ANSYS, Inc, Apr. 2019 (cit. on p. 86).

[75] *An introduction to multi-frequency adaptive meshing in hfss, release 2019 r2*, ANSYS, Inc, Apr. 2019 (cit. on p. 87).

Appendix A

Pulse Generator Fabrication Data

A.1 Circuit Schematics

The schematic pages for revision 3 and revision 4 of the pulse generator are shown below. Revision 3 and revision 4 share identical schematic diagrams. The revision 1 schematic has already been shown in Figure 2.3. Unlike with revision 1, the updated schematic has been split into distinct pages for the power supply (Figure A.1), the driver (Figure A.2), and the pulser and pulse forming stage combined (Figure A.3).

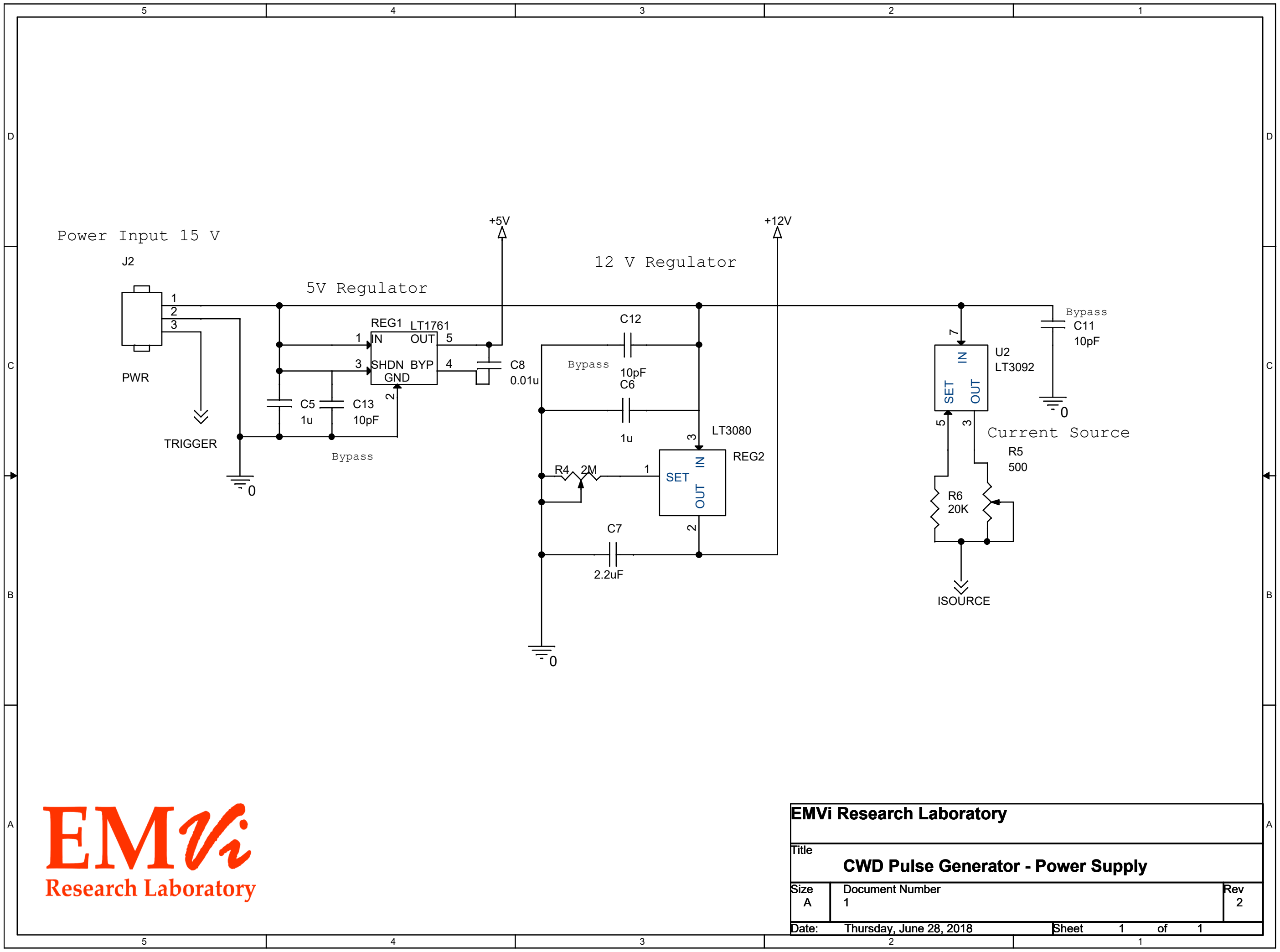

Figure A.1: Schematic of the power supply in pulse generator revision 3 and 4.

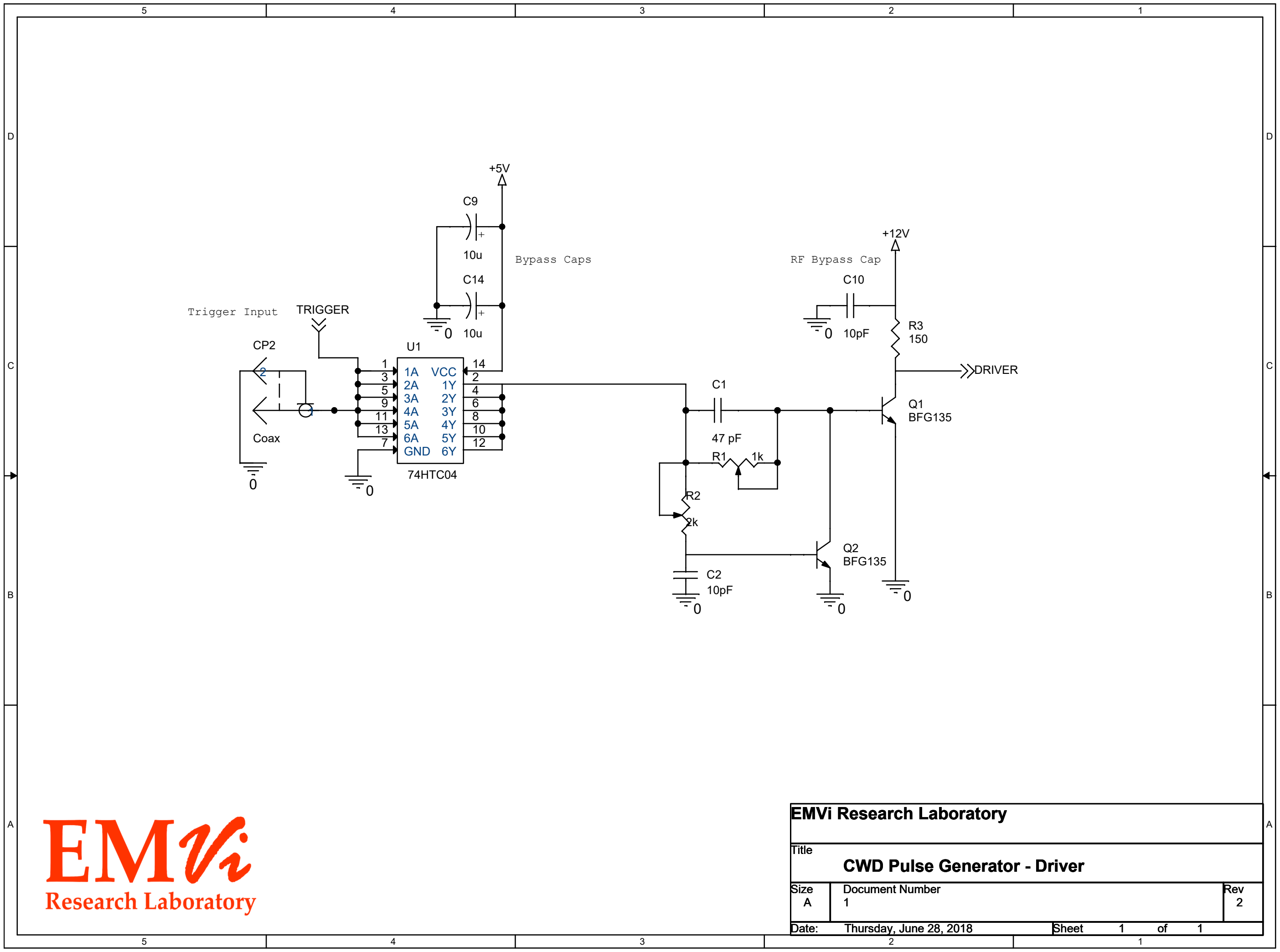

Figure A.2: Schematic of the Driver in pulse generator revision 3 and 4

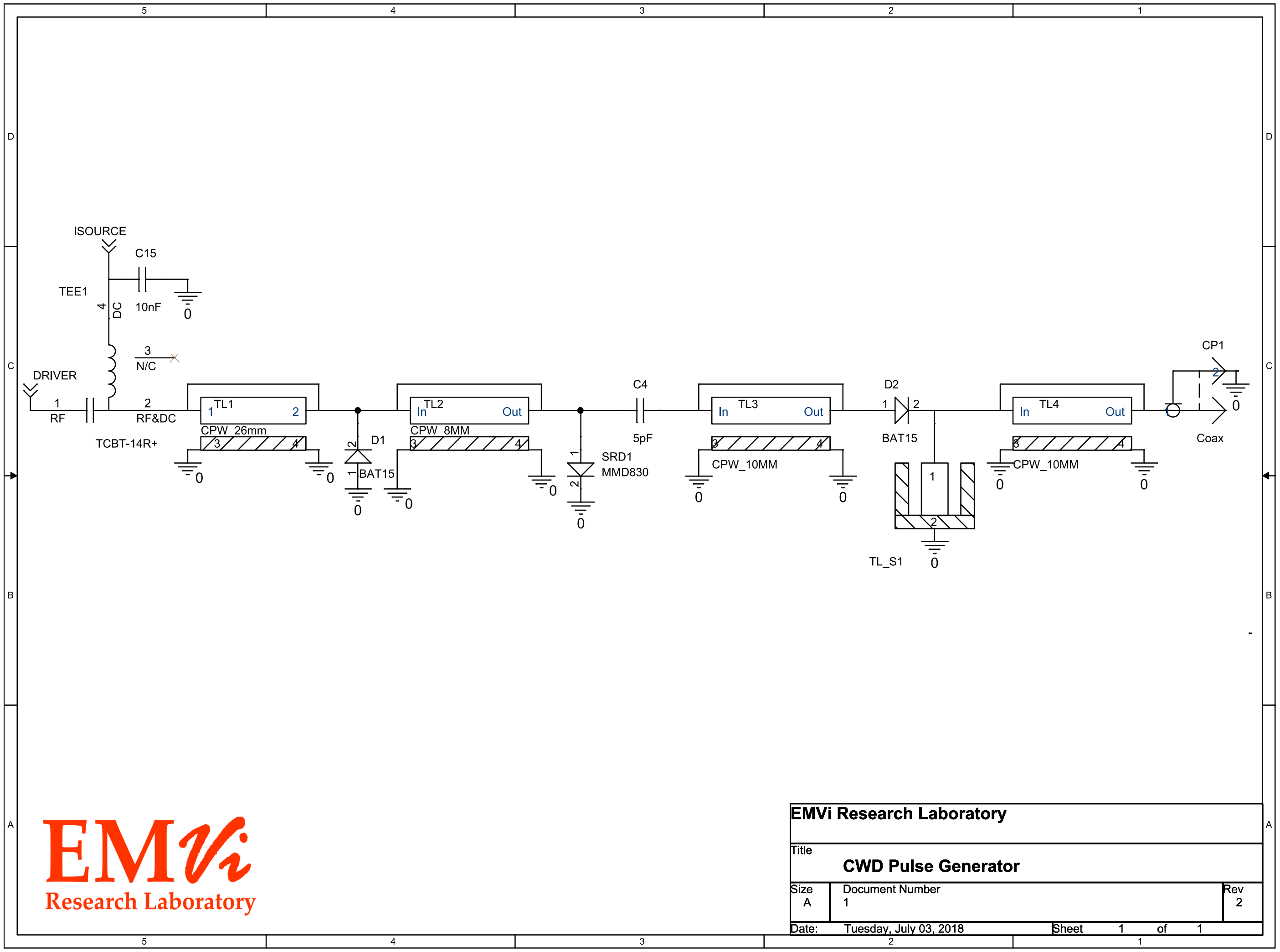

Figure A.3: Schematic of the pulser in pulse generator revision 3 and 4

A.2 PCB Fabrication Details

A.2.1 PCB Gerber Layers

The figures in this section give a complete set of printed circuit board (PCB) layers needed to fabricate Rev. 1 and Rev. 4 (4mm) boards. Each layer figure consists of the corresponding Gerber or drill file converted to PDF vector graphics at a 1:1 scale such that the exact geometry can be reproduced faithfully from the document. Shapes present in the Gerber files (and drilled holes) are rendered as black filled areas, while white areas are empty areas. As an alignment reference, the board edge layer is superimposed onto each layer figure as a faint gray rectangular outline.

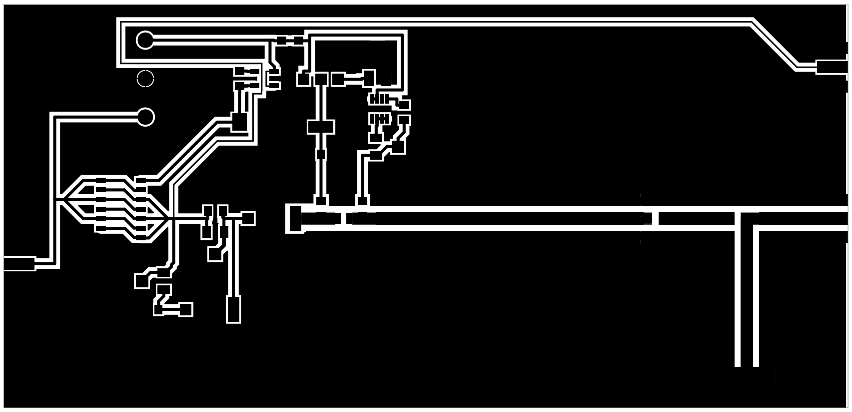

Figure A.4: Top copper layer for pulse generator revision 1.

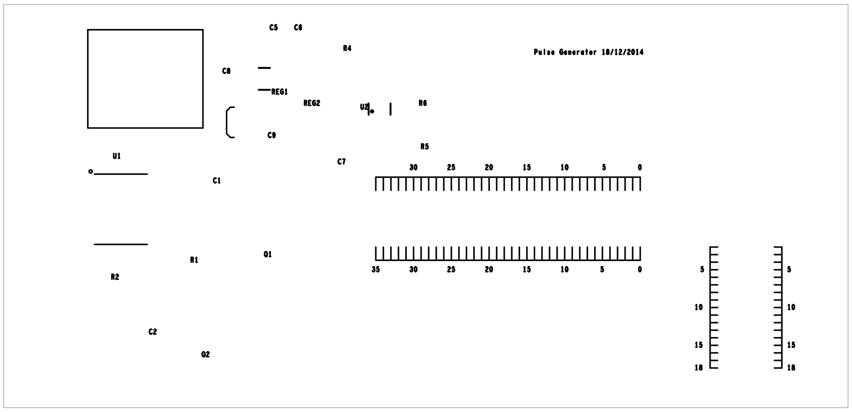

Figure A.5: Top silkscreen layer for pulse generator revision 1.

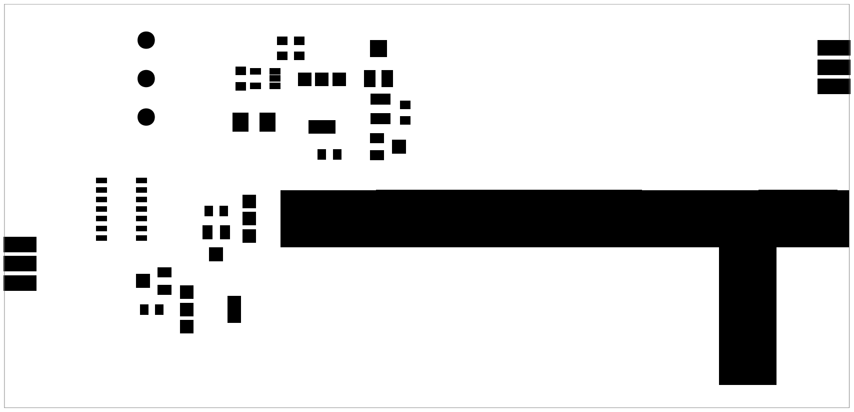

Figure A.6: Top solder mask layer for pulse generator revision 1.

Figure A.7: Bottom copper layer for pulse generator revision 1.

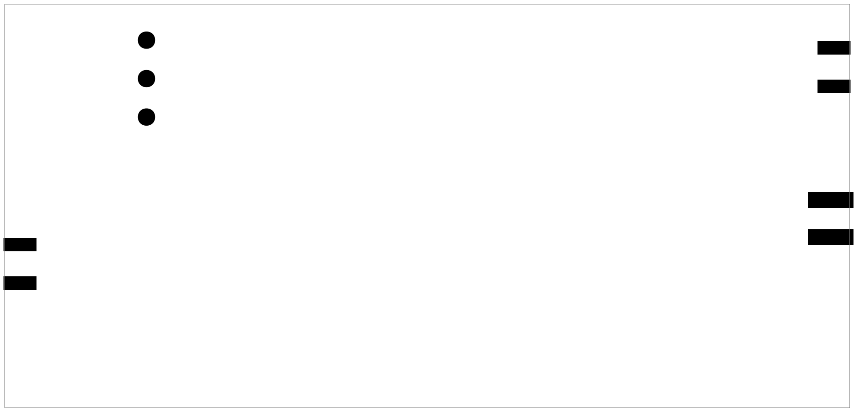

Figure A.8: Bottom solder mask layer for pulse generator revision 1.

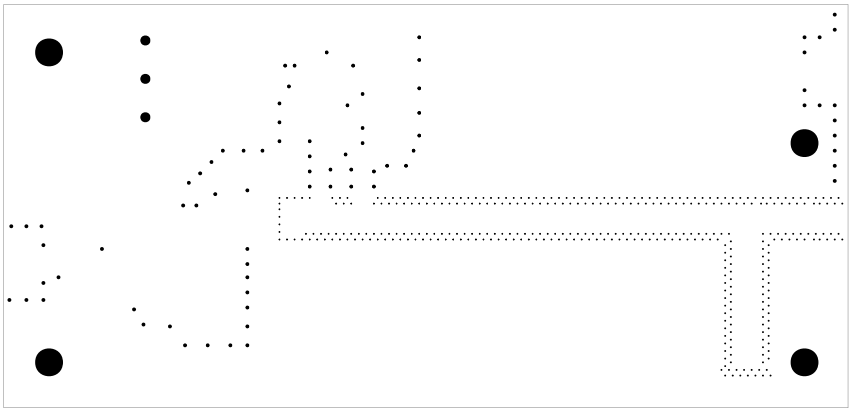

Figure A.9: Plated through holes for pulse generator revision 1.

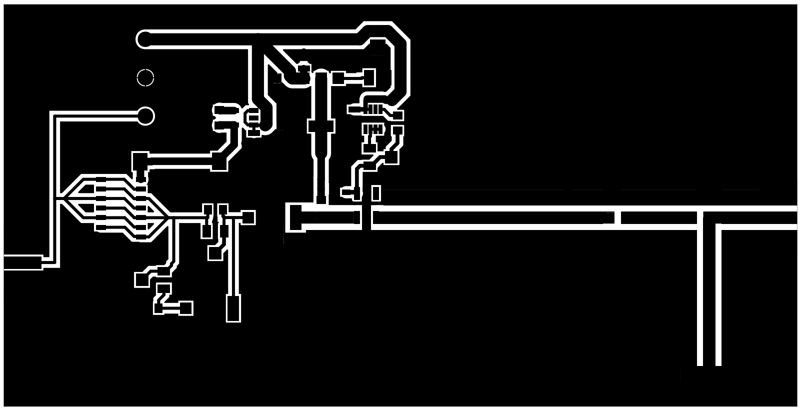

Figure A.10: Top copper layer for pulse generator revision 4 (4mm).

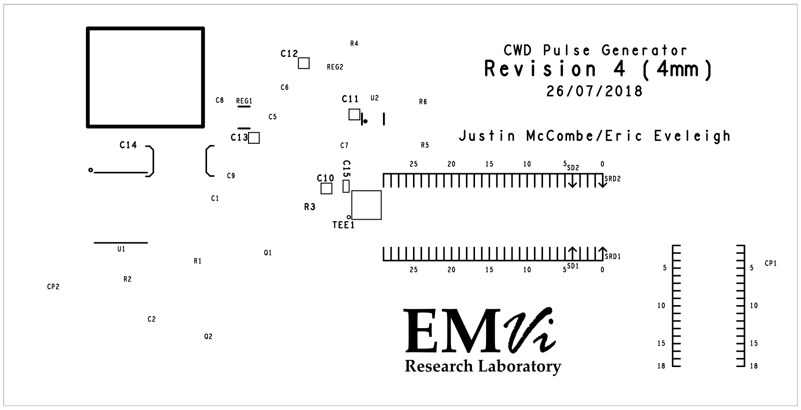

Figure A.11: Top silkscreen layer for pulse generator revision 4 (4mm).

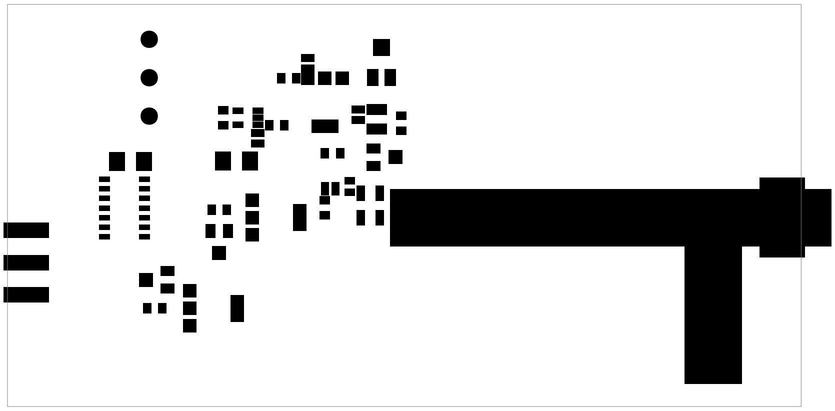

Figure A.12: Top solder mask layer for pulse generator revision 4 (4mm).

Figure A.13: Bottom copper layer for pulse generator revision 4 (4mm).

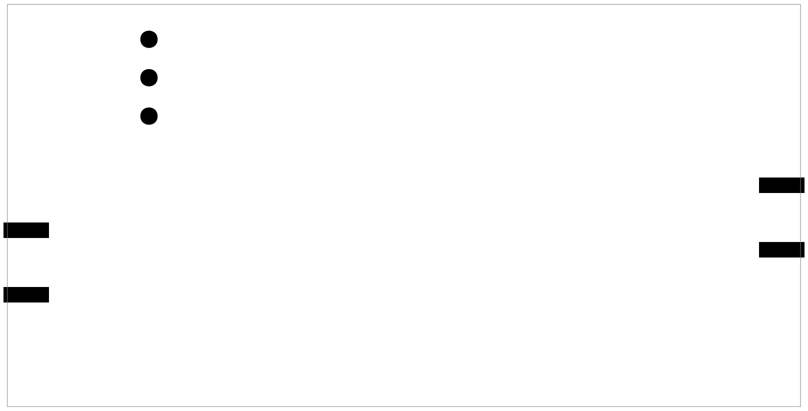

Figure A.14: Bottom solder mask layer for pulse generator revision 4 (4mm).

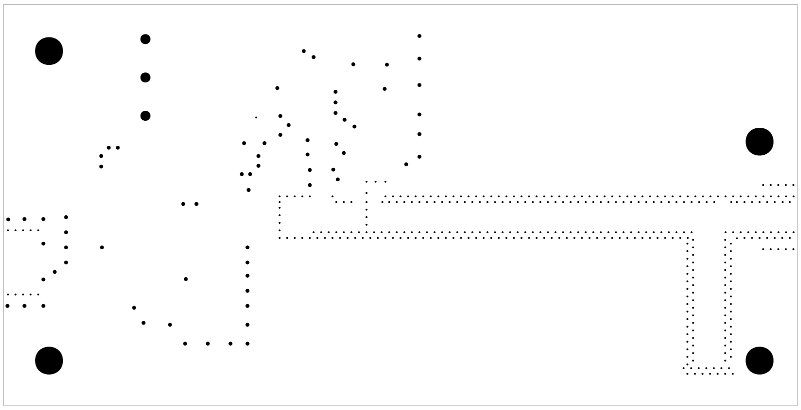

Figure A.15: Plated through holes for pulse generator revision 4 (4mm).

A.3 Bills of Materials

Table A.1: Bill of materials for pulse generator revision 1 at February 2020 prices in Canadian Dollar (1 CAD = 0.752457 USD). Total BOM Cost per Board: 278.38 CAD

Item	Quantity	Reference	Part	Supplier	Price	Notes
1	1	CP1	PE44213	Pasternack	32.08	24.17 USD
2	2	CP2, CP3	CONSMA003.031-L	Mouser	8.85	
3	1	C1	08052U470FAT2A	Digi-Key	0.84	
4	1	C2	600F100GT250XT	Digi-Key	1.86	
5	1	C3	AQ125A102KAJME	Digi-Key	3.80	
6	1	C4	600F5R1BT250XT	Digi-Key	1.94	
7	2	C5, C6	CL21B105KAFNNNE	Digi-Key	0.16	
8	1	C7	TMK212B7225KG-TR	Digi-Key	0.40	
9	1	C8	08055C103KAT2A	Digi-Key	0.19	
10	1	C9	F931E106KBA	Digi-Key	1.17	
11	2	D1, D2	BAT1503WE6327HTSA1	Digi-Key	0.60	
12	1	J2	OSTTG035100B	Digi-Key	1.62	
13	1	L1	805CS-060XJEB	Coilcraft	1.05	0.79 USD
14	2	Q1, Q2	BFG135	eBay	2.02	1.52 USD (lot of 25, NOS)
15	1	REG1	LT1761IS5-5#TRMPBF	Mouser	3.91	
16	1	REG2	LT3080EST#PBF	Mouser	5.28	
17	1	R1	3313J-1-102E	Mouser	2.47	
18	1	R2	3313J-1-202E	Mouser	2.47	
19	1	R3	4-2176091-1	Digi-Key	1.01	
20	1	R4	3314J-1-205E	Mouser	2.95	
21	1	R5	3313J-1-501E	Mouser	2.47	
22	1	R6	ERJ-6ENF2002V	Digi-Key	0.15	
23	1	SRD1	MMD830-0805-2	RFMW	24.08	18.12 USD (Feb. 2018)
24	1	U1	74HCT04D,653	Digi-Key	0.56	
25	1	U2	LT3092ETS8#TRPBF	Mouser	5.85	
26	1		108-0902-001	Digi-Key	1.33	Power connector
27	1		108-0903-001	Digi-Key	1.33	Power connector
28	1		B1-120BL	Newark	25.06	Aluminum enclosure
29	1		Rev. 1 PCB	CCI, Inc	131.25	Immersion silver finish

Table A.2: Bill of materials for pulse generator revision 3 and 4 at February 2020 prices in Canadian Dollar (1 CAD = 0.752457 USD). Total BOM Cost per Board: 249.84 CAD

Item	Quantity	Reference	Part	Supplier	Price	Notes
1	2	CP1, CP2	CONSMA003.031-L	Mouser	8.85	
2	1	C1	08052U470FAT2A	Digi-Key	0.84	
3	1	C2	600F100GT250XT	Digi-Key	1.86	
4	1	C4	600F5R1BT250XT	Digi-Key	1.94	
5	2	C5, C6	CL21B105KAFNNNE	Digi-Key	0.16	
6	1	C7	TMK212B7225KG-TR	Digi-Key	0.40	
7	1	C8	885012207092	Digi-Key	0.14	
8	2	C9, C14	F931E106KBA	Digi-Key	1.17	
9	4	C10–C13	100A100JT150XT	Digi-Key	3.32	Optional (bypass caps)
10	1	C15	EMK107SD103KA-T	Digi-Key	0.46	
11	2	D1, D2	BAT1503WE6327HTSA1	Digi-Key	0.60	
12	1	J2	OSTTG035100B	Digi-Key	1.62	
13	2	Q1, Q2	BFG135	eBay	2.02	1.52 USD (lot of 25, NOS)
14	1	REG1	LT1761IS5-5#TRMPBF	Mouser	3.91	
15	1	REG2	LT3080EST#PBF	Mouser	5.28	
16	1	R1	3313J-1-102E	Mouser	2.47	
17	1	R2	3313J-1-202E	Mouser	2.47	
18	1	R3	4-2176091-1	Digi-Key	1.01	
19	1	R4	3314J-1-205E	Mouser	2.95	
20	1	R5	3313J-1-501E	Mouser	2.47	
21	1	R6	ERJ-6ENF2002V	Digi-Key	0.15	
22	1	SRD1	MMD830-0805-2	RFMW	24.08	18.12 USD (Feb. 2018)
23	1	TEE1	TCBT-14R+	Mini-Circuits	11.23	8.45 USD @ 10 quantity
24	1	U1	74HCT04D,653	Digi-Key	0.56	
25	1	U2	LT3092ETS8#TRPBF	Mouser	5.85	
26	1		108-0902-001	Digi-Key	1.33	Power connector
27	1		108-0903-001	Digi-Key	1.33	Power connector
28	1		B1-120BL	Newark	25.06	Aluminum enclosure
29	1		Rev. 4 PCB	CCI, Inc	131.25	Immersion silver finish

Appendix B

Antenna Replication Instructions

This appendix contains detailed instructions for precise reproduction of both the initial (design04sma) and final (APS2019) antenna designs. The instructions are useful for the purposes of replicating the antennas in an electromagnetic (EM) simulator or in printed circuit board (PCB) computer-aided design (CAD) software for fabrication. Any desired parametrization of either model is left to the reader to implement.

B.1 Modelling the Initial (design04sma) Design

This section describes, in detail, the steps required to model the design04sma antenna. It consists of instructions and data tables which, when combined, allow faithful reconstruction of the original model. An outline of the modelling steps is as follows.

1. Model the substrate
    (a) Create a rectangular prism of appropriate dimensions in an appropriately

    defined global coordinate system

  (b) Assign material properties (if applicable)

2. Model the metallization
   - (a) Create the feed geometry
     - i. Ground planes
     - ii. Co-planar waveguide (CPW) structure
   - (b) Create the radiator
     - i. Create three rectangular strips
     - ii. Create two annular sectors
   - (c) Create the triangular hedge
     - i. Draw the first triangle
     - ii. Duplicate N times
   - (d) Combine metallization objects
   - (e) Assign material properties (if applicable)
3. Model the cavity
   - (a) Create the side walls
   - (b) Create the bottom
   - (c) Create the shorting post
   - (d) Combine objects
   - (e) Assign material properties (if applicable)

TABLE B.1: SUBSTRATE OUTLINE VERTICES IN THE INITIAL ANTENNA DESIGN ($z = 0$). UNITS IN MILLIMETRES.

Index	Coordinates (x, y)
1	(0, 60.4)
2	(0, -90.6)
3	(150, -90.6)
4	(150, 60.4)

B.1.1 Modelling the Substrate

Choose a 3D cartesian coordinate system that allows negative coordinates *with units in millimetres.* Draw a rectangle of width 151 mm and 150 mm length. See Table B.1 for the exact coordinates of the corners. Convert this rectangle into a rectangular prism of height 1.57 mm. The top of the prism should remain at $z = 0$, so the height should be expanded downward. The bottom of the prism finally lies in the $z = -1.57$ plane.

Assigning Material Properties to the Substrate

If the antenna is being modelled in an EM simulator, assign the prism with the material properties of Flame Retardant 4 (FR-4). Set the ϵ_r value to 4.4 and the $\tan\delta$ value to 0.018, or use the simulator's built in FR-4 material. Keep in mind that modelling FR-4 as a homogeneous, isotropic dielectric material is an approximation.

B.1.2 Modelling the Metallization

The metallization consists of the ground planes, the feed structure, the radiator, and the triangular hedge. Each of these is detailed next.

Table B.2: Ground plane vertices in the initial antenna design ($z = 0$). Units in millimetres.

(a) First ground plane polygon

Index	Coordinates (x, y)
1	(0, 60.4)
2	(0, 2.125)
3	(3.3, 1.5)
4	(12.4139, 1.5)
5	(12.4139, 60.4)

(b) Second ground plane polygon

Index	Coordinates (x, y)
1	(0, -2.125)
2	(0, -90.6)
3	(12.4139, -90.6)
4	(12.4139, -1.5)
5	(3.3, -1.5)

Ground Planes

Create the ground planes of the feed structure by drawing two filled polygons in the $z = 0$ plane. See Table B.2a and Table B.2b.

Feed Structure

The feed structure interacts with the split ground plane to form modified CPW line. The shape of the center conductor is also exactly representable as a filled polygon, with vertices shown in Table B.3.

Radiator

The radiator consists of five patches: three rectangles and two annular sectors. The rectangles are again exactly representable as polygons (See Table B.4a, Table B.4b, and Table B.4c). On the other hand, the annular sectors cannot be exactly represented as polygons since two of their edges are circular arcs. These shapes may be approximated as polygons (faceted), as is typical in finite element modelling or when plotting a PCB for fabrication. Luckily, an annular sector is the shape which

TABLE B.3: THE CENTER CONDUCTOR VERTICES IN THE INITIAL ANTENNA DESIGN ($z = 0$). UNITS IN MILLIMETRES.

Index	Coordinates (x, y)
1	(0, 1.25)
2	(0, -1.25)
3	(6.4, -1.25)
4	(12.8639, -0.22)
5	(13.3039, -0.22)
6	(13.3039, 0.22)
7	(12.8639, 0.22)
8	(6.4, 1.25)

TABLE B.4: THE RECTANGULAR PATCHES IN THE INITIAL ANTENNA DESIGN ($z = 0$). UNITS IN MILLIMETRES.

(a) Vertices of patch A

Index	Coordinates (x, y)
1	(35.1247, 0.17)
2	(35.1247, -21.799)
3	(90.2447, -21.799)
4	(90.2447, 0.17)

(b) Vertices of patch B

Index	Coordinates (x, y)
1	(30.2739, 33.915)
2	(30.2739, 0.684)
3	(117.0439, 0.684)
4	(117.0439, 33.915)

(c) Vertices of patch C

Index	Coordinates (x, y)
1	(76.61918, -40.0899)
2	(76.61918, -63.3507)
3	(120.38918, -63.3507)
4	(120.38918, -40.0899)

TABLE B.5: PARAMETERS OF THE LONG ANNULAR BEND IN THE INITIAL ANTENNA DESIGN.

(a) Line Segment

Index	Coordinates (x, y)
1	(12.8639, 0)
2	(31.2739, 0)

(b) Sweep Parameters

Type	Value
Origin (x, y, z)	(68.4839, 0, 0)
Sweep Axis (x, y, z)	(0, 0, 1)
Sweep Angle	-30 deg

TABLE B.6: PARAMETERS OF THE SHORT ANNULAR BEND IN THE INITIAL ANTENNA DESIGN.

(a) Line Segment

Index	Coordinates (x, y)
1	(36.1247, 0)
2	(12.8639, 0)

(b) Sweep Parameters

Type	Value
Origin (x, y, z)	(76.2146, 0, 0)
Sweep Axis (x, y, z)	(0, 0, 1)
Sweep Angle	90 deg

results from sweeping a line segment around a specified axis through a specified sweep angle. These features, therefore, are exactly specified as the endpoints of the line segment, the origin and direction of the sweep axis, and the sweep angle (Table B.5 and Table B.6). In case such an operation cannot be performed in the specific CAD software, the given descriptions can be used to mathematically generate faceted polygonal approximations of the annular sectors with an arbitrary level of detail.

Triangular Hedge

The triangular hedge consists of 20 identical metallic triangles spaced evenly apart. The vertices of the first triangle are given in Table B.7. Each triangle in the sequence is a copy of the previous triangle, where the vertices have been translated using the

Table B.7: The first triangle in the triangular hedge of the initial antenna design ($z = 0$). Units in millimetres.

Index	Coordinates (x, y)
1	(137.3, -87.1)
2	(150, -90.6)
3	(150, -83.6)

vector $< 0, 7.5, 0 >$.

Assigning Material Properties of the Metallization

If the metallization is left as a 2D polygon, it must be assigned as a perfect electric conductor () boundary in the simulation. This is because an infinitesimally thin conductor of finite conductivity is impossible to model in some simulators. If the metallization has been thickened, it can be assigned the material properties of Copper to match standard FR-4 laminate, or simply left as a PEC volume.

For the EM simulation, finite thickness of the metallization may be desired. The nominal metallization thickness of 1-Oz Copper FR-4 laminate is 1.4 mil, which equals 0.035 56 mm. The combined metallization shape in the $z = 0$ plane should be swept along the $< x, y, z > = < 0, 0, 1 >$ direction such that the top of the resulting solid is at $z = 0.03556$.

B.1.3 Modelling the Cavity

The cavity is composed of four metallic side walls, a bottom cover, and a shorting post. The total cavity height is 43.89 mm. First, the side walls are drawn at the top of the antenna substrate ($z = 0$) and extend down towards the bottom ($z = -43.89$). Then, bottom cover is placed to close the rectangular hole. Finally, the shorting post is attached between the cavity bottom and the antenna metallization to finish the model.

Side Walls

The side walls are constructed from the vertices in Table B.1. These vertices are first used to form a sequence of connected line segments (a Polyline in ANSYS High Frequency Structure Simulator (HFSS)) following the vertex order. Then, this polyline is swept through the vector $< -43.89, 0, 0 >$. This forms a 3D surface with four rectangular faces and 12 edges. The final step is to create an opening in one wall for the sub-miniature A (SMA) connector (to prevent the feed from being shorted out). This is achieved by subtracting a circle from the wall in the $x = 0$ plane. The circle center point is located at $(0, 0, 0.635)$ and the radius is 2.125 mm.

Bottom

The cavity bottom is constructed also from the vertices in Table B.1. Instead of setting $z = 0$, however, the plane is located at $z = -43.89$. Then the vertices are used to draw a rectangle, similar to how the substrate was constructed. Once this is finished, the cavity bottom should be united with the side walls into one 3D surface. The resulting surface can then be assigned the appropriate material properties.

Shorting Post

Before placing the shorting post, a hole must be "drilled" in the antenna substrate. To create the hole, a cylinder is subtracted from the substrate object. The hole cylinder is placed at the point (117.38918, -51.7203, 0). It has a radius of 2.5 mm and a height of 1.57 mm extending in the $< 0, 0, -1 >$ direction.

The shorting post is modelled as a metallic cylinder. This cylinder is placed at the same point as the hole cylinder. It has a height of 43.89 mm, extending downwards, and a radius of 2.25 mm. When constructed in this way the shorting post should only touch the antenna metallization and the cavity back cover, and it should not protrude through either of these surfaces.

Assigning Material Properties

The cavity metallization and the shorting post must be assigned material properties for simulation purposes. The metallization consists of the combined surface of the cavity side walls and bottom. This surface should be assigned the material properties of PEC by assigning a PEC boundary to the surface. The shorting post consists only of a cylinder. This cylinder is assigned as either a PEC solid or as copper.

B.2 Modelling the Final (APS2019) Design

This section tabulates the information required to model the APS2019 antenna. The steps are much the same as for the initial antenna design, so much of the detailed instruction of each step is omitted for conciseness. The reader should refer to the previous section should such level of detail be required. The outline of steps is as follows.

1. Model the substrate
    (a) Create a rectangular prism of appropriate dimensions in an appropriately defined global coordinate system

Table B.8: Substrate outline vertices in the final antenna design ($z = 0$). Units in millimetres.

Index	Coordinates (x, y)
1	(0, 72.245)
2	(0, -108.3675)
3	(150, -108.3675)
4	(150, 72.245)

   (b) Assign material properties (if applicable)

2. Model the metallization
   (a) Create the feed geometry
      i. Ground planes
      ii. CPW structure
   (b) Create the radiator
      i. Create three rectangular strips
      ii. Create two annular sectors
   (c) Combine metallization objects
   (d) Assign material properties (if applicable)

B.2.1 Modelling the Substrate

The substrate is modelled according to the vertices in Table B.8. Refer to the instructions under subsection B.1.1.

Table B.9: Ground plane vertices of the final antenna design ($z = 0$). Units in millimetres.

(a) First ground plane polygon

Index	Vertex (x, y)
1	(0, 72.245, 0)
2	(0, 2.125)
3	(3.3, 1.65)
4	(33, 1.65)
5	(39.0139, 0.65)
6	(39.0139, 72.245)

(b) Second ground plane polygon

Index	Vertex (x, y)
1	(0, -2.125)
2	(0, -108.3675)
3	(39.0139, -108.3675)
4	(39.0139, -0.65)
5	(33, -1.65)
6	(3.3, -1.65)

Assigning Material Properties of the Substrate

The substrate should be assigned the material properties of FR-4 if needed.

B.2.2 Modelling the Metallization

The metallization consists of the ground planes, the feed structure and the radiator. For full details refer to explanations under subsection B.1.2.

Ground Planes

Create the ground planes of the feed structure according to Table B.9a and Table B.9b.

Feed Structure

Create the feed structure using the vertices shown in Table B.10.

Table B.10: The center conductor vertices of the final antenna design ($z = 0$). Units in millimetres.

Index	Coordinates (x, y)
1	(0, 1.25)
2	(0, -1.25)
3	(33, -1.25)
4	(39.4639, -0.22)
5	(39.9039, -0.22)
6	(39.9039, 0.22)
7	(39.4639, 0.22)
8	(33, 1.25)

Radiator

Create three rectangular patches as in Table B.11a, Table B.11b, and Table B.11c. Then, create the two annular sectors from the information in Table B.12 and Table B.13.

Assigning Material Properties of the Metallization

The metallization should be either assigned as a PEC boundary, or thickened and assigned as copper metal. See section B.1.2 for full details.

TABLE B.11: THE RECTANGULAR PATCHES IN THE RADIATOR OF THE FINAL ANTENNA DESIGN EXPRESSED AS POLYGONS ($z = 0$). UNITS IN MILLIMETRES

(a) Vertices of patch A

Index	Coordinates (x, y)
1	(61.7247, 0.17)
2	(61.7247, -21.799)
3	(116.8447, -21.799)
4	(116.8447, 0.17)

(b) Vertices of patch B

Index	Coordinates (x, y)
1	(56.8739, 33.915)
2	(56.8739, 0.684)
3	(143.6439, 0.684)
4	(143.6439, 33.915)

(c) Vertices of the patch C

Index	Coordinates (x, y)
1	(102.8146, -40.0899)
2	(102.8146, -63.3507)
3	(146.5846, -63.3507)
4	(146.5846, -40.0899)

TABLE B.12: PARAMETERS OF THE SHORT ANNULAR BEND IN THE FINAL ANTENNA DESIGN.

(a) Line Segment ($z = 0$)

Index	Coordinates (x, y)
1	(39.4639, 0)
2	(57.8739, 0)

(b) Sweep Parameters

Type	Value
Origin (x, y, z)	(95.0839, 0, 0)
Sweep Axis (x, y, z)	(0, 0, 1)
Sweep Angle	-30 deg

TABLE B.13: PARAMETERS OF THE LONG ANNULAR BEND IN THE FINAL ANTENNA DESIGN.

(a) Line Segment

Index	Coordinates (x, y)
1	(62.7247, 0)
2	(39.4639, 0)

(b) Sweep Parameters

Type	Value
Origin (x, y, z)	(102.8146, 0, 0)
Sweep Axis (x, y, z)	(0, 0, 1)
Sweep Angle	90 deg